MODELING AND SYNTHESIS OF A PIEZOELECTRIC CERAMIC-REINFORCED METAL MATRIX COMPOSITE

by

Adam Goff

Thesis submitted to the Faculty of the
Virginia Polytechnic Institute and State University
in partial fulfillment of the requirements for the degree of

MASTER OF SCIENCE

in

Materials Science and Engineering

APPROVED:

Professor Stephen L. Kampe, Chairman

Professor Alex O. Aning

Professor Sean G. Corcoran

May 15, 2003
Blacksburg, Virginia

Keywords: Mechanical Damping, Piezoelectricity, Metal Matrix Composites, Eshelby Method

MODELING AND SYNTHESIS OF A PIEZOELECTRIC CERAMIC-REINFORCED METAL MATRIX COMPOSITE

by

Adam Goff

(ABSTRACT)

A mathematical model has been created based on J.D. Eshelby's equivalent inclusion method that can predict the elastic modulus and damping capability in the form of Joule heat for any piezoelectric ceramic-reinforced metal matrix composite system. Specifically, barium titanate ($BaTiO_3$), lead titanate ($PbTiO_3$), and zinc oxide (ZnO) piezoelectric ceramics have been modeled as dispersed particles shaped as spheres, prolate spheroids, and discs within a host of common structural metallic matrices including 304 stainless steel, mild steel, aluminum, brass, copper, lead, magnesium, nickel, Ni-20wt%Cr, tin, titanium, Ti-6Al-4V(at%), and tungsten. Composite systems that were predicted to exhibit the greatest level of damping capacity include copper, aluminum, and magnesium matrices reinforced with $PbTiO_3$, $BaTiO_3$, and ZnO, in descending order of damping magnitude. In general, higher-conducting, lower-stiffness metallic matrices coupled with more-piezoelectric, higher-stiffness ceramic reinforcement resulted in the greatest level of predicted damping capability and enhanced composite elastic modulus. Additionally, a Ni-20wt%Cr-30v%$BaTiO_3$ composite has been created using mechanical alloying processing. Specifically, pure constituent powders were combined stoichiometrically in a SPEX milling vial utilizing a charge ratio of 4:1 and subsequently milled for 24 hours. Separate composite powder samples were then annealed in a hydrogen tube furnace at 400°C, 500°C, and 600°C for one and five hours at each temperature. X-ray diffraction was performed on the as-milled and the annealed powders revealing that each was composed of the starting constituents in the appropriate proportions. Representative powders were mounted and polished using common metallographic procedures and microstructures were examined by optical microscopy, scanning electron microscopy, and transmission electron microscopy. All of the powders exhibited a good dispersion of $BaTiO_3$ particles ranging in diameter from 1μm to about 25nm with no noticeable difference between the as-milled and the annealed powders.

ACKNOWLEDGEMENTS

I would like to thank my graduate advisor, Dr. Stephen L. Kampe, for his directional guidance, advice, and mentoring throughout the course of this thesis work. I would also like to thank Dr. Alex Aning, Dr. Sean Corcoran, and Dr. William Reynolds for all of their guidance and for the valuable discussions we had on powder processing and modeling issues. I must also express gratitude to the sponsors of this research work, Dr. William Mullins from ARO and Dr. Leo Christodoulou from DARPA. Project funding was provided under ARO contract # DAAD19-01-1-0714.

Special thanks go to my graduate student colleagues, Shawn Kelly, Jennifer Franklin, and Ben Poquette for assisting in research-related issues and providing comic relief in the office. Thanks also go to the entire office faculty in the Materials Science and Engineering Department for assisting with product ordering problems and procedural issues. Particular appreciation goes to David Berry for his mechanical help with any and all lab equipment and to Steve McCartney for his assistance in using the SEM and TEM.

I would also like to express great gratitude to my parents, Vernon and Anne, my brothers, Matt and Nathan, my Grandparents, and the rest of mine and my fiancé's family for love, financial and emotional support, and encouragement to pursue my graduate education.

Finally, I would like to deeply thank my fiancé, Caren, for all of her love, support, understanding, and patience all throughout my undergraduate and graduate studies. For without her support, none of this work would be possible.

LIST OF FIGURES

LIST OF TABLES

TABLE OF CONTENTS

1. BACKGROUND

1.1 Project Introduction

There exists a need to provide vibration damping capabilities to many different structural engineering applications throughout our world. Whether that need is for acoustic noise reduction for a clandestine military operation, or mechanical vibration suppression for fatigue prevention on an aircraft, the goal is the same: To reduce unwanted vibration perturbations within that environment. At present, materials that exhibit poor self-damping capabilities tend to dominate the bulk of structural applications. Vibration reduction is thus achieved through the use of active or passive damping materials that are often-times added on top of the existing structure. Therefore, mass and cost is supplementary to the already-bulky and sometimes expensive structural component.

In any engineering design and construction problem it is essential to consider the variational parameters that most-greatly affect the behavior and life of the given structure. Therefore, choices must be made as to which properties are most crucial for a given design decision. An example of this can be found in the materials selection plot of Figure 1 showing Young's modulus versus damping loss coefficient for many typical aerospace structural materials. It can be seen that while magnesium, aluminum, titanium and their alloys offer some significant damping capability (expressed by a higher damping coefficient), they do not offer the higher stiffness and corrosion resistance benefit of some of the superalloys. On the other hand, the superalloys don't always offer the level of inherent damping capability that the previously said alloys do. Therefore, in choosing from these materials, one must decide which properties are most important for a given structural design.

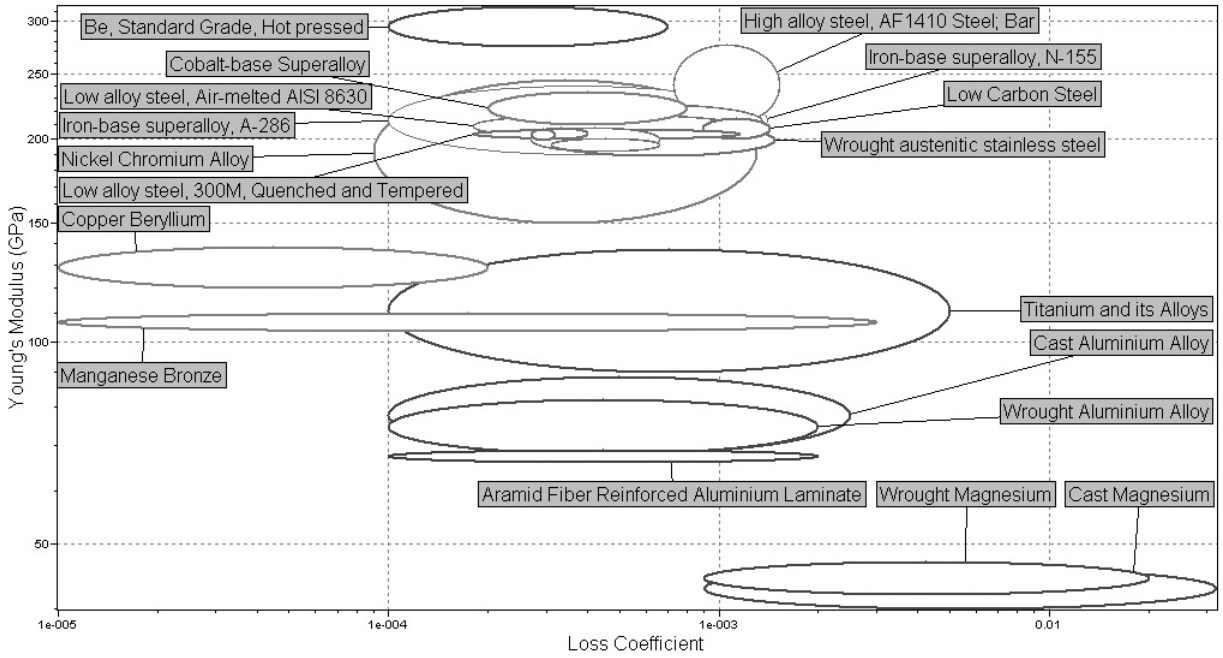

Figure 1: Materials selection chart with Young's modulus plotted against the damping loss coefficient for various aerospace materials. (created using *CES Selector 4.0* computer software)

It is obvious that a structural material containing a significant inherent vibration damping capability and strength would be of great interest and benefit to the engineering community, especially if that material were comprised of popular structural materials currently in use. Therefore, in following with this theme, the goal of this thesis project was to create a multifunctional metal matrix composite discontinuously-reinforced with piezoelectric ceramic particles. It is proposed that a homogeneous dispersion of piezoelectric ceramic particles within a metallic matrix will provide a form of passive vibration damping capability through the conversion of elastic strain to electrical energy to heat by resistive heating at the particle/matrix interface. Additionally, the matrix is further strengthened through common dispersion strengthening mechanisms (dislocation hindering) resulting in the multifunctionality of the composite.

Evidence has shown that the addition of piezoelectric particles to a ceramic phase actually serves to enhance the overall toughness of that phase.[4-6] This is due to the fact that part of the mechanical energy that causes crack extension is transformed into electrical energy and dissipated by domain wall motion in the piezoelectric particles.[7-10] It is believed that perhaps the

addition of piezoelectric particles to a metallic phase (as in our material) will also serve to enhance the material's overall toughness in a similar manner as for a ceramic phase.

This thesis work has been two-fold. The first part consisted of using mechanical alloying as a processing means to synthesis the said piezoelectric ceramic reinforced metal matrix composite. The ultimate goal was to acquire enough composite powder to have it consolidated into a bulk form from which material specimens could be machined and vibration damping tests could be performed. This stemmed from the realization that a relatively quick-and-dirty processing means (such as mechanical alloying) would allow us to rapidly produce composite powder specimens in sufficient quantity to have it consolidated. This would allow for the actual real-world testing of the material to determine whether or not the addition of a piezoelectric ceramic phase actually provides any enhancement to overall damping capability.

The second part of this thesis project consisted of the development of a mathematical model that could be used to predict the composite elastic modulus and damping capability of any discontinuous piezoelectric ceramic reinforced metal matrix composite system. It was hoped that the model could be generalized in order to explore the effect that reinforcement type, shape, and aspect ratio had on the overall damping effectiveness of several material systems.

Thesis project results will be presented summarizing findings from the initial stages of this project up to its current state.

1.2 Vibration Damping and Materials

1.2.1 Definition and Quantification

Damping capacity is a measure of a material's ability to convert mechanical vibration energy into some other form of energy, usually in the form of heat. All materials possess some level of inherent internal damping capability, although usually on a very small scale. A material's damping ability is quantified by deforming a specimen elastically through some given cycle and measuring the ratio of dissipated energy to supplied energy. This ratio is termed the material loss factor or loss coefficient (η) and may also be referred to as internal friction, the loss tangent ($\tan \phi$), inverse quality factor (Q^{-1}), specific damping capacity (ψ), or the logarithmic decrement (δ).[11-13] These various quantifications are a product of the specific type of damping

measurement employed, mode of vibration operation, and geometry of the test specimen. Accordingly, they are not exactly equivalent in most cases due to the experimental methods used to obtain them and detail for the derivation of each will not be given here.

As long as a material is deformed within its elastic limits and the damping capacity is relatively small, the above measures of damping (except δ) can be related by the following equation.[11]

$$\tan\phi = Q^{-1} = \eta = \psi / 2\pi \qquad [1]$$

There are several methods of determining the damping characteristics of a given material and each method can be characterized based on the type of deformation the material specimen undergoes during the given test procedure. The two basic types include dilatational deformation in which the specimen undergoes a volume change without shape change, and shear deformation in which the specimen shape changes without any change in volume.[13] The specific test method used to obtain material damping information will ultimately depend on the type of material in question. Due to the wide range of possible test methods and variances for each material, focus here will only be placed on tests used to determine the damping characteristics of metal-based materials which are common in structural applications.

Test methods used to quantify damping in metallic materials can be grouped into two main categories according to the mode of deformation that is used. A typical dilatational deformation method utilizes a time domain based flexural test in which a cantilever beam is bent and the transient vibration settling time is recorded. Damped cantilever beam theory is then used to curve-fit or back out the resultant damping capability of the particular specimen.[13] A typical shear deformation test method involves oscillating a cylindrical specimen in torsion at various frequencies to produce states of pure shear. Displacement and transient vibration settling time are measured and damping factors are calculated according to test geometry and theory.[14] Additionally, temperature may be incorporated into both types of tests in order to monitor damping capability over a range of conditions.

1.2.2 Damping Mechanisms

There are a number of different internal energy transformational mechanisms that contribute to a material's overall damping capacity which depend on the specifics of the said material. In most all of these mechanisms, damping is achieved through the conversion of mechanical energy into thermal energy. In metallic materials, for instance, various contributing factors to damping include the amount and type of crystal defects present, grain boundary size and sliding, dislocation motion, plastic zone size, phase transformations, thermomechanical effects, magnetoelastic phenomena, and stress-induced ordering.[12,13]

As compared to metals and ceramics, polymeric materials posses the highest levels of internal damping simply due to their viscoelastic nature. Rearrangement of polymer chains and bond rotations lead to the dissipation of energy as heat. Polymers are obviously not ideal structural materials however due to their low strength and creep susceptibility. In general, damping tends to decrease with increasing material strength.

Figure 2 shows a materials selection plot with various materials plotted against their inherent damping coefficients and yield strengths. A range of values is shown for each material class representing an overall spectrum of materials for each. As can be seen, metals and ceramics tend to have lower damping coefficient values as opposed to foams, natural materials (wood), and polymeric materials; however they tend to be stronger and are more obvious choices for bulk singular or composite structural components. Thus a trade-off exists between material damping and overall strength.

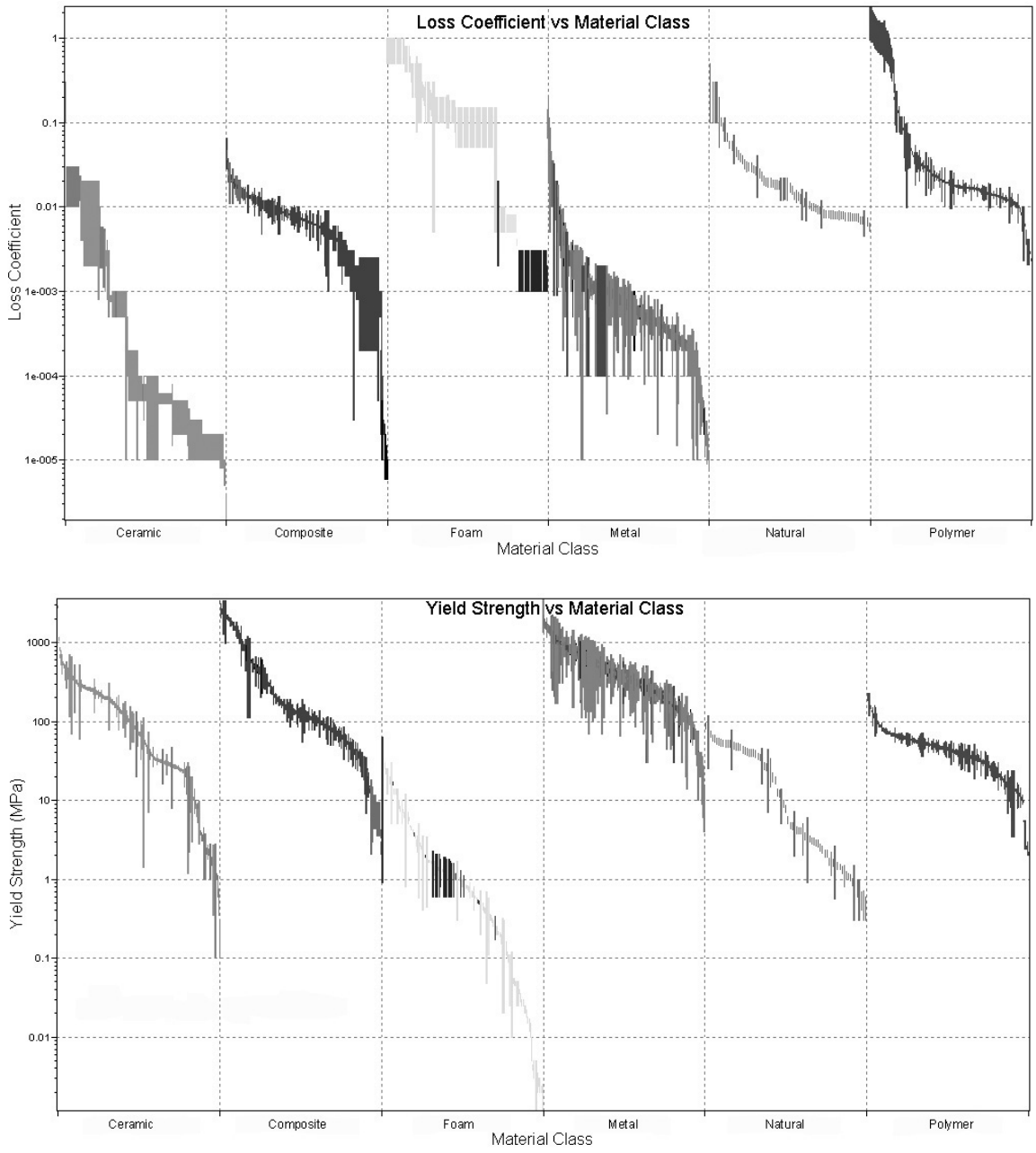

Figure 2: Materials selection charts showing yield strengths and damping loss coefficients for several families of materials. (created using *CES Selector 4.0* computer software)

1.2.3 Classification of Damping Materials

There are two broad categories in which all damping materials can be classified: passive and/or active. Passive damping materials provide damping capabilities simply by being present

on or within a structure. That is, they dampen simply because they are subjected to vibration or impact loading. On the other hand, active damping materials provide damping services on-command at critical structural levels. This is usually accomplished by some sort of sensor or actuator that measures the presence of mechanical vibration on or in a system and instructs the damping material to respond accordingly.

There exist many different types of engineering materials that are used for damping purposes. Therefore, it is beneficial to provide a general overview of these different types and the mechanisms that are involved with each one's damping capability. This summary should by no means be taken as a complete listing of all of these materials.

1.2.3.1 Viscoelastic Materials

Viscoeleastic damping is exhibited by two groups of materials: polymers and glasses. Vibration damping in polymers is accomplished by atomic bond rotation (generating configurational heat) during deformation and by the relaxation and recovery of polymer network chains after they have been mechanically deformed.[15] As can be seen in Figure 2, polymers have the largest inherent damping capacity on average than that of any other material class. However, they tend to have low modulus values and their damping capacity is greatly dependent upon temperature.[16]

Glasses are composed of inorganic oxides that exhibit short-term order and long-term disorder and damping is accommodated by relaxation processes upon deformation of the lattice. As is seen in Figure 2, glasses (ceramic category) tend to have damping coefficients on the order of composite and metallic materials but have strengths greater than that of polymers on average. As with polymers, glasses can creep over time at elevated temperatures thus restricting their use in some applications. Also, glasses tend to be brittle and are subject to thermal and mechanical shock.[15]

As a singular damping component, polymeric materials have been extensively used to provide acoustic and mechanical vibration reduction to a great number of structures. Probably the best example of this is the use of different types of rubber and other viscoelastic materials in constrained layer damping (CLD) at critical structural joints and fixtures in building construction and machinery that tend to see increased mechanical vibrations. Typically in a CLD application,

a viscoelastic material is sandwiched between the vibrating structure and a stiff material (usually metallic or ceramic) resulting in an increase in strain and hence damping in the viscoeleastic material.

Gradient polymeric materials have recently seen increased use in damping applications.[17] In these types of materials, the mechanical properties (E,η) vary along the thickness of the overall material, thereby providing damping and strength capabilities in a gradient manner. This allows for an extension of the possible damping range for the given material and to provide specific mechanical requirements for certain regions within the material.

Liquid crystal polymers (LCPs) have been in existence for quite some time (e.g. Kevlar fiber); however they have just recently been utilized in traditional damping applications.[17] LCPs are similar in chemistry to polymers but have an additional phase in which molecules lie somewhere between a disordered liquid and an ordered solid. LCPs are anisotropic in their mesophase, but will turn isotropic in the rubbery state. Damping arises when the rod-like molecules in the mesophase align themselves upon deformation into the isotropic phase.

There are some mentionable drawbacks to using viscoelastic materials in damping applications. First off, damping is usually very sensitive to temperature in both polymers and glasses. Second, these materials are often added to an existing structure for damping aid therefore increasing overall mass (albeit probably small) and cost for the entire structure. Further, damping capability is provided on top of the structure and not from internally within where vibrations resonate, thereby resulting in a less-effective transformation of energy.

1.2.3.2 Metallic Materials

There are a great number of metallic materials that exhibit a significant level of inherent damping ability. Most of these materials are either alloys or composites usually consisting of multiple phases. It is rare that a pure metal will posses any real damping capability, however exceptions do occur. Figure 3 shows a plot of logarithmic decrement versus tensile strength for various metals and alloys (adapted from Suda et al). It can be seen that, in general, lower tensile strength metals and alloys tend to have a larger logarithmic decrement (and vice versa).

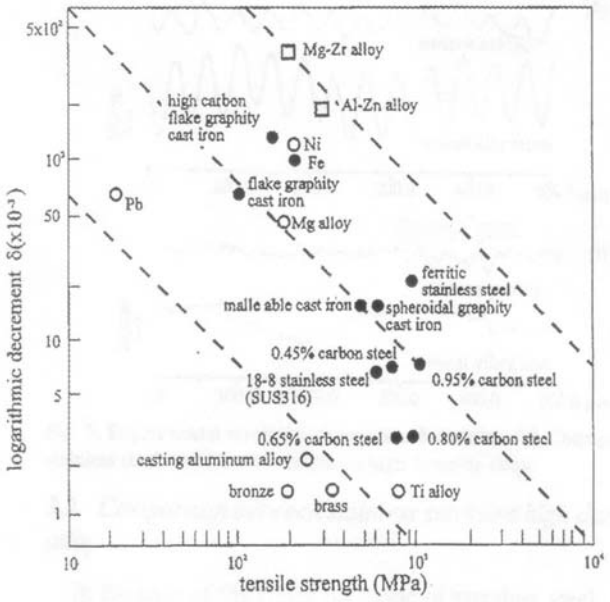

Figure 3: Plot of logarithmic decrement versus tensile strength for various metals and alloys. [18]

Some of the dominant mechanisms that contribute to damping in metallic materials include the amount and type of crystal defects present, grain boundary size and sliding motion under deformation, dislocation motion, thermoelastic effects, magnetoelastic phenomena, and stress-induced ordering.[12,13] Defects that can contribute to damping include point-, line-, bulk-, and surface-defects.[12] In general, the greater the amount of defects, the higher the damping ability for a given material due to increased energy accommodation. Therefore, it can be inferred that a good damping ability may actually prove harmful to the material if a large number of defects are present. Grain boundary size and dislocation motion are interrelated due to their correlation with one another and the larger the grain boundary size, the easier and more-freely dislocations can move and thus provide a source of energy transfer for damping capability.

There are several distinct groups that metallic damping materials can be classified into and the largest ones will now be summarized.

Particulate Reinforced Metal Matrix Composites

It has long been known that a distribution of particulates within a metallic matrix will provide a higher level of internal damping capability than that exhibited by the base matrix alone. Several metal matrix composites exploit these particulate-induced damping mechanisms

including high-carbon steels, cast irons, and aluminum and magnesium matrix composites containing graphite, SiC, or Al_2O_3 inclusions.

Increased particulate damping is due to several reasons and may be attributed to numerous damping mechanisms, the nature of which depends on the size, shape, chemistry, and mechanical properties of the reinforcement. Some of these damping mechanisms include: 1) thermoelestic damping in which local stress concentrations form around particulate inclusions resulting in thermal gradient energy losses; 2) thermal expansion mismatch in which the differences in CTE between the matrix and reinforcement cause dislocation generation around the particulates to accommodate thermal stress buildup; and 3) interface damping in which the crystal structure distortion of the metal matrix surrounding the particulates results in particle-matrix interfacial slip and frictional energy loss (damping). [11,14,19]

High-damping metal matrix composites (HDMMCs) hold an advantage over traditional viscoelastic damping materials due to their wide range of temperature use, strength, and creep resistance. Additionally, HDMMCs are often advantageous over traditional structural metals and alloys due to their increased damping, increased strength, and sometimes lower density that is related to the presence of a reinforcing phase.

Metallic Foams

Metallic foams are often very practical choices for structural applications due to their low mass and good damping and sound absorption capabilities. It is well known that the presence of large amounts of porosity in metallic foams contributes to damping due to stress concentration and mode conversion around pores and that damping ability is inversely proportional to foam density.[20,21] Additionally, the porosity in metallic foams tends to result in increased levels of micro cracks and dislocation densities around the pore walls that serves to further enhance damping ability. It has also been shown by Jiejun et al that damping ability, tensile strength, and stiffness of an aluminum foam can be increased even further if it is reinforced with SiC particulates.[21] This is not surprising and is a prime example of the tailoring that can be done to a material in order to meet some given multifunctional need.

Shape Memory Alloys

Shape memory alloys (SMAs) have been used in many different damping applications including vibration reduction in snow skis, shock wave absorption in armor and bullet proofing

structures, and seismic damping in civil constructions. The two most common families of SMAs that are utilized in passive damping applications include nickel-titanium alloys and copper-zinc-aluminum alloys. These alloys can exhibit passive damping capability through hysteretic behavior associated with a martensitic phase transformation. As a SMA is cyclically stressed or vibrated, a reversible martensitic phase transformation provides damping by inducing crystallographic reorientation and/or dislocation generation. Mechanical damping is then facilitated by energy dissipation as frictional heat. Additionally, the overall damping capability of SMAs is influenced by temperature as well as cyclic strain amplitude and frequency. [22-24]

1.2.3.3 Piezoelectric Damping Materials

Piezoelectric damping materials represent a large class of composite materials that provide active or passive vibration damping capability that depends on the internal mechanical layout of the composite. Regardless of whether damping is achieved actively or passively the overall damping mechanism is the same – mechanical energy is dissipated as resistive heat through the piezoelectric effect. Much work has been put into developing active piezoelectric damping composites by embedding continuous piezoelectric ceramic rods, fibers, and/or plates within a viscoelastic polymer matrix.[25,26] The piezoelectric elements are oriented in such a way as to provide some specifically-activated countermeasure for shear or compressive stresses in certain directions within the overall composite material. When vibration is induced within the composite, a sensor of some sort actuates and in-turn electrically activates the piezoelectric ceramic elements. Figure 4 shows one possible layout of this type of composite in which composite damping capability is increased in the z-direction due to the presence of aligned piezoelectric ceramic rods.

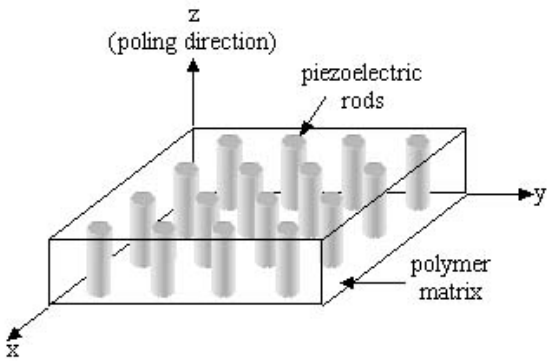

Figure 4: Schematic of one possible layout of an active piezoelectric ceramic composite.

Another group of piezoelectric damped composites that have been of interest are passively-damped, polymer matrix composites consisting of a discontinuous dispersion of piezoelectric ceramic particles and carbon black.[27-29] The mode of damping in these types of composite systems is the transformation of mechanical energy from the polymer matrix to the piezoelectric ceramic particles which is then transformed into electrical energy and dissipated as resistive heat into the conducting carbon black powder. It has been found that a noticeable increase in damping capability is not found in these composites unless the polymer matrix is loaded with at least 50 volume % of piezoelectric ceramic particles. This isn't particularly surprising however since the polymer matrix already contains a relatively large inherent damping ability, thus requiring a large barrier that must be overcome to further increase damping. Figure 5 (a) shows a schematic of this type of composite damping material while (b) shows an equivalent circuit for the mechanism behind damping in this type of composite.

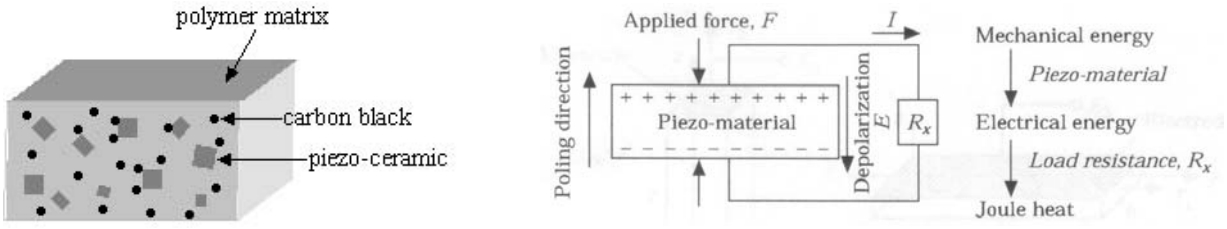

(a) (b)

Figure 5: (a) A schematic of a polymer matrix composite containing a discontinuous dispersion of piezoelectric ceramic particles and carbon black powder and (b) an equivalent circuit for its working damping mechanism.[16]

The damping mechanism behind the composite material that is the subject of this thesis is based on concept represented in Figure 5. We instead utilize a metallic matrix and the inherent electrical conductivity of the matrix is used to dissipate electrical energy in the form of Joule heat.

1.3 Electrical Phenomena in $BaTiO_3$

1.3.1 Introduction

Electrical phenomena is classified here as any dipolar change within a material due to outside electrical, mechanical, or thermal stimuli. Using this definition we can readily see that a great deal of materials (if not all) can potentially possess these forms of dipolar changeability. It is then obvious that many potential areas of application exist for these materials; however the overall usefulness of them in real-world situations is limited to their phenomenological magnitude of response. One such material that has shown high levels of dipolar response is barium titanate ($BaTiO_3$). Barium titanate is a piezoelectric material that has seen much use during the past half century in transducer and sensor applications in which its electromechanical nature has been exploited to detect motion or electrical disturbances within structures and devices (through field generation) and transform mechanical energy to electrical energy (or vise versa). Different forms of electrical phenomena will now be explored, ending with their importance to the usefulness of $BaTiO_3$.

1.3.2 Ferroelectricity and Pyroelectricity

Ferroelectric materials are a class of dielectrics that exhibit spontaneous polarization on an atomic level without the presence of an electric field or outside stimuli. The polarity of a given ferroelectric crystal can be made to switch direction by means of an applied electric field and is thus reversible, allowing great flexibility in electrical applications. In all ferroelectric materials there exists a nonpolar state that is only slightly less stable than the polar form, so upon a change in temperature the stability of the structure shifts to favor the nonpolar form. The temperature at which this inversion takes place is termed the Curie temperature and is named after Pierre and Jacques Curie due to their discovery of piezoelectricity in 1880.[30]

Pyroelectric materials are defined by a change in dipole magnitude with temperature. Therefore, all ferroelectric materials must be pyroelectric by definition. Specifically, electric dipoles within a ferroelectric material will become spontaneously aligned in some preferred orientation to display an overall non-zero net charge. This is a result of interactions between adjacent unit cells within the material that cause permanent dipoles to mutually align in the same direction.[31] Similarly, the pyroelectric effect occurs when a ferroelectric material is uniformly heated resulting in a change in dipole magnitude owing to atomic rearrangement within the crystalline unit cell.

While the pyroelectric effect is present in all ferroelectric materials, the strength and relative usefulness of it for electromechanical applications depends on the nature of phase transitions and relative orientation of unit cells within a crystal. A first order phase transition is one in which properties such as polarization and lattice constants change discontinuously, while a second order transition is defined by a continuous and gradual change in properties by atomic rearrangement. This can be thought of as a sudden change in atomic positions within a unit cell (1^{st} order) versus one in which atoms gradually shift and orient themselves until reaching a stabilized state (2^{nd} order). Additionally, the unit cells of a pyroelectric crystal must be poled in the same direction in order for a net charge to result, so any crystals that contain dipolar arrangements in compensating directions cannot be pyroelectric.

1.3.3 Piezoelectricity

Piezoelectricity refers to an electromechanical phenomenon in which an electric field is induced within a material from an applied force, or vice versa. It was first discovered in 1880 by Pierre and Jacques Curie by successfully measuring surface charges appearing on specially prepared crystals of tourmaline and quartz, among others.[30] Due to its direct electrical-mechanical nature, piezoelectricity is perhaps the most beneficial form of all electrical phenomena for transducer and sensory applications.

Physically, as a piezoelectric material is stressed, atomic positions change within unit cells depending on whether the stress is in compression or tension. This change in atomic position in turn alters the magnitude of dipolar arrangements leading to the buildup of a net

surface charge in the crystal. Figure 6 shows an example of the piezoelectric effect in a material and the voltage that is generated based on a compressive stress.

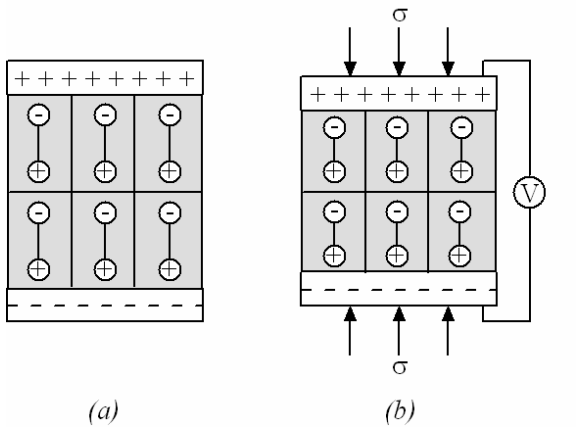

Figure 6: Schematic showing the direct piezoelectric effect.
Dipolar arrangements within a ferroelectric material *(a)* in an unstressed state and *(b)* in a stressed state resulting in a surface charge buildup and a generated voltage.

For most solid materials, an applied stress σ simply causes a proportional strain ε which is related by the elastic modulus Y by the simple equation,

$$\sigma = Y\varepsilon \qquad [2]$$

Piezoelectricity is then the additional phenomena of the creation of an electric charge in a material from an applied stress. This is termed the direct piezoelectric effect and the charge is proportional to the applied force, being of opposite sign for tension and compression. The magnitude of this charge is related to the applied stress by,

$$D = \frac{Q}{A} = d\sigma, \qquad [3]$$

where D is the dielectric displacement, Q is the charge, A is area, and d is the piezoelectric constant for a specific material in units of coulombs/Newton.[30] However, a converse effect exists in that an applied electric field E can produce a proportional strain, ε, given by equation [4] where d again is the piezoelectric constant.

$$\varepsilon = dE \qquad [4]$$

Another piezoelectric constant that can be derived from equations [3] and [4] is the g constant. The g constant gives the electric field that is produced for a given material based off an applied stress and is related to the piezoelectric constant d by,

$$g = \frac{d}{\epsilon'} = \frac{d}{K \epsilon_0} \qquad [5]$$

where ϵ' is the permittivity of the material, ϵ_0 is the permittivity of free space, and K is the dielectric constant (ϵ'/ϵ_0).[30]

Another frequently-used factor in piezoelectric behavior is termed the electromechanical coupling factor k. It is basically a measure of the energy conversion efficiency of a piezoelectric material and is always less than one since the conversion is always incomplete. It is defined in terms of k^2 by,

$$k^2 = \frac{electrical\ energy\ converted\ to\ mechanical\ energy}{input\ electrical\ energy}$$

or [6]

$$k^2 = \frac{mechanical\ energy\ converted\ to\ electrical\ energy}{input\ mechanical\ energy}$$

When ranking piezoelectric candidate materials for some specific application, it can be seen that a high d constant is desirable for applications that require motion or large displacement based off of a given stress, whereas a high g constant is advantageous for applications that require high voltage generation from a given stress. Additionally, a large electromechanical coupling factor is beneficial in most all piezoelectric applications since it essentially represents the overall strength of the effect. It should be mentioned that there are a variety of ways in which the previous-mentioned piezoelectric factors can be measured experimentally and the details of these will not be explored here.

1.3.4 Electrical Phenomena and the Polymorphic Crystal Structure of $BaTiO_3$

Barium titanate is a ferroelectric and additionally a pyroelectric material that possesses a relatively large piezoelectric effect as well. It was the first piezoelectric ceramic commercially developed and still sees widespread use in many different applications due to its high electromechanical constant and relative ease of manufacturability. It can exist in two basic crystal structures; a ferroelectric perovskite form and a non-ferroelectric hexagonal form.

Figure 7 shows the ferroelectric nature of a unit cell of the most useful form of $BaTiO_3$, the tetragonal form. The electric dipole moment occurs naturally in $BaTiO_3$ due to the

displacement of the O^{2-} and Ti^{4+} ions from the central axis of the tetragonal unit cell. The ionic dipole vanishes however when barium titanate is heated above its Curie point of 130°C. When this occurs, the O^{2-} and Ti^{4+} ions shift into the symmetric positions and the unit cell becomes cubic perovskite.[31]

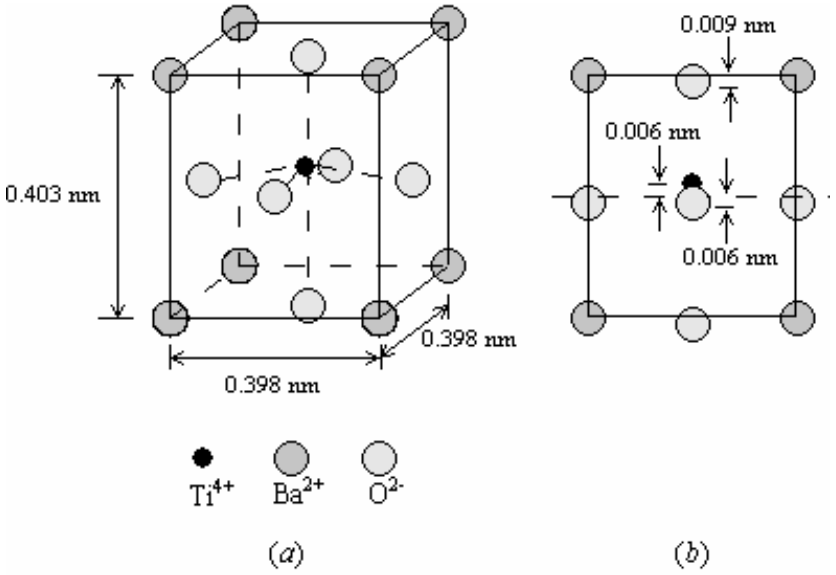

Figure 7: Unit cell of tetragonal barium titanate showing (*a*) atomic positions in an isometric view and (*b*) face view of atomic displacement of O^{2-} and Ti^{4+} ions from the central cell axis resulting in polarization.

Figure 8 shows the various polymorphic crystal structures of $BaTiO_3$ and their transformation temperatures. As can be seen, the higher temperature phase of $BaTiO_3$ has a hexagonal crystal structure which occurs at about 1460°C. Below 1460°C the structure changes to cubic pervoskite, however the hexagonal phase can exist metastably at room temperature. The cubic phase is stable up until the Curie point of about 130°C. The structure then transforms into the tetragonal phase, the most useful piezoelectric phase, and is stable between about 0°C and 130°C. Finally, the lower temperature phases are the orthorhombic phase which is stable between 0°C and -90°C and the rhombohedral phase which is stable below about -90°C.

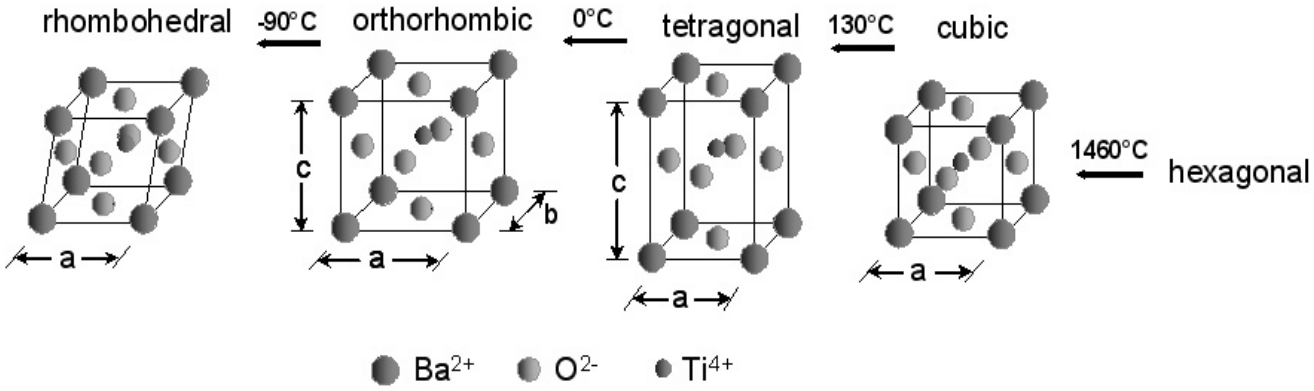

Figure 8: The various polymorphic crystal structures and transformation temperatures of $BaTiO_3$.

As previously mentioned, the most useful piezoelectric form of $BaTiO_3$ is the tetragonal form; therefore it is the goal in most all electromechanical applications to acquire this form. This is not always easy though since the cubic form and hexagonal form can be retained at room temperature. It is suggested by the literature that the cubic phase can be heat treated in order to obtain the tetragonal phase, but specific heat profiles have not been found. Additionally, the cubic phase can be reverted into the tetragonal phase with sufficient applied pressure or the appropriate poling electrical field.

1.4 The Eshelby Approach to Composite Modeling

1.4.1 Introduction

Any inhomogeneous composite will contain internal stresses that result from the nonuniform nature of the material itself. The magnitude of the internal stress depends on the composition of the composite and the degree of its inhomogeneity. For a composite that is comprised of two or more distinct constituents with different stiffnesses, these internal stresses will tend to be quite large and on a magnitude that shouldn't be ignored during composite mechanical analyses.

For the most part, structural composite materials are comprised of two or more phases with inherently different mechanical and/or chemical properties. These may include both continuously-reinforced composites such as laminate or fiber + matrix, and discontinuously-

reinforced composites such as whisker or particle + matrix. Regardless of the type of composite, dissimilar internal stresses are induced during mechanical or thermal loading of the material due to differences in mechanical properties (stiffness,CTE,etc.) of the constituents and variances in shape mismatch between the phases. It can easily be seen that the analysis and accurate prediction of these internal composite stresses are required in order to accurately predict the mechanical behavior of any composite.

While many efforts have transpired over the years to accurately account for internal stresses in discontinuously-reinforced composites, most proved too tedious to be of any practical use due to the complex mathematical computations that were involved. These mathematical complexities however were circumvented by a unique and ingenious method that was pioneered by J.D. Eshelby in the 1950s.[32]

Eshelby's technique was particularly unique in that he represented actual discontinuous composite inclusions by ones comprised of the matrix material instead of a mechanically dissimilar one. He then formulated a method to determine the misfit strain associated with the equivalent homogeneous inclusion that resulted in the same surrounding stress field as for the actual inclusion. In this manner, he was able to fully predict the mechanical response of the matrix to the inclusion during some stressed state.

1.4.2 Specifics of the Equivalent Inclusion Method

Eshelby developed a means to quantify the local inclusion stresses in mechanically-dissimilar composites by envisioning a series of cutting and welding thought experiments. Specifically, he visualized what would happen when a piece of an unstressed isotropic medium were cut, elastically transformed in some manner, and then welded back into the hole from where it came.[32] He realized that, depending on the shape of the cut piece of matrix, the strains in the surrounding non-transformed matrix could be quite complex and difficult to analyze (Figure 9a). He also realized that the choice of an ellipsoidal shape would make the stress/strain analysis much simpler because it is unique in that an ellipsoid, when elastically stressed, will contain a uniform stress at all points within it (Figure 9b).[1]

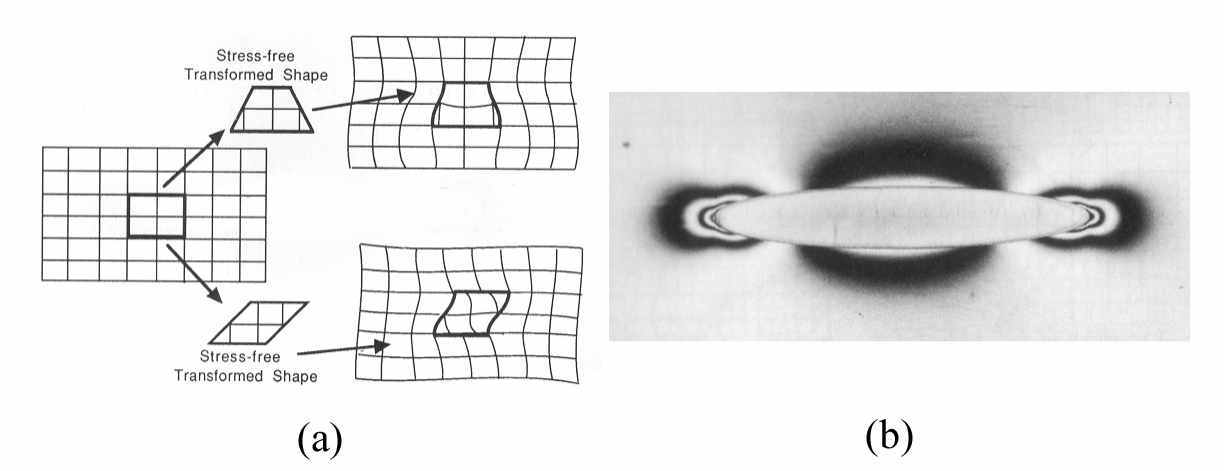

Figure 9: (a) Displacement maps for two different stress-free shape transformations resulting in complex strain fields (grid lines) both in and surrounding the shapes. (b) Stress fields (dark fringe lines) associated with an axially-compressed ellipsoidal inclusion within a matrix. Notice how the stress fluctuates in the matrix around the center and ends of the inclusion, whereas it is uniform within the inclusion. [1]

Figure 10 shows the thought experiment that led to Eshelby's equivalent inclusion method. As can be seen, an ellipsoid of an isotropic infinite matrix material is cut and removed from the homogeneous surroundings. It then undergoes a stress-free elastic transformation in which it is strained to a new transformation strain, ε^T (sometimes called the eigenstrain[33]). Next, surface tractions are applied to the transformed shape to bring it back to its original unstrained state and it is then welded into the hole from where it came. The surface tractions are then removed and a new equilibrium is reached between the matrix and the inclusion at a new constrained strain, ε^C. [1]

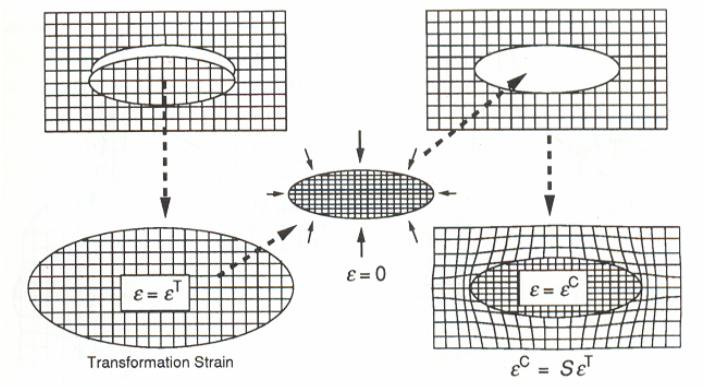

Figure 10: Eshelby's cutting and welding thought experiment resulting in his formulation for the equivalent inclusion method. [1]

Hooke's Law can then be used to calculate the stress within the inclusion since it is strained uniformly throughout by the equation

$$\sigma_I = C_M(\varepsilon^C - \varepsilon^T) \qquad [7]$$

where C_M is the stiffness tensor of the material and σ_I is the stress within a single inclusion. If the inclusion undergoes a shape change to the transformed strain ε^T, then knowledge of the final constrained strain ε^C is all that is needed to find σ_I. [1]

Eshelby formulated a unique approach for determining the constrained strain from the transformed strain by means of a tensor that takes the inclusion aspect ratio, shape, and Poisson's ratio of the matrix into account. This tensor is termed the "Eshelby shape tensor", *S*, and is related to the constrained and transformed strain by the following equation.†

$$\varepsilon^C = S\varepsilon^T \qquad [8]$$

The inclusion stress can now be written in terms of the stress-free shape mismatch by substituting equation [8] in for [7] giving

$$\sigma_I = C_M(S - I)\varepsilon^T \qquad [9]$$

where *I* is the identity matrix.

1.4.3 The Uniqueness of Eshelby's Equivalent Inclusion Method

The most important aspect of Eshelby's equivalent inclusion method coupled with the Eshelby shape tensor is that for any elastically inhomogeneous composite system in which there are inclusions present, one can envision an equivalent elastically homogeneous one that will generate the same matrix and inclusion stress fields as the real composite. This means that the inclusion stress can be represented in terms of both the equivalent composite in which the inclusion is made of the same material as the matrix and the real composite in which the inclusion is made of a separate material from the matrix. Figure 11 shows Eshelby's cutting-and-welding thought process in comparing the real composite and the equivalent composite.

† The determination of *S* for different inclusion shapes can be quite complex and details for several different ones can be found in Mura.[31]

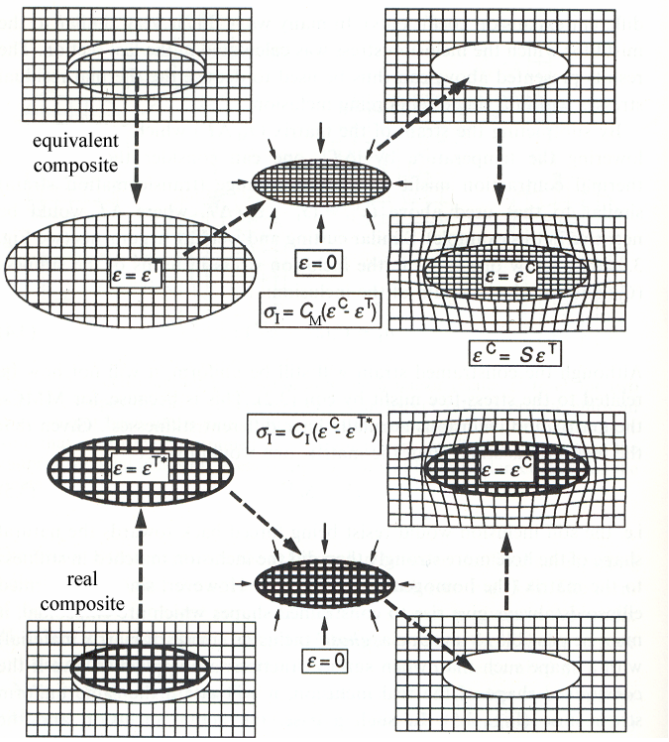

Figure 11: Comparison between Eshelby's cutting-and-welding thought experiment for both the real and equivalent composites. [1]

If the transformation strain in the real inclusion is represented by ε^{T*} and the inclusion stiffness tensor is C_I, then the inclusion stress in both the equivalent and real composites can be given by

$$\sigma_I = C_M(\varepsilon^C - \varepsilon^T) \quad - equivalent\ composite \qquad [10]$$

$$\sigma_I = C_I(\varepsilon^C - \varepsilon^{T*}) \quad - real\ composite \qquad [11]$$

or

$$C_M(S - I)\varepsilon^T = C_I(S\varepsilon^T - \varepsilon^{T*}) \qquad [12]$$

Therefore, it is seen that any elastic shape misfit in a real composite (ε^{T*}) coupled with knowledge of phase stiffnesses and inclusion shape can lead to the prediction of an equivalent elastic shape misfit in a matrix inclusion (ε^T) by

$$\varepsilon^T = [(C_I - C_M)S + C_M]^{-1} C_I \varepsilon^{T*} \qquad [13]$$

The stress within one inclusion is then,

$$\begin{aligned}\sigma_I &= C_M(S-I)\varepsilon^T \\ &= C_M(S-I)[(C_I - C_M)S + C_M]^{-1} C_I \varepsilon^{T*}\end{aligned} \qquad [14]$$

Equation [14] is important in that it represents the underlying premise for why the Eshelby method is so unique; it allows one to predict the stress in an inclusion without detailed knowledge of the corresponding complicated stresses in the matrix.

1.4.4 Application of the Eshelby Equivalent Inclusion Technique

We are usually not interested in knowing the internal stress within one single inclusion within an unloaded composite; rather, we are interested in the average stress in the all of the inclusions within a loaded composite as a whole. In order to obtain expressions that allow for this calculation, the equations in the previous section must first be altered to include the volume fraction of inclusions within the composite and the effect that an applied load has on the composite mechanical behavior.

1.4.4.1 The Dilute Loaded Composite Case

If we analyze what happens to a loaded elastically homogeneous infinite composite in which a singular inclusion is modeled as the equivalent inclusion case, the strain (ε^A) should be the same everywhere. The total stress at any point within the composite is simply the sum of the applied stress, σ_A, and the inclusion stress calculated in equation [10]. This is given by

$$\sigma_I + \sigma^A = C_M(\varepsilon^C - \varepsilon^T) + C_M \varepsilon^A \qquad [15]$$

where

$$\sigma_{\mathrm{A}} = C_M \varepsilon^A \qquad [16]$$

The mechanical behavior in a real composite will obviously be quite different than that of the equivalent inclusion case (see Figure 12). The beauty of this technique though is that you have freedom over the choice of the original shape of the equivalent inclusion so that it is always possible to select a shape that will result in an equivalent stress-free misfit (ε^T) that will be equal to the stress in the real inclusion. Because of this, the constrained shape change and stress in a real inclusion will be identical to the equivalent one in a composite loaded by an applied stress.

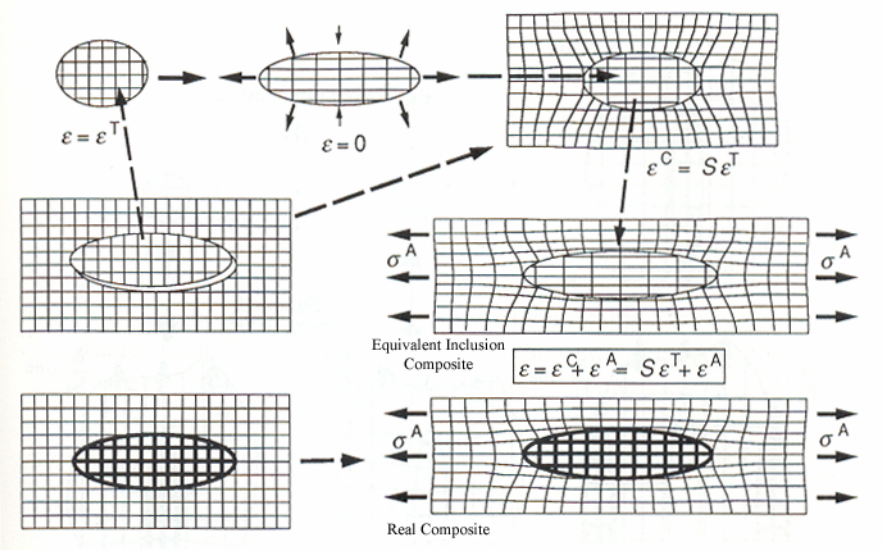

Figure 12: Comparison between a loaded real composite and one which contains an equivalent inclusion. The usefulness of this technique is shown in that the total constrained strain is equal in both cases. [1]

The total constrained shape change (ε^C_{total}) will be equal to the constrained strain in the inclusion before loading plus the applied strain, given by

$$\varepsilon^C_{total} = \varepsilon^C + \varepsilon^A \quad - \textit{equivalent and real inclusions} \qquad [17]$$

Similarly, the inclusion stress must be the same in the equivalent inclusion and the real inclusion by definition. The total inclusion stress (σ^I_{total}) is actually the sum of the inclusion stress given by equation [10] and the applied stress to the composite given by equation [16] and is given by

$$\sigma^I_{total} = \sigma_I + \sigma_A = C_M(\varepsilon^C + \varepsilon^A - \varepsilon^T) \quad - \textit{equivalent and real inclusion} \qquad [18]$$

The total real inclusion stress can also be expressed in terms of Hooke's Law by

$$\sigma^I_{total} = C_I(\varepsilon^C + \varepsilon^A) \quad - \textit{real inclusion} \qquad [19]$$

Now, by combining equations [18], [19], and [8] an expression for the transformation strain (shape misfit) for the equivalent inclusion can be given by

$$\varepsilon^T = -[(C_I - C_M)S + C_M]^{-1}(C_I - C_M)\varepsilon^A \qquad [20]$$

Using equations [9] and [20] and substituting into equation [18], we arrive at an expression for the total inclusion stress (both real and equivalent) in terms of applied composite strain, constituent stiffnesses, and size and shape of the inclusion.

$$\sigma_{total}^{I} = \sigma_I + \sigma^A = -C_M(S-I)[(C_I - C_M)S + C_M]^{-1}(C_I - C_M)\varepsilon^A + C_M\varepsilon^A \qquad [21]$$

Equation [21] is an important result in that the real inclusion stress can always be calculated with knowledge of the applied strain, inclusion size and shape, and phase stiffnesses.[1]

1.4.4.2 The non-Dilute Loaded Composite Case

It is a bit more difficult to model non-dilute composites because it is necessary to account for the effect of many different inclusions at once. The presence of multiple inclusions influences not only the overall matrix mechanical behavior, but also the elastic fields of each other. One way to account for the overall effect of multiple inclusions is to deal with the average of the stresses in constituent phases. This "mean field"‡ approach was first proposed by Mori and Tanaka[34] and has since been utilized in several other composite analyses. [35-37]

The important final result of the mean field approach is the development of constituent mean internal stresses. The mean internal stress of the matrix $\langle\sigma\rangle_M$ and the inclusions $\langle\sigma\rangle_I$ can be thought of as background stresses that serve to partition between the phases. Specifically, these mean internal stresses represent the background stress that is felt by one inclusion resulting from the presence of all of the others. They are given by

$$\langle\sigma\rangle_M = -fC_M(S-I)\varepsilon^T \qquad [22]$$

$$\langle\sigma\rangle_I = (1-f)C_M(S-I)\varepsilon^T \qquad [23]$$

where f is the volume fraction of reinforcement (inclusions) and ε^T is given in similar but modified terms as equation [20] by

$$\varepsilon^T = -\{(C_M - C_I)[S - f(S-I)] - C_M\}^{-1}(C_M - C_I)\varepsilon^A \qquad [24]$$

‡ Detailed derivation of the mean field approach will not be given here. Focus will instead be placed on the final result and usefulness of this approach. For a detailed explanation, the reader is directed to these sources.[30,32]

There is a unique relationship between $\langle\sigma\rangle_M$ and $\langle\sigma\rangle_I$ in that their volume weighted values sum to zero.[1] This relationship is given by

$$(1-f)\langle\sigma\rangle_M + f\langle\sigma\rangle_I = 0$$
$$\therefore$$
$$\langle\sigma\rangle_M = -\frac{f}{1-f}\langle\sigma\rangle_I \qquad [25]$$

It has been shown that the average phase stresses can be calculated from the applied composite stress and constituent mean internal stresses.[1] Specifically, the average phase stresses are given by

$$\overline{\sigma}_M = \sigma_A + \langle\sigma\rangle_M$$
$$\textit{and} \qquad [26]$$
$$\overline{\sigma}_I = \sigma_A + \langle\sigma\rangle_I$$

This is an important result in the effort to predict real composite properties. Using the mean field approach, one is able to calculate average composite phase stresses simply from knowledge of the applied stress, volume fraction and shape of reinforcement, and constituent stiffnesses.

1.4.5 Derivation of Composite Stiffness

Using the definition of average phase and mean internal stresses, an expression for the overall composite stiffness can be derived. The composite stiffness, C_C, can be given in terms of the volume averaged composite strain under an applied load, $\overline{\varepsilon}_C^A$, by

$$\sigma^A = C_C\overline{\varepsilon}_C^A = C_C(\varepsilon^A + \langle\varepsilon\rangle_C^A) \qquad [27]$$

where ε^A is the applied strain and $\langle\varepsilon\rangle_C^A$ is the overall mean composite strain composed of the mean matrix strain and volume fraction–weighted constrained strain given by

$$\langle\varepsilon\rangle_C^A = \langle\varepsilon\rangle_M + f\varepsilon^C \qquad [28]$$

Rewriting equation [25] in terms of strains we have

$$(1-f)C_M\langle\varepsilon\rangle_M + fC_M(\langle\varepsilon\rangle_M + \varepsilon^C - \varepsilon^T) = 0$$

and [29]

$$\langle\varepsilon\rangle_M = -f(\varepsilon^C - \varepsilon^T) = 0$$

Substituting the definition of $\langle\varepsilon\rangle_M$ in equation [29] for equation [28] we obtain

$$\langle\varepsilon\rangle_C^A = f\varepsilon^T \quad [30]$$

Therefore, using equation [30] and [27] we can see that the average composite strain is given by

$$\bar{\varepsilon}_C^A = \varepsilon^A + f\varepsilon^T \quad [31]$$

Now, using the expression for ε^T given in equation [24] and substituting into equation [31] we have

$$\bar{\varepsilon}_C^A = \varepsilon^A - f\{(C_M - C_I)[S - f(S-I)] - C_M\}^{-1}(C_M - C_I)\varepsilon^A \quad [32]$$

Substituting equation [32] into equation [27] we get

$$\sigma^A = C_C[C_M{}^{-1}\sigma^A - f\{(C_M - C_I)[S - f(S-I)] - C_M\}^{-1}(C_M - C_I)C_M{}^{-1}\sigma^A] \quad [33]$$

and solving for C_C we finally arrive at an expression for the composite stiffness tensor given by[1]

$$C_C = [C_M{}^{-1} - f\{(C_M - C_I)[S - f(S-I)] - C_M\}^{-1}(C_M - C_I)C_M{}^{-1}]^{-1} \quad [34]$$

The derivation of the composite stiffness tensor is unique in its outcome in that by combining the results of Eshelby's equivalent inclusion technique with the mean field approach, one is able to predict composite mechanical behavior simply through knowledge of constituent stiffnesses and inclusion size, shape, and volume fraction. This is a very powerful technique and serves as the basis for the computational model developed during the course of this graduate work that can be used to predict the damping capabilities of any discontinuously-reinforced metal matrix composite.

1.5 Mechanical Alloying

1.5.1 Definition and History

Mechanical alloying (MA) is a highly-energetic ball milling technique that is used to produce composite metallic powders with intimately mixed microstructures. Specifically, the MA process consists of a dry powder/ball charge (consisting of at least 15v% of a ductile metal) that is placed in a container and excited either by a stirring or shaking/vibrating motion. In any case, microstructural refinement during the MA process occurs due to the repeated welding, fracturing, and rewelding of the dry powder constituents during their impact between ball-ball and/or ball-container collisions.[2,38,39]

Mechanical alloying holds an advantage over traditional ball milling processes in that one is able to produce a material whose internal homogeneity is independent of the initial starting particle size. It is not uncommon to obtain mechanically-alloyed dispersions with less than 1μm interparticle spacing from initial constituent powder sizes of 50-100 μm average diameter.[40]

There are two main differences between the MA process and a traditional ball milling process. First, the MA process occurs in a highly-energetic manner normally utilizing a dry starting powder charge, whereas a traditional ball milling process is somewhat less energetic and often utilizes additional milling surface modification agents to help reduce the amount of interparticle cold welding. Second, the rates of welding and fracturing are about equal in the MA process resulting in a relatively coarse average particle size, whereas average particle sizes in a traditional ball milling process are somewhat smaller due to the increased rate of fracturing versus welding due to the use of milling liquids and surfactants. The equal average rates of welding and fracturing in the MA process is what allows the powder constituents to become so intimately mixed.

Historically, the MA process was first developed in 1966 at the International Nickel Company's (INCO) Paul D. Merica Research Laboratory as part of an effort to create a nickel-base superalloy with a unique combination of intermediate and high temperature strength intended for use in gas turbine applications. Specifically, it was thought that the combination of a γ', $Ni_3(Al,Ti)$ precipitate phase within an oxide dispersion strengthened (ODS) nickel-base superalloy would provide the required range of temperature strength and corrosion resistance

necessary for the high-temperature creep resistance that is required in a gas turbine application. After an extensive research effort, the first successful γ′-strengthened ODS superalloy was successfully created and became known as IN-853.[2,39,41] The composition of IN-853 along with several additional examples of mechanically alloyed nickel-base superalloys in use today can be found in Table I.

Table I: Compositions of Selected MA Alloys (wt%) [42,43]

Alloy	Ni	Cr	Mo	W	Al	Ti	Ta	Zr	B	C	Y_2O_3
IN-853	bal	20.7	--	--	1.5	0.056	--	0.076	0.006	0.056	1.3
MA 753	bal	20.0	--	--	1.5	2.5	--	0.07	0.007	0.05	1.3
MA 754	bal	20.0	--	--	0.3	0.5	--	--	--	0.05	0.6
MA 757	bal	16.0	--	--	4.0	0.5	--	--	--	0.05	0.6
MA 758	bal	30.0	--	--	0.3	0.5	--	--	--	0.05	0.6
MA 760	bal	20.0	2.0	3.5	6.0	--	--	--	--	--	0.95
MA 6000	bal	15.0	2.0	4.0	4.5	2.5	2.0	0.15	0.01	0.05	1.1

It should be said that the MA process evolved during the development of IN-853 due to the shortcomings of popular oxide dispersion strengthening and solid solution strengthening techniques at that time such as mechanical mixing, ignition surface coating, internal oxidation, selective reduction, melt injection, and rapid solidification. These techniques proved inadequate in the creation of a γ′-strengthened ODS superalloy for many different reasons, some of which include impractical initial powder size limitations, extreme powder reactivity, and inhomogeneous interparticle spacing and phase dispersion. [2,38]

The fact that ball milling had previously been used by INCO to coat hard phases such as zirconium oxide and tungsten carbide with softer phases such as nickel and cobalt, coupled with the fact that severely plastically-deformed metallic powders behave in a brittle fashion, led INCO to experiment with the idea of using ball milling as a processing means for a γ′-strengthened ODS superalloy. It was realized that if it were possible to employ a highly-energetic ball milling process that facilitated severe deformation levels required for brittle behavior and fracture of soft materials (such as nickel), then the proper balance of cold welding and fracturing might be

obtained that resulted in a refined internal microstructure of composite powder.[41] This thought process eventually led to the development of mechanical alloying.

1.5.2 Processing Equipment, Methods, and Concerns

There are many different types of mechanical alloying processing equipment including attritor mills, shaker mills, vibratory mills, centrifugal ball mills and conventional-type ball mills. We will focus only on the two most common research-oriented forms, however, the attritor and shaker mills. An attritor mill consists of a stationary tank that can be anywhere from roughly 1 gallon up to about 100 gallons in volume. It contains a central shaft that rotates an impeller within the tank upwards of about 250 rpm. Under these energetic operating conditions, the ball charge is disturbed within the tank in a consistent but random manner that results in composite powder microstructural development with time. Figure 13 shows a common attritor mill, the Szegvari mill.

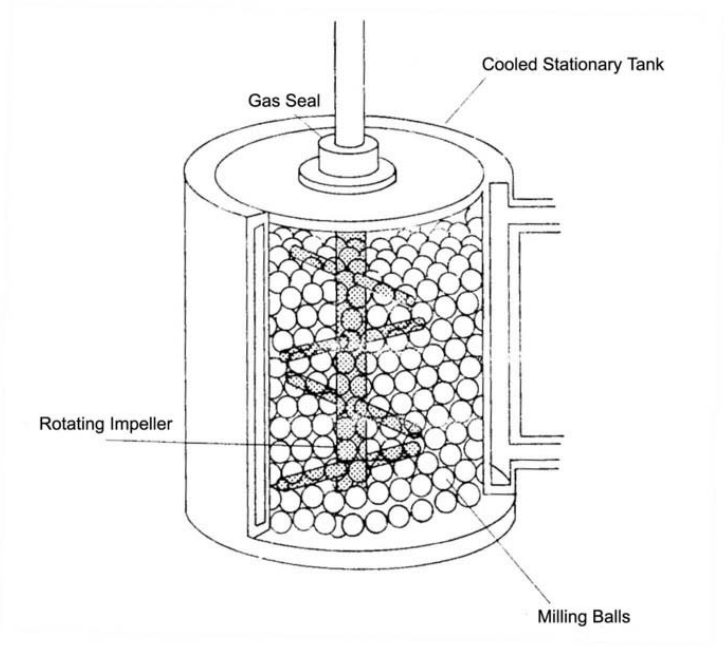

Figure 13: An example of a Szegvari-type attritor grinding mill. [2]

The other main category of smaller-scale MA processing equipment includes shaker mills. These types of mills process powder constituents by continually and violently shaking a container in which ball and powder charge is loaded. Ball-ball and ball-container collisions

continually trap and refine the powder constituents with time ultimately leading to an overall homogeneously dispersed microstructure.[2]

One example of this type of processing equipment is the SPEX mill. The SPEX mill is significantly smaller than the attritor mill and can only process a powder charge of about 10 grams, depending on the density of starting constituents, but is an obvious choice for experimental-type research in which small amounts of powders are all that is required. The SPEX mill shakes the milling container in three-mutually perpendicular directions at about 1200 rpm resulting in powder microstructural refinement with time. A typical SPEX mill is shown in Figure 14.

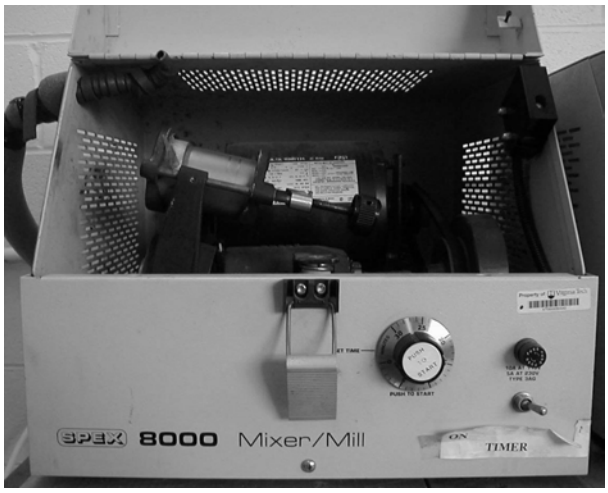

Figure 14: A typical SPEX shaker mill.

There will be some level of contamination in any MA process simply due to its energetic nature. This is due to the fact that during processing, impacts between container and milling balls will result in tiny fractions of milling material that fracture off and disperse into the composite powder through the same means that microstructural refinement occurs. This could lead to harmful contamination of the composite powder depending on what the material is and what types of powders are being processed. Regardless of the type of mechanical alloying process, care should be taken to properly choose the most appropriate type of container and milling media for the given system.

A general guideline to reduce contamination during processing is to use milling media that is made of a similar material as that of the material to be processed. For most mechanical alloying applications, hardened steel milling media is sufficient to reduce contamination during processing. Depending on constituent materials however, it may be beneficial to use milling media made of alumina, zirconia, tungsten carbide, or stainless steel.

In any mechanical alloying process, a balance between cold welding and fracturing is necessary in order for a net-homogeneous composite microstructure to be attained. It is not always easy to obtain this balance, however, due to the many material differences between powder constituents. Starting constituents often range from being very soft and ductile (e.g. lead) to being quite brittle, such as is the case with intermetallics and/or ceramics. Sometimes it is necessary to add a processing control agent to the starting constituents in order to hinder clean surface contact between metallic powders. A reduction in clean surface contact between metallic powders results in less cold-welding and actually promotes fracturing, ultimately resulting in the behavioral balance that is sought. [2]

Another technique that is sometimes used to promote powder fracture as opposed to cold-welding is cryogenic milling. This method is often used in the production of MA lead-based alloys to reduce operating temperatures down into the brittle regime. Cooling the milling container can be achieved in numerous ways, but one popular method is to simply drip liquid nitrogen onto the milling chamber during processing.

1.5.3 Powder Processing and Microstructure

In any mechanical alloying process, starting powder constituents are first blended according to the required stoichiometry for the given composite formulation. They are then placed in the milling container along with the appropriate ball charge and milled for the desired length of time until a steady state of homogeneous dispersion is achieved. In some MA processes, the powders are milled to an intermediate state in order to attain certain properties or to form a metastable phase. Regardless of the processing path, all mechanically alloyed powders must finally be consolidated in some fashion in order to be useable in a bulk form.[40] Figure 15 shows an overall summary of a typical mechanical alloying process and the idea behind microstructural refinement with time.

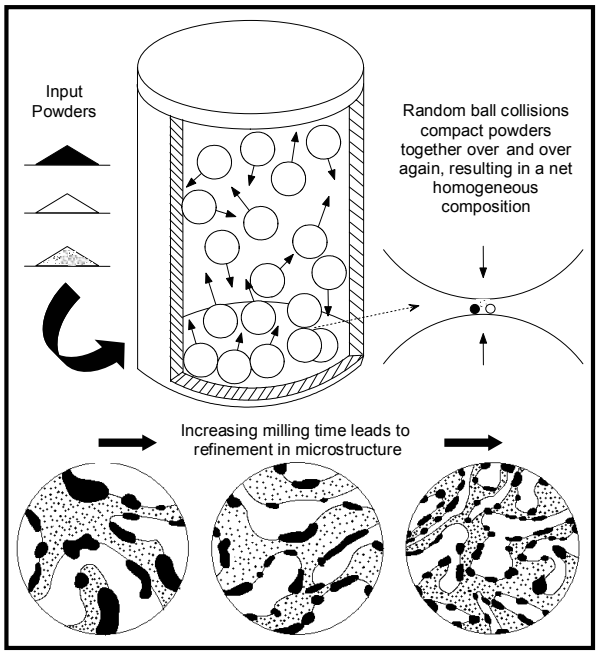

Figure 15: Summary of MA processing and microstructural refinement.

In order to understand the physical phenomena that occur during MA processing it is useful to outline a representation of a typical process into three stages. Figure 16 defines the starting constituents and their deformation behavior that will be used in this specific example. As can be seen, ductile metal powders tend to elongate and flatten after a single ball-powder-ball collision, while more brittle phases, such as intermetallics and dispersoids, tend to fracture into several smaller pieces.

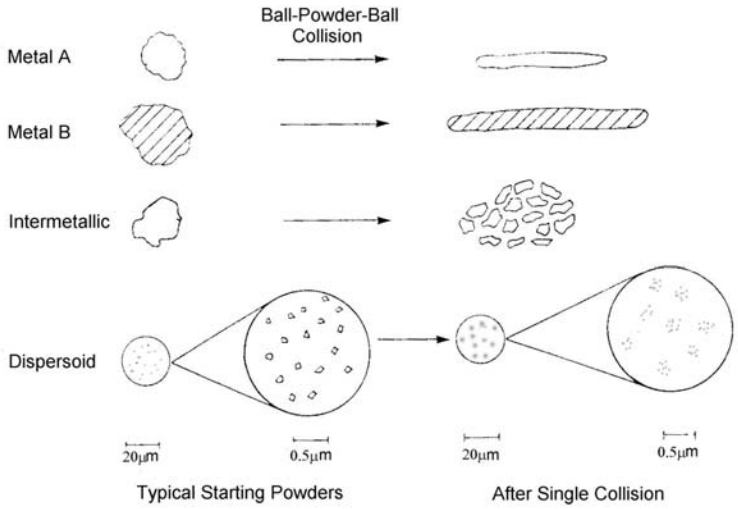

Figure 16: Deformation characteristics of starting powders used in a typical MA process. [2]

1.5.3.1 Early Stage

During the early stage of processing (Figure 17), particles are essentially layered composites comprised of the starting constituents. Composite particles form from a series of repetitive steps during processing. As the metallic phases are flattened during ball collisions and overlap, atomically clean surfaces are placed in contact with one another and subsequently cold-weld together. As this process occurs, brittle constituents (intermetallics and dispersoids) are occluded by the ductile constituents thus becoming trapped along cold-weld interfaces. There is a wide range in particle sizes during this stage and non-welded fragments of starting powders may additionally be present. It should also be noted that lamellae thickness is relatively coarse during this stage as well. [2,38,39,41-45]

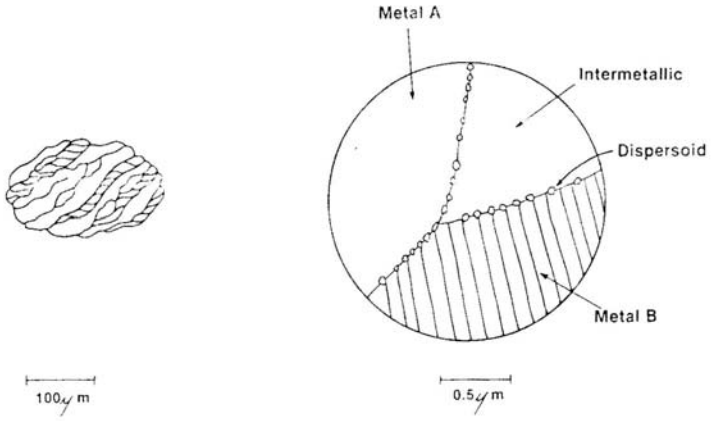

Figure 17: Early stage of processing in which particles are layered composites of starting constituents. [2]

1.5.3.2 Intermediate Stage

The composite powder particles are further refined during this stage of processing due to continual welding and fracturing of excessively work-hardened metallic phases and brittle intermetallics and/or dispersoids. The reduction in particle size, increased microstructural mixing, and elevated temperature of the powder constituents due to the adsorbed kinetic energy of milling balls all help to facilitate the existence of areas of solute dissolution throughout the metallic powder matrix and potentially may lead to areas where new phases develop. This is primarily due to an overall decrease in atomic diffusion distances between individual phases and decreased activation energies for diffusion due to the increase in temperature. Additionally, lamellae thickness is further reduced and dispersoid spacing becomes more uniform during this stage. [2,38,39,41-45]

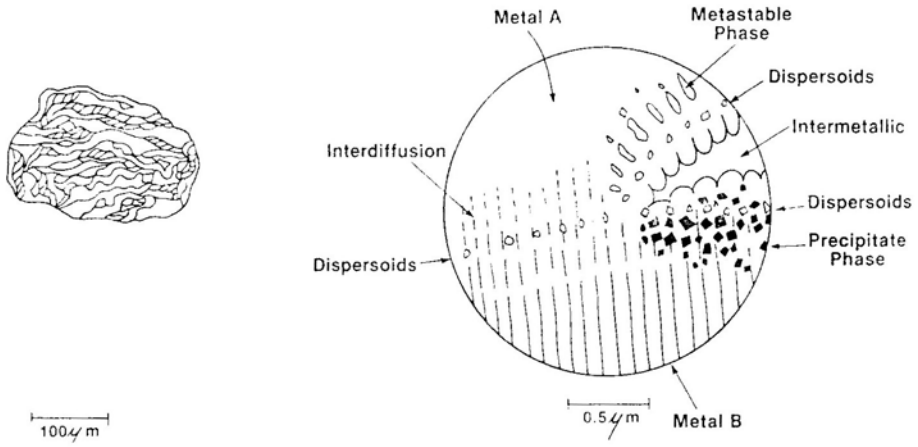

Figure 18: Intermediate stage of processing showing reduced lamellae thickness, solute dissolution, and formation of new phases. [2]

1.5.3.3 Final Stage

During this stage of processing (Figure 19), individual particle compositions are equal to the starting powder blend composition; the lamellae are no longer optically resolvable; and the dispersoid spacing is equal to the distance between weld interfaces. At this point, further processing would not improve the dispersoid distribution or serve to enhance the homogeneity of the composite microstructure.

In order to complete the MA process and obtain a useable bulk composite form, the powders are heated to a temperature greater than half the melting temperature of the composite powder and consolidated. This serves to further homogenize the microstructure and tends to evenly-distribute any impurities introduced during processing so as to reduce the effects of having large inclusions present in the bulk composite powder. Typical consolidation techniques include hot compaction followed by hot extrusion or hot isostatic pressing (see *1.5.4*).[2,38,39,41-45]

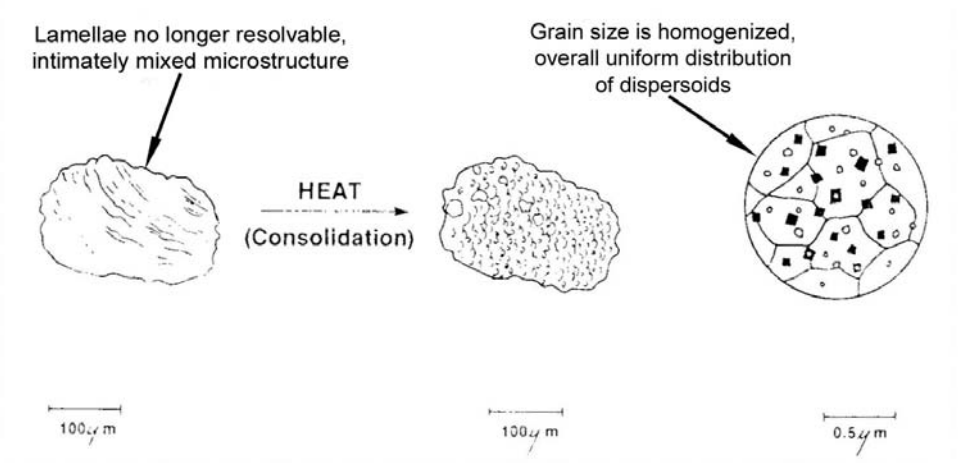

Figure 19: Final stage in processing and consolidation. [2]

1.5.4 Powder Consolidation

As was mentioned in the previous section, mechanically alloyed powders must ultimately be consolidated in some manner in order to use them in a given application. Simple pressing and sintering has not proven successful in the consolidation of many mechanically alloyed powder systems primarily due to the powder's inherent high hardness levels and the presence of harder-phase oxides within the powder microstructure. Typical consolidation techniques that have proven successful however, include hot compaction followed by hot extrusion and hot isostatic pressing (HIP). Once the powder is consolidated, it can then either be used directly or may be further processed to attain additional desirable properties such as texturing for increased directional strength. Figure 20, Figure 21, and Figure 22 show typical schematic representations of each of these consolidation processes.

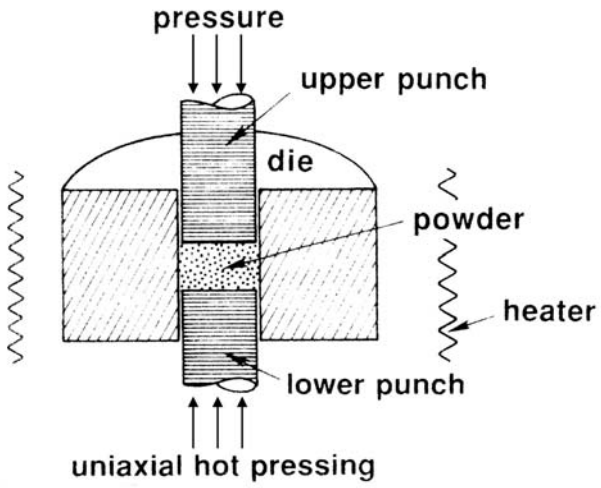

Figure 20: Cross-section of a typical hot compaction process. [3]

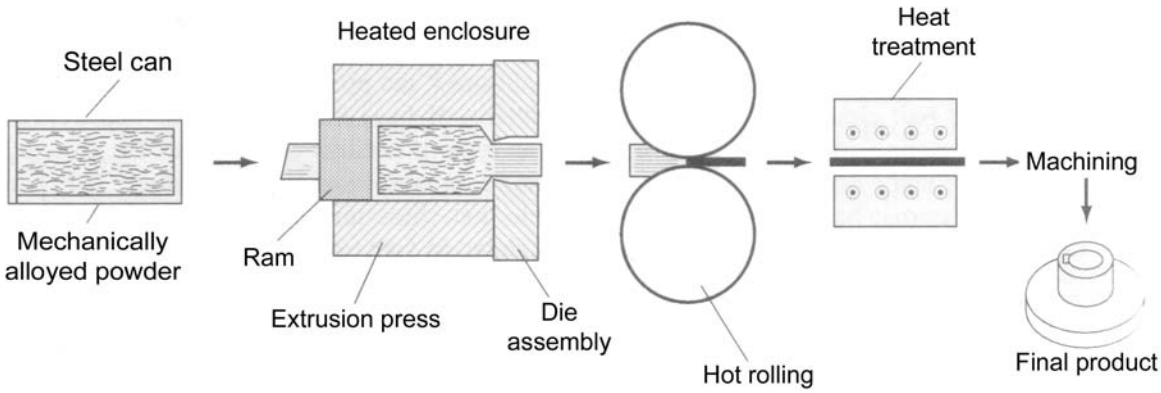

Figure 21: Schematic of a typical hot-extrusion processing path including additional alloy heat treatment. [40]39

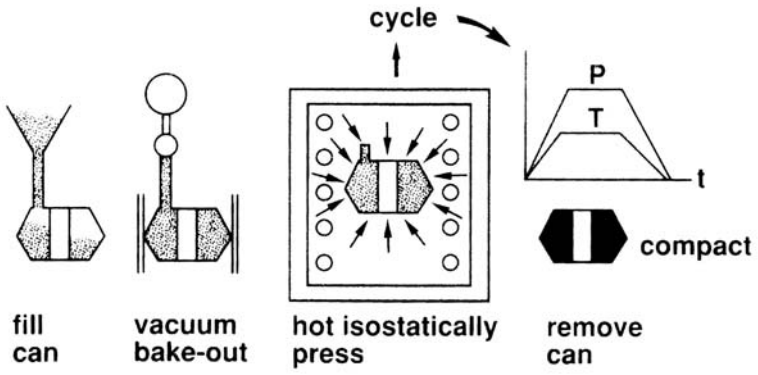

Figure 22: A schematic of a typical HIP operation and a common temperature (T) and pressure (P) schedule vs time.[3]

2. EXPERIMENTAL PROCEDURES

2.1 Development of Composite Model

2.1.1 General Outline

A unique and novel model was created to predict mechanical properties and mechanical damping capability for any discontinuously-reinforced metal matrix composite system. Specifically, the model is based on Eshelby's equivalent inclusion method and was created using Mathematica computer software. It can be broken up into five distinct main routines that, when combined, lead to a predicted amount of Joule heat that is produced for a given composite system for a given stressed state. Additionally, the model can predict composite stiffness over a range of reinforcement volume fractions and shapes. In that, the model is not able to predict the dynamic damping response for a given composite system and thus not able to predict a composite's loss modulus, but instead is best used as a relative ranking utility for the overall mechanical damping effectiveness for a host of composite systems.

Figure 23 shows a flowchart outlining the five main routines (numbered dark circles) of the model, and the basic user input that is required for one run. A brief overview of the thought processes involved with the development of these routines will now be given that serve to summarize specific details in a linear fashion. Detailed explanation of all aspects of the model will not be given here and the reader is directed to *Appendix C* for more specific modeling information.

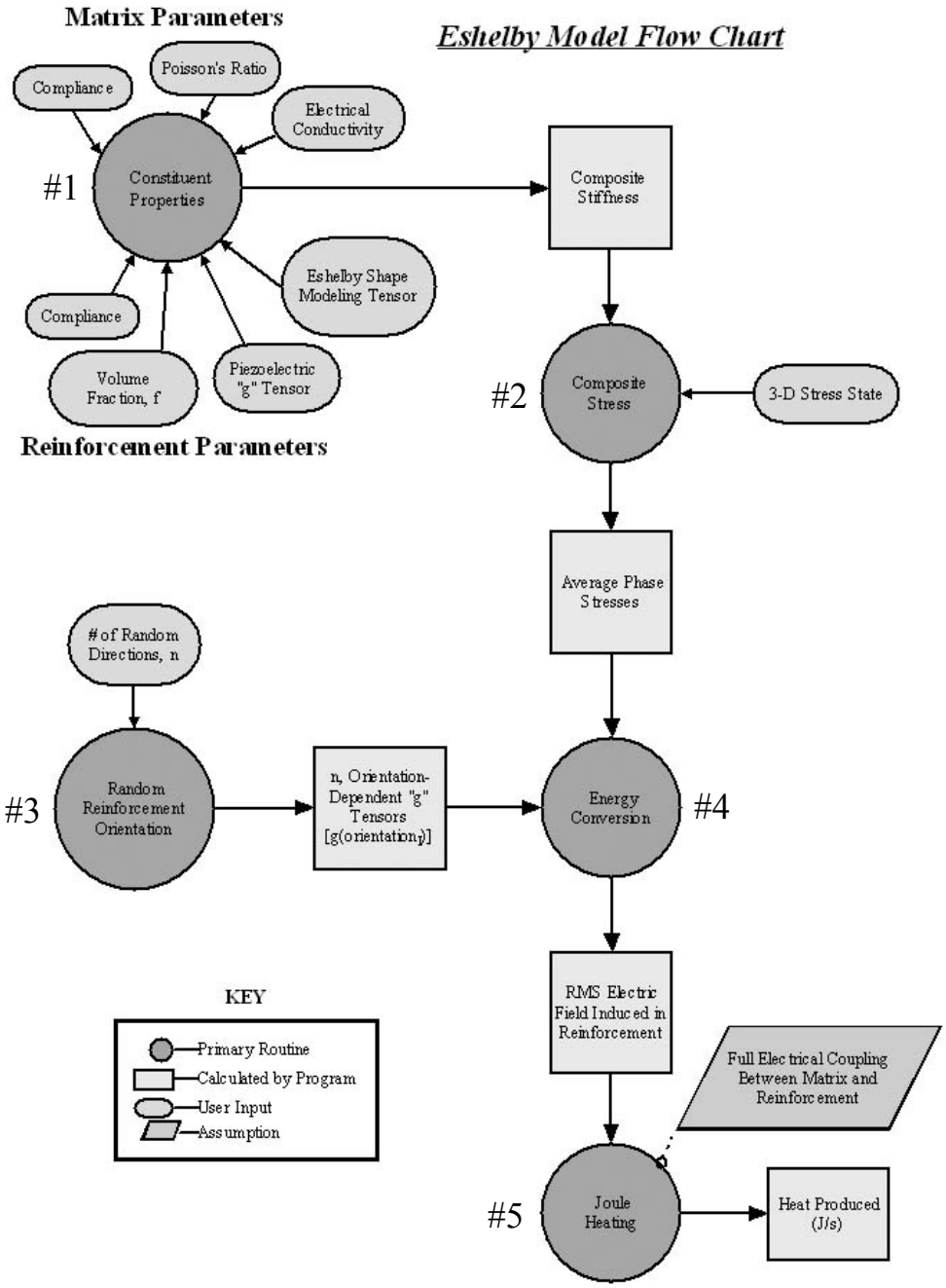

Figure 23: A flowchart outlining the five main routines (dark circles) of the Eshelby mathematical model and the basic input/output that is associated with one run.

2.1.2 Model Routine Specifics

Routine # 1: Constituent Properties

The Eshelby-based model is initialized by user definition of composite constituent properties. The composite matrix material is chosen and the appropriate compliance tensor is defined, along with the matrix Poisson's ratio, and electrical conductivity tensor. Similarly, the composite reinforcement material is chosen and the appropriate compliance tensor is defined, along with the volume fraction of reinforcement, piezoelectric "*g*" tensor in units of (*Vm/N*), and Eshelby shape tensor. It should be noted that the model is generic in form to allow the user to mold the modeling dynamics to their preference. It is therefore possible to experiment with single volume fractions, a range of volume fractions, and/or different Eshelby shape modeling tensors to analyze their impact on predicted composite modulus and damping capability.

Once all constituent properties have been input, the model puts the constituent compliance tensors and reinforcement piezoelectric "*g*" tensor into expanded form in order for mathematical operations to be performed on them. Eshelby's equivalent inclusion method is then used to arrive at a prediction for the overall composite compliance tensor(s), depending on whether a single volume fraction or a range of volume fractions is analyzed. Specifically, the equations used in predicting the composite compliance are

$$Q = f(S - I)[(C_M - C_I)S - C_M]^{-1}(C_I - C_M), \quad \textit{and} \quad S_C = [I + (S - I)^{-1}(I + Q)^{-1}Q]C_M{}^{-1} \qquad [35]$$

where C_M and C_I are the matrix and reinforcement stiffness, respectively, in units of (N/m^2), S is the Eshelby shape tensor, I is a 6x6 identity matrix, and S_C is the composite compliance tensor in units of (m^2/N). [37] At this point, reinforcement has been modeled as being mutually aligned for composite modulus calculations. This is not completely accurate; however this issue will be addressed in section 3.1.

Routine # 2: Composite Stress

As mentioned previously, this model does not predict the dynamic damping response of a composite material. Alternately, it predicts the composite mechanical response to a static, user-defined, three-dimensional stressed state. This particular stressed state can be thought of as an

average stress that the composite is subjected to per unit time. This mode of thinking effectively eliminates the difficulty in attempting to analyze a dynamic vibrational state. Therefore, the user defines a specific stress tensor to be analyzed in units of *GPa*. By utilizing the procedure outlined in Clyne and Withers [1], the stress is partitioned between the matrix and reinforcement phases according to the equations

$$\begin{aligned} \langle \sigma \rangle_M &= -fC_M(S-I)\varepsilon^T \\ \langle \sigma \rangle_I &= (1-f)C_M(S-I)\varepsilon^T \end{aligned} \qquad [36]$$

where $\langle \sigma \rangle_M$ and $\langle \sigma \rangle_I$ are the mean internal stress in the matrix and inclusion respectively, and ε^T is the transformation strain given by equation [24].

The average stress in the matrix and reinforcement is simply the addition of the applied stress and the mean internal stress of each constituent and is given by the following equations

$$\begin{aligned} \overline{\sigma}_M &= \sigma_A + \langle \sigma \rangle_M \\ &\textit{and} \\ \overline{\sigma}_I &= \sigma_A + \langle \sigma \rangle_I \end{aligned} \qquad [37]$$

where σ_A is the user-defined three-dimensional static stress (applied stress). The quantification of the average reinforcement stress is what makes the Eshelby technique so useful in the prediction of composite damping capability.

Routine # 3: Random Reinforcement Orientation

The third primary model routine accounts for the anisotropic nature of randomly-oriented discontinuous piezoelectric inclusions (e.g. $BaTiO_3$) within a metallic matrix. The reason that this is essential is that for any piezoelectric medium, the specific electromechanical response varies with direction within the unit cell. It is then necessary to appropriately account for this since the piezoelectric reinforcing particles are modeled as being randomly oriented.

Specifically, the piezoelectric "g" tensor is transformed into a user-defined number of different random sets or orientation axes. This is accomplished first through user input of the exact number of different orientations to analyze. For each number, a different random set of three mutually-perpendicular unit reference axes is calculated, representing an entirely unique orientation in which the reinforcement particles are modeled as being fully aligned. A transformation matrix is calculated using direction cosines between the three mutually-perpendicular unit reference axes for each randomly-chosen direction (see *Appendix C*). This

transformation matrix is then used to effectively transform the "*g*" tensor into the new set of reference axes.

At the end of routine # 3 there exists a new, transformed piezoelectric "*g*" tensor for each set of reference axes. Each new "*g*" tensor represents the global piezoelectric response as if all the particles were aligned in the new set of reference axes. Figure 24 shows the original reference axes used as a basis in this model for two common inclusion shapes and a new random orientation in which the piezoelectric "*g*" tensor is transformed into. The X, Y, Z reference axes correspond to the matrix orientation and the 1, 2, 3 axes correspond to the reinforcement orientation. The top two schematics in Figure 24 show the reinforcement and matrix orientations mutually aligned whereas the bottom two schematics shows the new reinforcement orientation after transformation into a new set of random reference axes. It is these new reference axes in which the piezoelectric "*g*" tensor is transformed into for each random orientation.

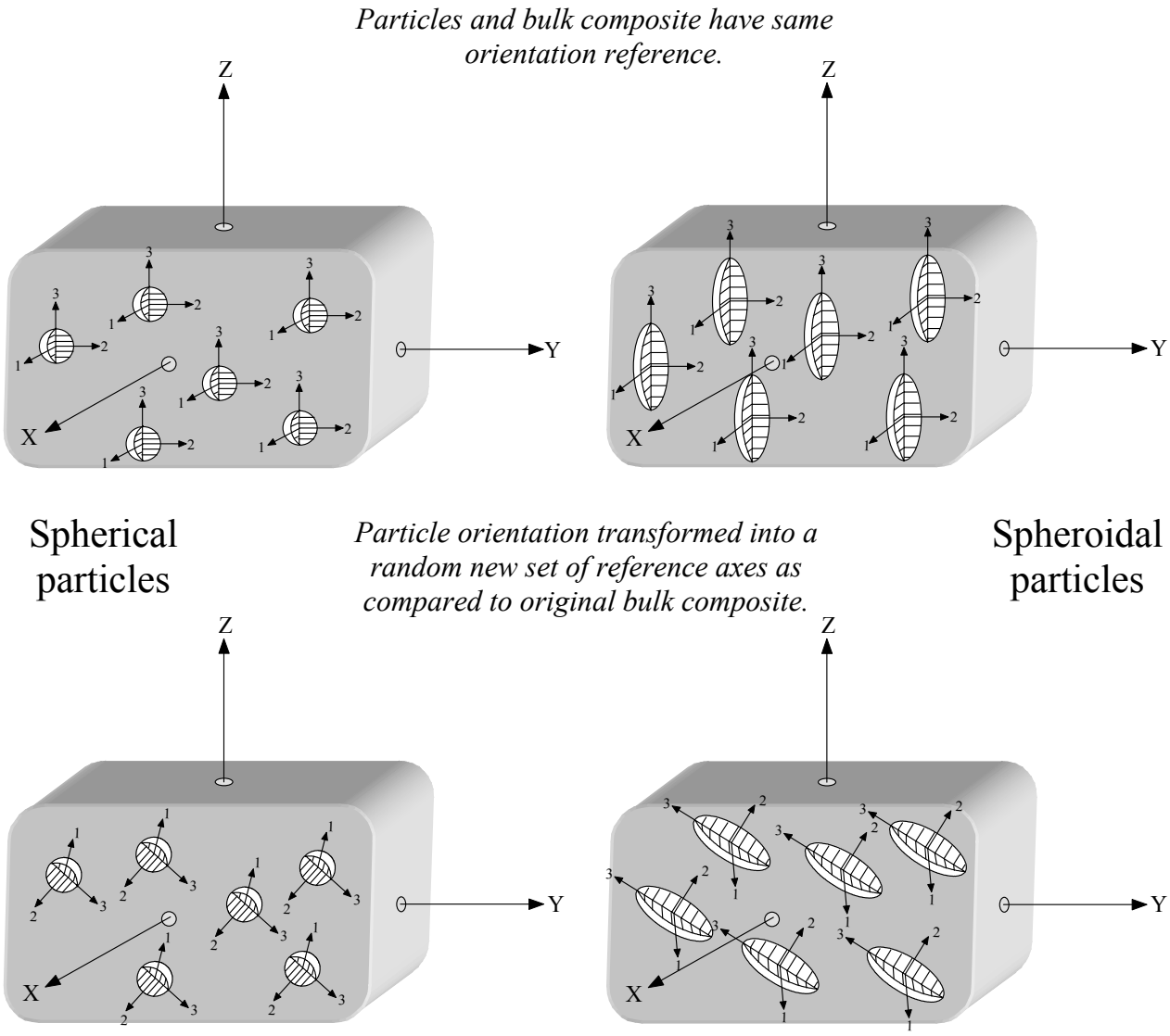

Figure 24: Orientation axes X,Y,Z correspond to matrix orientation, whereas axes 1,2,3 correspond to reinforcement orientation. Top two schematics show two different reinforcement shapes which are mutually aligned with the matrix orientation. Bottom two schematics show new reinforcement orientation after being transformed into a random set of reference axes.

Routine # 4: Energy Conversion

In this part of the model, each individual randomly-transformed piezoelectric "*g*" tensor is dotted into the average inclusion stress, resulting in the calculation of the average electric field induced in the reinforcement for each different reinforcement orientation. At this point, the model has calculated a user-defined set of different electric fields induced in the reinforcement representing the average field induced for each unique fully-aligned orientation of inclusions.

A root-mean-square calculation is then performed that effectively quantifies the overall average electric field induced in the randomly-oriented inclusions. The entire procedure is summarized as follows:

$$E(I) = g(I).\overline{\sigma}_I \qquad [38]$$

where *g(I)* is the inclusion orientation-dependent "*g*" tensor in units of (*Vm/N*), $\overline{\sigma}_I$ is the average stress in the reinforcement in units of (N/m^2) , *E(I)* is the orientation-dependent electric field induced in the reinforcement in units of (*V/m*), and

$$E_{rms} = \sqrt{\frac{\sum_{1}^{n} E(I)^2}{n}} \qquad [39]$$

where *n* is the number of different orientation references and E_{rms} is the root-mean-squared electric field, also in units of (*V/m*).

Routine # 5: Joule Heating Calculation

The final portion of the model consists of the calculation of the amount of Joule heat that is produced for a given composite volume based on the defined three-dimensional applied stress. First, the electrical conductivity tensor of the matrix material (σ_{cond}) is dotted into the root-mean-squared electric field to arrive at the current density (j_ρ) induced within the reinforcement-surrounding matrix. The current density is defined as

$$j_\rho = \sigma_{cond} \cdot E_{rms} \qquad [40]$$

where σ_{cond} has units of $(\Omega\ m)^{-1}$ and j_ρ has units of (A/m^2).

Before further progress is made by the model, the user must decide the volume of composite material to consider, with the easiest choice being 1 m^3. Choosing this volume simplifies things by allowing the volume fraction of reinforcement to represent the total volume occupied by the reinforcement in units of (m^3). Finally, by utilizing the current density, root-mean-squared electric field, and volume of reinforcement in a given overall composite volume, the model is able to calculate the predicted amount of Joule heat that results from the given situation. This is given by

$$Joule\,Heat = (j_\rho \cdot E_{rms}) \times v_r \qquad [41]$$

where v_r is the volume of the composite that is occupied by reinforcement and the amount of Joule Heat is in units of (*J/s*). This is the final calculation performed by the model and represents the final end-result of what it is intended to provide.

2.1.3 Use of Model and Assumptions Made

The model is set up in such a way as to require the user to manually input constituent properties, volume fractions of reinforcement to analyze, the three-dimensional stress state to apply to the composite, the number of different random orientations to analyze, and the total volume of composite material. The model does not prompt the user to input this information, thus detailed knowledge regarding the model layout is required in order to operate it successfully.

In all analyses and results presented here, the model was altered to automatically calculate the overall composite stiffness and the amount of Joule heat produced for volume fractions of reinforcement ranging from 0 – 1 in step increments of 0.025. Additionally, 25,000 different random orientations were chosen for the Random Reinforcement Orientation routine (#3). This number was chosen simply because it was found that any number greater than 25,000 didn't provide any significant increase in modeling resolution. The 3-D stress state was arbitrarily chosen and corresponded to an isostatic compression of 50 Pa which keeps all of the modeled composite systems in the elastic regime. Furthermore, the total composite volume chosen to analyze was $1cm^3$ resulting in the total volume occupied by the reinforcement to be equal to the volume fraction of reinforcement expressed in units of cm^3.

Specific assumptions made during modeling include the following: 1) All metallic matrices analyzed were polycrystalline and isotropic, 2) Reinforcement particles were fully aligned for the average phase stress and composite stiffness calculations, 3) Reinforcement particles are randomly oriented for the energy conversion calculation, 4) The reinforcement-matrix interfaces are strongly bonded, and 5) There is complete electrical coupling between the reinforcement and matrix and all electrical energy induced in the reinforcement is transferred as resistive heat into the matrix.

2.1.4 Modeled Composite Systems

The piezoelectric ceramic reinforcement phases chosen to be modeled include barium titanate ($BaTiO_3$), lead titanate ($PbTiO_3$), and zinc oxide (ZnO). These materials were chosen specifically because they were 1) either being investigated as a real dispersion phase at the time of modeling or 2) were planned to be investigated in future composite experiments. Each piezoelectric material was modeled as being dispersed in a host of metallic matrices that were chosen due to their traditional usefulness in structural applications, metal matrix composites, or simply because data were easily obtained for them. Table II shows the composite systems that were modeled during this analysis. Data for each constituent material along with the source is listed in *Appendix A*.

The piezoelectric ceramic materials were assumed to be crystalline and the metal matrices were assumed to be in the bulk polycrystalline form for all of the modeled systems. Additionally, each of the reinforcement phases were separately modeled as being dispersed in the shape of spheres, prolate spheroids, and penny-shaped discs, of which details follow.

Table II: Modeled Composite Systems

Reinforcement → Matrix ↓	*$BaTiO_3$*	*$PbTiO_3$*	*ZnO*
304 Stainless Steel			
Aluminum			
Brass			
Copper			
Mild Steel			
Lead			
Magnesium			
Nickel			
Ni – 20wt% Cr			
Tin			
Titanium			
Ti – 6Al – 4V			
Tungsten			

2.1.5 Reinforcement Shapes

Each reinforcement phase was modeled as being in the shape of spheres, prolate spheroids, and penny-shaped discs for each one of the metal matrices listed in Table II. These shapes were chosen because they are representative of what typical discontinuous reinforcement shapes often look like in real composite systems. Figure 25 shows each one of the different representative shapes along with assumed geometrical parameters used in the modeling for each case.

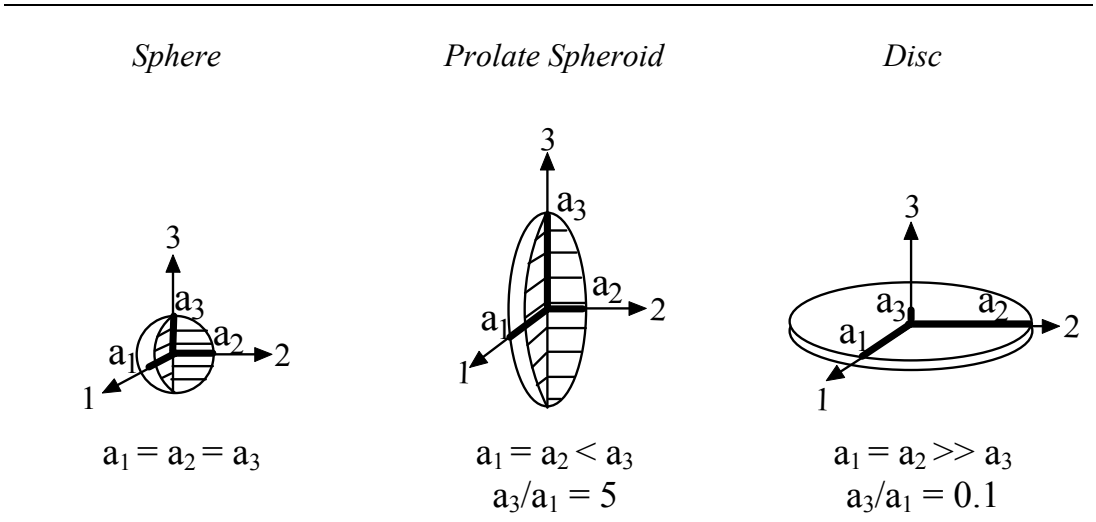

Figure 25: The three shapes chosen to represent the reinforcement shapes within the metal matrices during modeling. All three shapes were modeled for all three piezoelectric materials ($BaTiO_3$, $PbTiO_3$, ZnO) for each different metal matrix.

2.2 Production of Composite Using Mechanical Alloying (MA)

2.2.1 General Outline

A need was identified early on in this thesis project to be able to synthesize an actual piezoelectric ceramic-reinforced metal matrix composite in order to demonstrate either our ability or inability to create such a said material. Additionally, the actual composite material would serve as a means to obtain real vibration damping test specimens and test their damping effectiveness in order to show whether or not the electromechanical energy conversion theory hypothesized in this thesis holds true. A variety of synthesis routes were investigated as a

potential means in creating the composite material with the two most notable methods including Solvent-Assisted Reaction Synthesis (SARS) and Mechanical Alloying (MA).

Jennifer Frankin, a Master's student working on this same project, elected to perform the primary investigative work on utilizing SARS as a processing path and more information on this synthesis technique and her results can be found in her thesis submittal. Alternately, I elected to initiate primary work on utilizing mechanical alloying as a synthesis route and what follows is a summary of this work.

2.2.2 Composite Formulation

The composite system was chosen to be a *Ni-20wt%Cr–30v%$BaTiO_3$* material simply because several existing nickel-based superalloys are created by mechanical alloying. It was thought that by choosing a commercially mechanically alloyed system, difficulty in early experimental trials with unsuitable systems could be avoided. Barium titanate was chosen as the piezoelectric ceramic reinforcement due to its good piezoelectric response, availability, and low toxicity. The amount of reinforcement (30v%) was chosen simply because it was felt that this was a safe reinforcement loading, hopefully neither being too small to not notice any damping capability, or too large thus compromising composite strength.

The matrix in this composite formulation is based on a nickel oxide-dispersion-strengthened (ODS) superalloy created by the International Nickel Company (INCO, now owned by Special Metals) that contains 20wt% chromium balanced by nickel and strengthened by yitria oxide. This alloy is termed INCONEL MA 754 and its composition can be found in Table I of section 1.5.1. Figure 26 shows the Ni-Cr binary phase diagram. As can be seen, chromium can exist as a solid solution in nickel up until about 22wt%. It was hoped that this level of chromium solubility in nickel would be achieved during mechanical alloying and thus provide some level of solid-solution strengthening and corrosion resistance to the composite.

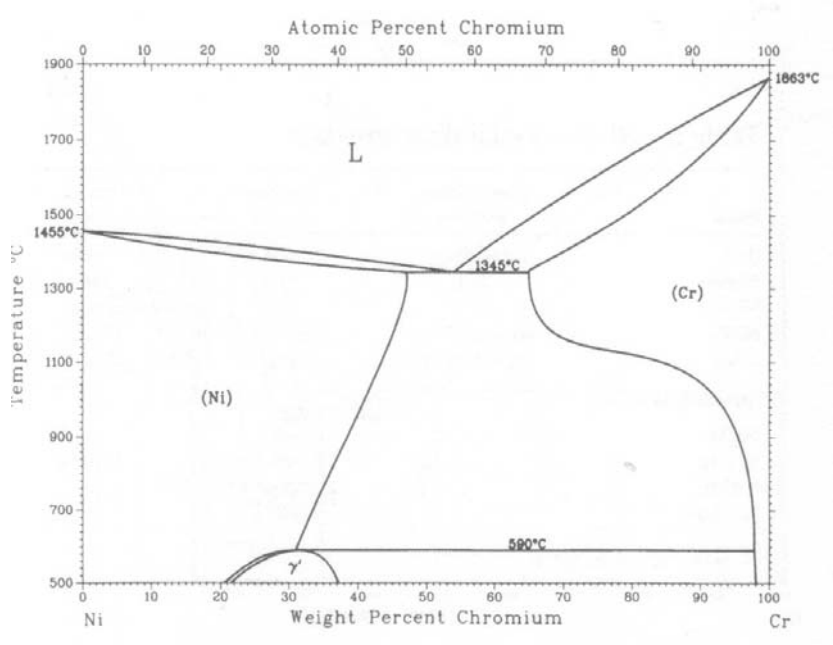

Figure 26: Ni-Cr binary phase diagram.

All of the composite constituent materials were obtained in powder form and were -325 mesh size (< 43μm). Elemental nickel and chromium powders were obtained from Atlantic Equipment Engineers (Bergenfield, NJ) and were 99.9% and 99.8% purity, respectively. Crystalline tetragonal barium titanate powder was obtained from Alfa-Aesar (Ward Hill, MA) and was 99% pure. The composition of the formulated composite is given in weight and volume percentages in Table III below.

Table III: Composition of the Mechanically Alloyed Composite.

Constituent	Weight %	Volume %
Ni	61.8	53.5
Cr	15.4	16.5
$BaTiO_3$	22.8	30.0

2.2.3 Mechanical Alloying

A SPEX™ 8000M mixer/mill (Figure 14) was utilized to mechanically alloy the composite. The SPEX vial and milling ball material was chosen to be 440C hardened steel in hopes of reducing contamination during milling due to its high hardness. Additionally, the diameter of the milling balls was 7/16" and a charge ratio of 4:1 was arbitrarily chosen.

All powder handling was done inside a LABCONCO™ Protector, Controlled Atmosphere Glove Box backfilled with argon gas. Constituent powders were weighed inside the glove box according to the stoichiometry given in Table III to give a resultant combined powder mass of 15 grams. The constituent powders and the ball charge were placed inside the SPEX vial (within the glove box) and sealed hand-tight. The loaded SPEX vial was then placed inside the mill and milled for 24 hours.

Upon completion of milling, separate composite powder samples were individually annealed in a LINDBERG™ tube furnace equipped with a piece of ≈ 2½" diameter INCONEL® 600 alloy purged with hydrogen gas for the times and temperatures given in Table IV. Annealing temperatures and times were arbitrarily chosen and temperatures were limited by the maximum use temperature of the INCONEL 600 tube (≈ 700°C). The designation of "*MA*" stands for "mechanically alloyed", "*HT*" stands for "heat treatment", and the numbers designate the annealing temperature and the time.

Table IV: Annealing Designations and Schedules for Several Post-Milled Composite Powder Samples.

Annealing Designation	**Temperature (°C)**	**Time (hours)**
MA-NOHT	-----	-----
MA-400HT-1	400	1
MA-400HT-5	400	5
MA-500HT-1	500	1
MA-500HT-5	500	5
MA-600HT-1	600	1
MA-600HT-5	600	5

2.2.4 Composite Characterization

2.2.4.1 X-Ray Diffraction

X-ray diffraction characterization was performed on the starting constituent powders, the as-milled powder, and the annealed powders using a Scintag XDS2000 powder diffractometer utilizing a copper target X-ray tube that produces a beam with principle wavelengths of Cu K-alpha1 (1.5405Å), Cu K-alpha2 (1.5443Å), and Cu K-beta (1.3922Å). The detector is able to exclude the Cu K-beta radiation from the diffraction patterns, but its resolution is somewhat poor

and recommended solely for use as a means to identify bulk phases present in a sample. Additionally, all diffraction scans utilized a 2-θ range of 15° - 70°. X-ray diffraction data was analyzed with the help of DRXWin 2.2 software, where mentioned.

2.2.4.2 Metallographic Preparation

The as-milled powder (*MA-NOHT*) and powder samples *MA-400HT-5*, *MA-500HT-5*, and *MA-600HT-5* were diluted in ground diallyl phthalate mount powder and hot-mounted using a LECO PR-22 pneumatic mounting press. Care was taken to ensure that individual composite powder particles were relatively isolated from one another during mounting to allow for a more coherent and strong bond between the sample and mounting powders to take place. Powder samples *MA-400HT-1*, *MA-500HT-1*, and *MA-600HT-1* were not mounted due to time constraints and the fact that nothing notably different was found between the samples annealed for 1 hour vs. 5 hours during X-ray diffraction analysis.

The mounted samples were rough polished with 240, 320, 400, and 600 grit grinding paper for 10 minutes each on an Ecomet 3 variable speed auto polisher. The samples were finished by auto polishing with a final finish polishing cloth and 0.04μm colloidal silica for 10 minutes. Finally, the mounted and polished powder samples were chemically etched in an attempt to make the dispersion of the $BaTiO_3$ particles within the Ni-Cr matrix more easily observable during analysis. Specifically, the etchant was composed of 70v% HCl and 30v% H_2O_2. This etchant composition was taken from Vander Voort [46] and is traditionally used for ODS superalloy materials including INCONEL MA-754. Each mounted powder specimen was immersed in this solution for approximately three seconds and rinsed with water followed by acetone.

2.2.4.3 Microscopy

Optical microscopy was performed on the as-polished mounted powder samples using an Olympus BH2-UMA microscope with a digital camera attached for image capture. The specimens were observed utilizing Nomarski differential interference contrast and polarized light. A field-emission scanning electron microscope (FE-SEM) was used to observe the as-polished and etched powder specimens at a much higher magnification than allowable by optical microscopy. Specifically, the FE-SEM unit was a LEO 1550 model with an IXRF Systems Iridium Microanalysis energy dispersive spectroscopy (EDS) unit attached to it that allowed for quantitative analysis of elemental constituents within the powder samples.

Lastly, transmission electron microscopy (TEM) was performed on the *MA-NOHT* powder sample using a Phillips EM420 unit equipped with a tungsten thermionic emitter. The powder specimen was prepared by diluting some of the powder in about 30mL of ethanol. A syringe was used to draw up some of this mixture and a small drop was applied to a carbon-coated copper TEM grid. The TEM specimen was observed using a double-tilt specimen holder.

3. EXPERIMENTAL RESULTS and DISCUSSION

3.1 Composite Modeling

Barium titanate ($BaTiO_3$), lead titanate ($PbTiO_3$), and zinc oxide (ZnO) piezoelectric ceramics were modeled as discontinuous reinforcement shaped as spheres, prolate spheroids, and penny-shaped discs within a host of metallic matrices (Table II). Both the composite elastic modulus and damping capability in the form of Joule heat were calculated for each specific composite system using the mathematical model previously outlined. Results from these analyses are now given.

3.1.1 Composite Elastic Modulus

Table V shows plots of composite elastic modulus as a function of volume fraction of reinforcement as predicted by the model for each material system. The plots are grouped according to the shape and type of piezoelectric reinforcement analyzed. It can be seen in all of the plots that the Eshelby equivalent inclusion-based model predicts that the composite elastic modulus originates at the pure matrix constituent's modulus value at zero volume fraction of reinforcement and approaches the pure reinforcement modulus at one volume fraction of reinforcement. This intuitively makes sense and is not mathematically surprising. It is also seen that composite elastic modulus increases with the addition of piezoelectric ceramics that have a higher stiffness than the pure matrix alone, whereas the opposite is true for matrices with higher stiffnesses than their respective reinforcement materials.

Table V: Plots of Composite Elastic Modulus vs. Volume Fraction of Reinforcement for three different piezoelectric ceramics dispersed in a host of metallic matrices.

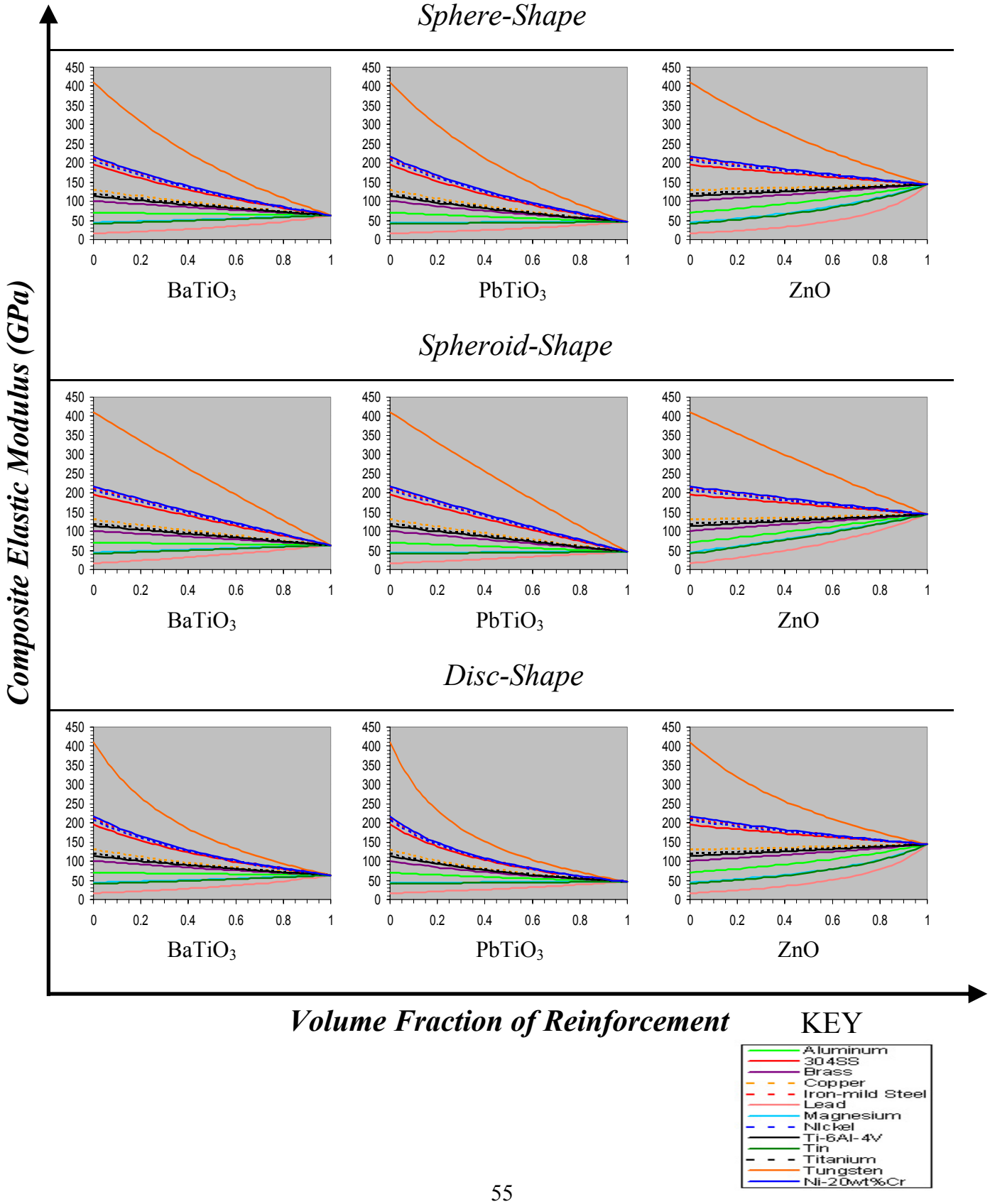

3.1.1.1 Trends in Behavior

Effect of Reinforcement Material

In general, crystalline ZnO (E = 144GPa) is the best reinforcement material that was analyzed because it has a higher elastic modulus than $BaTiO_3$ or $PbTiO_3$ (E = 64GPa and 47GPa respectively), thereby exhibiting the largest extent of elastic modulus enhancement on average for the metallic matrices that were examined. High-stiffness matrices such as tungsten, nickel, Ni-20wt%Cr, 304 stainless steel, and mild steel showed no elastic modulus enhancement with the addition of any of the reinforcement materials. The only matrices in which the elastic modulus was enhanced by the addition of either the $BaTiO_3$ or the $PbTiO_3$ reinforcement include lead, magnesium, and tin; while the addition of ZnO increased the elastic modulus of aluminum, brass, copper, lead, magnesium, Ti-6Al-4V, tin, and titanium.

Effect of Reinforcement Shape

In general, the reinforcement modeled as being in the shape of prolate spheroids provided the greatest level of modulus enhancement or lowest level of modulus weakening, depending on whether the metallic matrix elastic modulus was enhanced or lessened by the addition of the reinforcement. The spherical shape exhibited the next greatest level of elastic modulus enhancement while the disc shape exhibited the lowest. This behavior can be attributed to the fact that the reinforcement was modeled as being totally aligned, thus a greater increase in modulus was noticed for the shapes that were elongated in one direction (e.g. spheroids or discs). Additionally, the Eshelby shape modeling tensor takes into account the aspect ratio of reinforcement; therefore dimensional changes in reinforcement in one direction can have a pronounced effect on the composite elastic modulus. Consequently, elastic modulus trends presented here should be taken as true only for this specific set of modeling conditions (aspect ratio, reinforcement stiffness, etc).

For matrices in which the elastic modulus was much less than the reinforcement modulus (e.g. lead), the best reinforcing shape was the spheroid, followed by the disc and then the sphere. Table VI shows plots of composite modulus as a function of volume fraction of reinforcement for all three reinforcement shapes dispersed in brass, tin, tungsten, and lead matrices. Shape-elastic modulus trends can best be seen in these plots as opposed to the ones in Table V.

Table VI: Plots of Composite Elastic Modulus vs. Volume Fraction of Reinforcement for all three inclusion shapes dispersed in brass, tin, tungsten, and lead matrices.

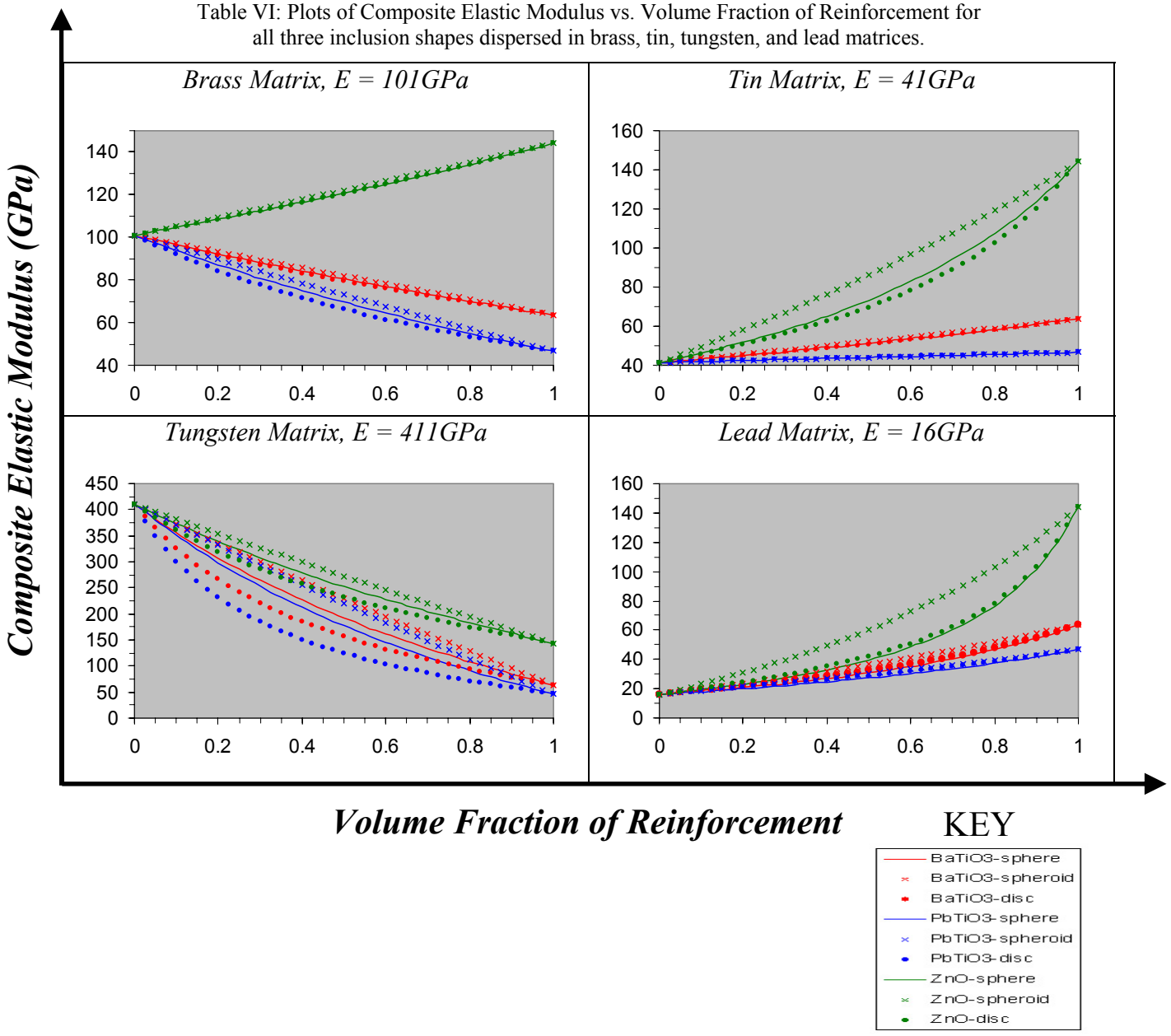

3.1.1.2 Comparison with Other Composite Predictions

It was determined that the Eshelby method of composite modeling predicts composite modulus values that agree with the famous Hashin-Shtrikman lower bound estimate. This can be seen in Figure 27 in which composite Young's modulus is plotted as a function of volume fraction of $BaTiO_3$ for a Ni-20wt%Cr matrix. Traditional composite mechanical property modeling techniques are plotted for comparison with the Eshelby method, including the Voight-

Reuss, Halpin-Tsai, and Hashin-Shtrikman bounds. It can be seen that the Eshelby method and the Hashin-Shrikman lower bound estimate fall in between all of the other composite modeling methods.

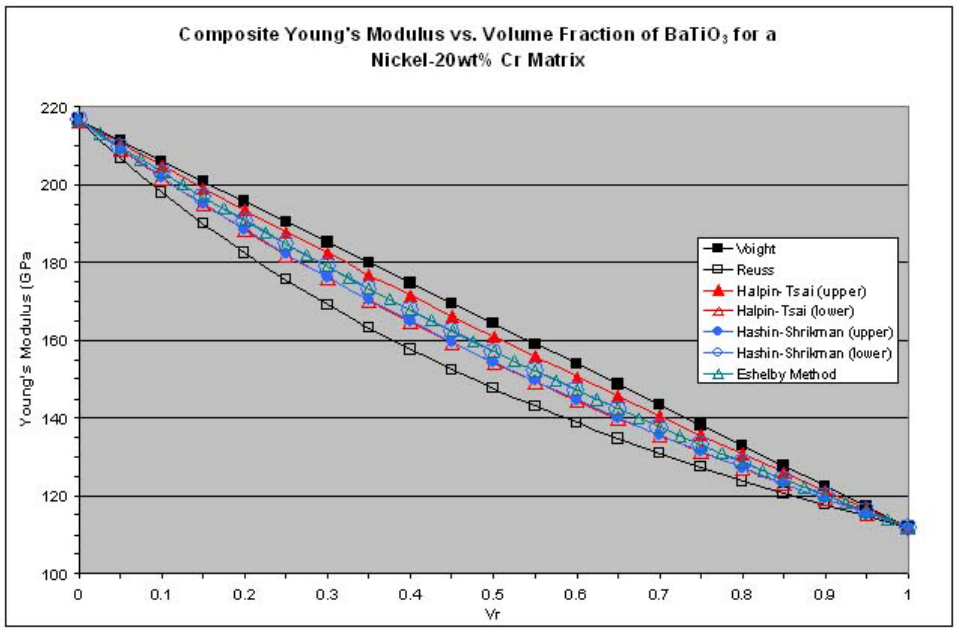

Figure 27: Plot of composite Young's modulus vs. volume fraction of ceramic $BaTiO_3$ for a Ni-20wt%Cr matrix based on four different composite modeling techniques. (spherical reinforcement)

3.1.2 Composite Damping Capability

Table VII shows composite damping capability in the form of Joule heat produced per second as a function of volume fraction of reinforcement for each modeled material system. Results are for an isostatic applied stress of 50Pa on $1cm^3$ of composite material. Plots are grouped according to the shape and type of piezoelectric reinforcement analyzed. Results are given for reinforcement volume fractions only up until 0.6 because it is thought that any more reinforcement addition past this relative amount would result in less effective damping and model predictions increasingly become less representative of the actual physical behavior. It is believed that as more and more reinforcement is added to the matrix, less of the matrix is able to encompass each reinforcing particle possibly resulting in electrical charge buildup and less resistive heating (damping).

Table VII: Plots of Composite Joule Heating vs. Volume Fraction of Reinforcement for three different piezoelectric ceramics dispersed in a host of metallic matrices.

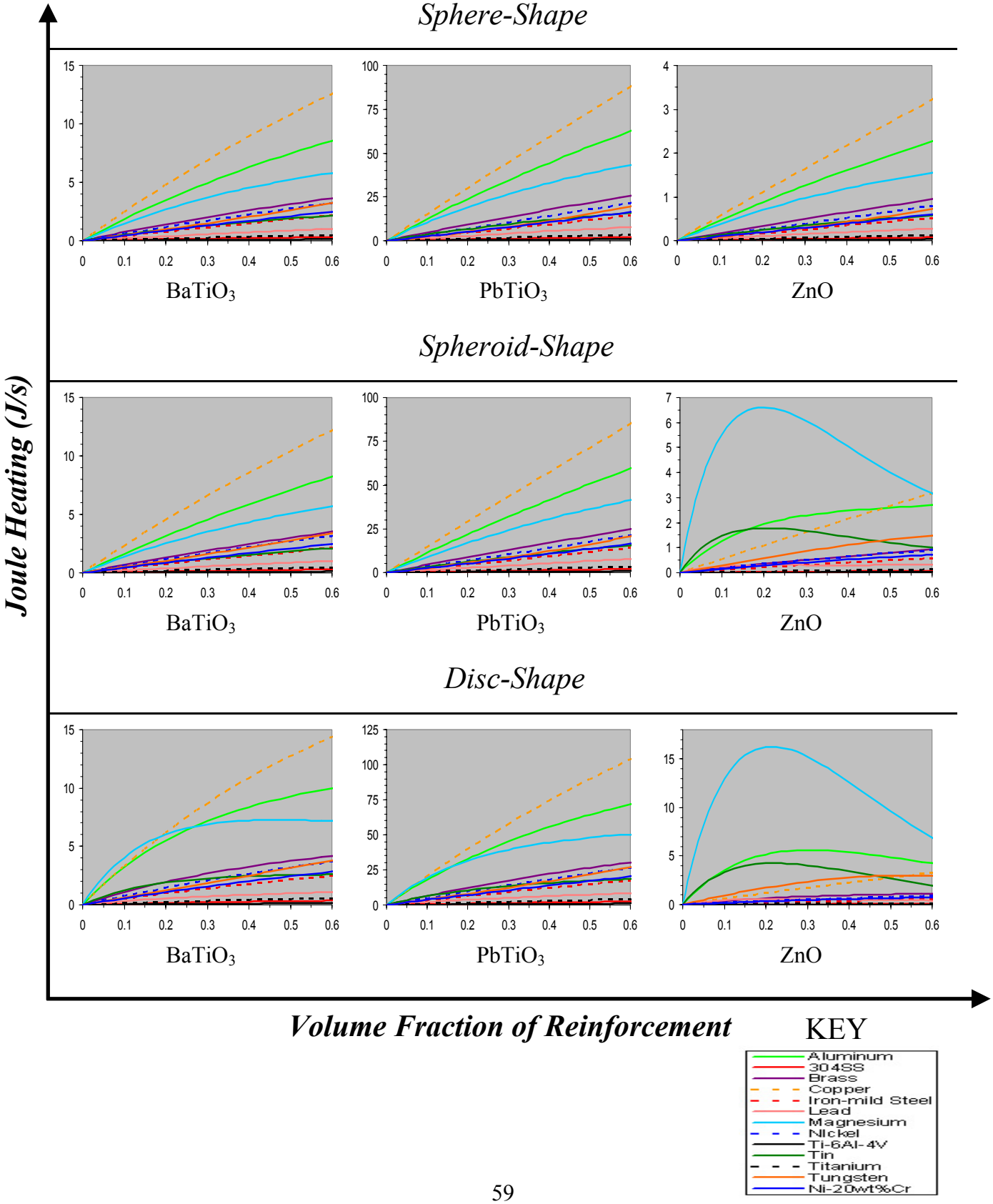

3.1.2.1 Trends in Behavior

Effect of Reinforcement Material

Lead titanate exhibits the largest damping capability for all of the metal matrices with barium titanate following in second, and zinc oxide in third. This can directly be attributed to the fact that $PbTiO_3$ has a larger piezoelectric "g" tensor (in principle directions) than both $BaTiO_3$ and ZnO. Similarly, $BaTiO_3$ has a larger "g" tensor than ZnO. When reinforcement is modeled as spheres, damping values for $PbTiO_3$ are about 7 times larger than $BaTiO_3$ values and about 25 times larger than ZnO values. This same general trend prevails for all of the $BaTiO_3$ modeled shapes; however damping behavior varies for ZnO when modeled as spheroids and/or discs.

Effect of Reinforcement Shape

In general, disc-shaped reinforcement predicts the highest levels of damping for a given piezoelectric reinforcement material. Sphere-shaped reinforcement predicts the next highest level of damping for all of the matrices and reinforcement materials except for that of ZnO. When reinforcement is modeled as spheroids, a higher damping response is predicted for ZnO than if it were modeled as spheres. This is due to the addition of the stiff ZnO (E=144GPa) phase, coupled with the fact that elongated spheroid particles tend to increase load transfer between the matrix and reinforcement thus increasing the amount of load taken on by the piezoelectric particles. Increased load on the piezoelectric particles directly translates into more of an induced electric field throughout the reinforcement, and thus more resistive Joule heating is predicted.

Interesting behavior is noticed for magnesium, aluminum, and tin matrices when reinforcement is modeled as spheroidal and disc-shaped ZnO particles. A peak in damping capability occurs for these matrices that can be correlated with a maximum in load transfer from the matrix to the elongated reinforcement. These matrices are significantly strengthened by the addition of the ZnO since the Mg, Al, and Sn have elastic moduli of 44.7, 70.3, and 41.4GPa, respectively. All of these matrices additionally have high electrical conductivities (*Appendix A*). Their high conductivity coupled with the increase in load transfer due to the addition of the stiff, elongated ZnO particles results in the increase in damping capability seen in Table VII. However, as volume fraction of reinforcement increases, there are more and more individual inclusions available to take on some of the applied stress, therefore resulting in a decrease in

overall average inclusion stress. The peaks in damping occur when this average inclusion stress decrement takes over the benefit of having an increased total volume of reinforcement.

3.1.3 Discussion on Modeling

Warning should be stated in regards to the accuracy of the model predictions and to what faith should be placed in their end-values. The composite model was constructed by over-simplifying real behavior and making several assumptions that were known to be somewhat inaccurate. Namely, all reinforcement shapes were modeled as being mutually aligned with one another during composite elastic modulus calculations. This was done in part because trial experiments showed that random reinforcement orientation played a small role in the overall composite stiffness predictions when compared to other, larger factors, such as reinforcement stiffness and matrix Poisson's ratio. This assumption was also made to save on model computing time. The addition of a random orientation calculation for both the inclusion stiffness tensor and the Eshelby shape tensor resulted in an increase in model run-time from about 15 minutes per run to about 2.5 hours per run. Trial model runs in which both of these random orientation routines were used resulted in a minutely-changed predicted composite elastic modulus. Additionally, composite damping predictions tended to the spherical-shaped reinforcement predictions. This makes sense in that as random orientation resolution is increased during modeling, a non-spherical shape (such as a disc) is rotated and re-oriented in so many different directions that an anisotropic tensorial value approaches the isotropic one. The situation can be compared to a penny spinning on a table top. At any given instance in time the penny is still a penny and is still disk-shaped, but to our time-averaging eyes the penny appears to be a spinning sphere.

Reinforcing peiezoelectric particles will more than likely be randomly oriented within the composites that we synthesize, simply due to the nature of the synthesis processes. Mechanical alloying leads to a discontinuous dispersion of polyhedral-shaped piezoelectric ceramic particles (see section 3.2) that can be approximated as spheres. Therefore, using sphere-shaped reinforcement is the ideal choice when modeling the damping capabilities of potential mechanically alloyed material systems.

Reaction synthesis can result in many uniquely-shaped particles, with the specific morphology and orientation of the reinforcement dependent upon the chemistry and

thermodynamics of the composite system and associated reactions. Any number of shapes and aspect ratios can be imagined including, plate-like morphologies, discs, fibers, cuboids, and spheres. Additionally, these reinforcement shapes may or may not have a preferred orientation, depending on the specific material system. Therefore, the choice of reinforcement shape and orientation used during modeling should be made on a case-by-case basis.

Other assumptions that were made in order to ease construction of the model include the assumption that the reinforcement/matrix interfaces were strongly bonded and that there was total electromechanical coupling between the piezoelectric particles and the matrix. In any real composite there will inevitably be some degree of poor bonding at the particle/matrix interface, possibly resulting in slippage. In some cases this is actually beneficial to mechanical damping, but in the case of examining the coupling extent of electrical fields to a conducting matrix, weakly-bonded interfaces may actually be harmful to composite damping capability. Likewise, there will never be total energy transfer of electrical fields to a conducting matrix in a real composite. There will always be some degree of field build-up around the particles that may or may not interfere with the particles' ability to transfer further mechanical energy into an electrical field. Finally, the Joule heat that is produced from the mechanical/electrical/thermal energy conversion mechanism may not be able to be carried away fast enough due to issues associated with internal metallic heat conduction. This may cause further electrical field build-up, resulting in a less-effective damping system.

In any regard, the model should be used as a relative prediction tool to qualitatively rank the damping effectiveness of a family of different material systems. In no way should the model be used as a definitive quantitative tool for a material's absolute damping capability. Accordingly, the model should only be used for stress states that are in the composite elastic regime. Electromechanical theory and assumptions break down once composite mechanical behavior becomes plastic.

3.1.4 Summary of Modeling Results

The model used to predict composite stiffness and mechanical damping capability proved quite useful in ranking the overall effectiveness that different reinforcement materials, shapes, and aspect ratios had on metal matrix composite mechanical behavior. The composite model predicts that matrices reinforced with $PbTiO_3$ should exhibit the largest levels of mechanical

damping as compared to $BaTiO_3$ and ZnO reinforcement. Barium titanate is the next best piezoelectric material for damping purposes, followed by zinc oxide. This trend in piezoelectric material damping behavior can be correlated with the magnitude of each one's piezoelectric "g" tensor with larger tensors translating into a higher damping capability. Additionally, low-stiffness, high-conductivity metal matrices such as copper, aluminum, and magnesium tend to facilitate damping as defined by the model more so than stiffer and more resistive matrices. This is due to increased load transfer from the compliant metal matrix to the stiff piezoelectric inclusions, in turn producing a larger magnitude of electric field and thus more resistive heat produced (increased damping). Lastly, disc-shaped inclusions resulted in larger levels of damping overall with the sphere-shaped inclusions coming in second and the spheroids in third. This may be attributed to the larger aspect ratio for the discs(10) as compared to the smaller spheroid aspect ratio(5) and sphere(1). (see section 2.1) Additionally, there may be more of a pronounced effect of the Eshelby shape modeling tensor on the predicted load transfer for disc-shaped reinforcement as opposed to spheroid or sphere-shaped reinforcement, even when all other factors such as aspect ratio, volume, or surface area are common for each shape.

3.2 Mechanical Alloying

A *Ni-20wt%Cr-30v%$BaTiO_3$* composite was created by mechanically alloying a mixture of nickel, chromium, and barium titanate powders in a SPEX mixer/mill for 24 hours. Individual powder samples were then annealed at 400°C, 500°C, and 600°C for 1 hour and for 5 hours separately in a hydrogen tube furnace. Characterization of the powders was carried out using X-ray diffraction, optical microscopy, scanning electron microscopy (SEM) coupled with energy dispersive spectroscopy (EDS), and transmission electron microscopy (TEM). Table VIII shows a summary of the different powder samples and the characterization techniques that were employed for each one.

Table VIII: Specific Methods of Characterization Performed on Each Powder Sample

Powder Sample	X-ray Diffraction	Optical Microscopy	SEM and EDS	TEM
MA-NOHT	X	X	X	X
MA-400HT-1	X			
MA-400HT-5	X	X	X	
MA-500HT-1	X			
MA-500HT-5	X	X	X	
MA-600HT-1	X			
MA-600HT-5	X	X	X	

3.2.1 Analysis of Constituent Powders

All starting composite constituent powders were -325 mesh size (<43μm) and detailed information as to the processes used to synthesize them unfortunately was not available at the time of writing. Scanning electron microscopy was used to obtain a general view of the morphology of the starting powders used in the mechanical alloying experiment. Detailed particle size analysis was not performed due to the initial powder size-independent nature of the mechanical alloying process. Figure 28 is an SEM micrograph exhibiting the clustered polyhedral morphology of the nickel powder. Agglomerated particles appear to be on the same size order.

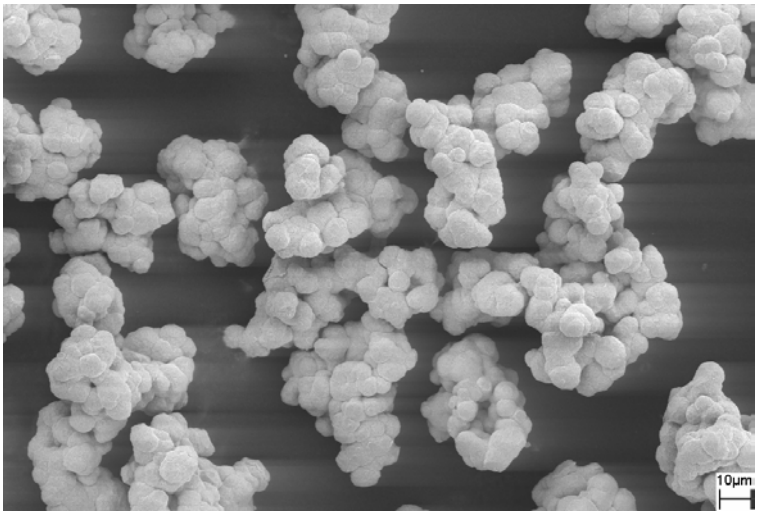

Figure 28: SEM micrograph showing the nickel powder used in mechanical alloying.

Figure 29 is an SEM micrograph showing the chromium powder used in the mechanical alloying experiment. The particles are more jagged and elongated than the nickel powders and particle diameter fluctuates between about 50μm to around 1 or 2μm.

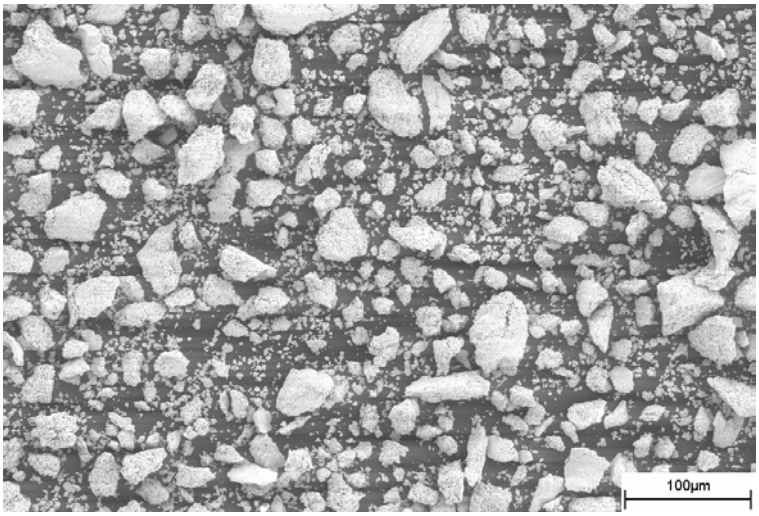

Figure 29: SEM micrograph showing the chromium powder used in mechanical alloying.

Figure 30 shows the barium titanate powder used in mechanical alloying. The clustered particles appear to be agglomerated, smooth polyhedrons that have individual diameters between about 1-2µm and the submicron range.

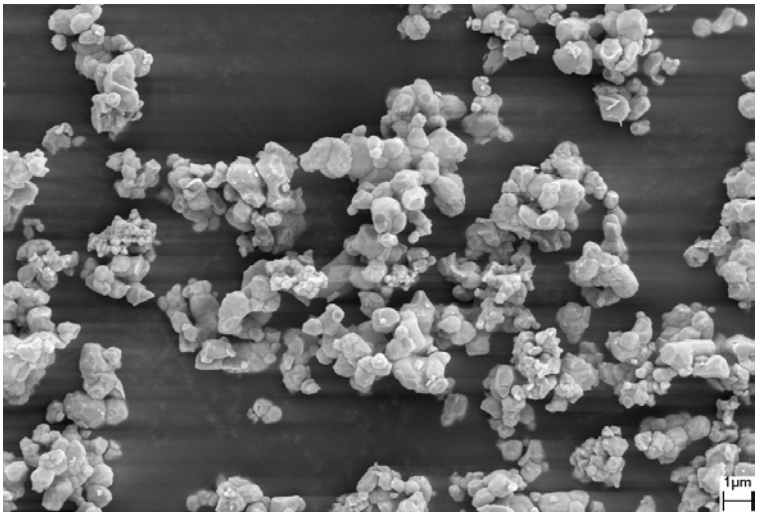

Figure 30: SEM micrograph showing the barium titanate powder used in mechanical alloying.

3.2.2 Description of the Mechanical Alloying Process

Nothing out of the ordinary occurred during the MA process except that heat was generated during milling. After the 24 hour milling time the SPEX vial was extremely hot and thermal-protective gloves had to be worn in order to handle the container. It is thought that the temperature of the container was probably above about 100°C, although no accurate temperature

measurement was conducted. It is not uncommon during mechanical alloying (or milling in general) for excessive heat to be generated, simply due to the internal friction within the container from the motion of the milling balls and the container itself. It was first thought that possibly an exothermic chemical reaction had occurred during milling, thus releasing a large amount of heat into the container; however later X-ray diffraction measurements proved this was not the case.

3.2.3 Analysis of the Mechanically Alloyed Composite

3.2.3.1 X-ray Diffraction

X-ray diffraction (XRD) characterization was performed on the pure starting constituent powders, the as-milled composite powder, and on all of the annealed powders. A 2-θ range between 15° and 70° was used in all measurements. Table IX is a listing of the predicted diffraction peaks for the starting constituent powders. Both the tetragonal and cubic form of $BaTiO_3$ is given as well for comparison purposes. It should be mentioned that it was a primary goal to retain the tetragonal form of $BaTiO_3$ during mechanical alloying since it is this form which exhibits the greatest level of piezoelectricity. The supplier of the pure $BaTiO_3$ powder (Alfa Aesar) claimed that it was in the tetragonal form and XRD results later proved that it indeed was.

Table IX: Predicted Diffraction Peaks and Relative Intensities for the MA Starting Constituents.
(Data adapted from the JCPDS powder diffraction database)

			Predicted Diffraction Data		
Constituent	**Space Group**	**Crystal System**	**2-θ**	**Intensity**	**h k l**
Ni	Fm$\bar{3}$m	FCC	44.497	999	111
			51.851	420	200
Cr	Im$\bar{3}$m	BCC	44.371	999	110
			64.554	112	200
$BaTiO_3$	P4mm	Tetragonal (perovskite)	22.019	107	001
			22.237	201	100
			31.495	999	101
			31.651	597	110
			38.893	330	111
			44.908	150	002
			45.371	291	200
			50.664	41	102
			50.981	43	201
			51.087	54	210
			55.979	149	112
			56.275	291	211
			65.748	136	202
			66.107	71	220
$BaTiO_3$	Pm$\bar{3}$m	Cubic (perovskite)	22.139	204	100
			31.51	999	110
			38.847	229	111
			45.163	300	200
			50.849	79	210
			56.107	297	211
			65.784	139	220

Figure 31 shows XRD results from the starting constituent powders. The nickel and chromium powders produced peaks as would be expected from Table IX and the barium titanate powder produced peaks corresponding to the tetragonal form. Individual peaks should occur for the (101) and (110) planes (and others) for tetragonal $BaTiO_3$, however 2-θ peak values were too close together to be resolved by the diffractometer.

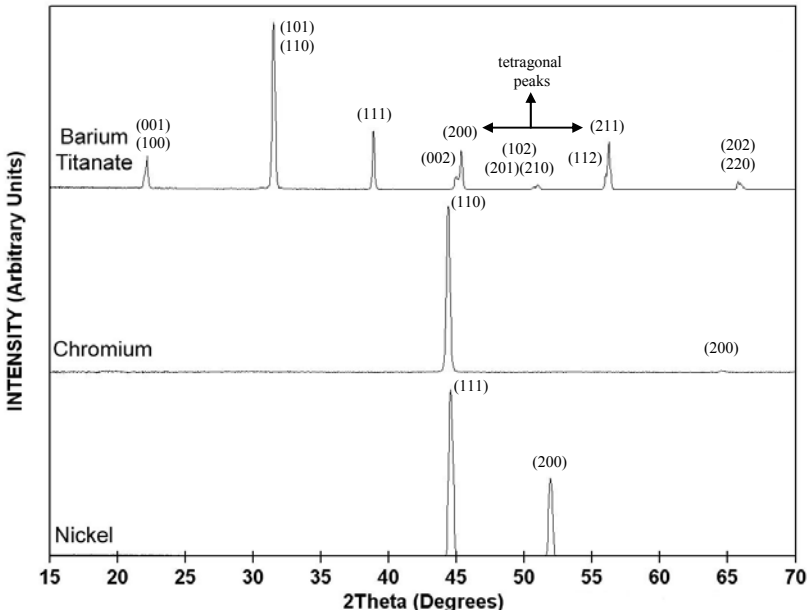

Figure 31: XRD results for the pure starting constituent powders used for mechanical alloying.

Figure 32 shows XRD results for the as-milled powder sample, *MA-NOHT*, compared to the starting constituents. The as-milled powder sample appears to be composed of a mixture of the starting constituents, although it is unclear which form of $BaTiO_3$ is present. The temperature of the powders and container increased as milling progressed due to friction. If the system temperature surpassed the Curie temperature for $BaTiO_3$ (≈130°C), coupled with the fact that the powders were under highly-strained states during alloying, then it's possible that the $BaTiO_3$ powder was converted from the tetragonal into the cubic form.

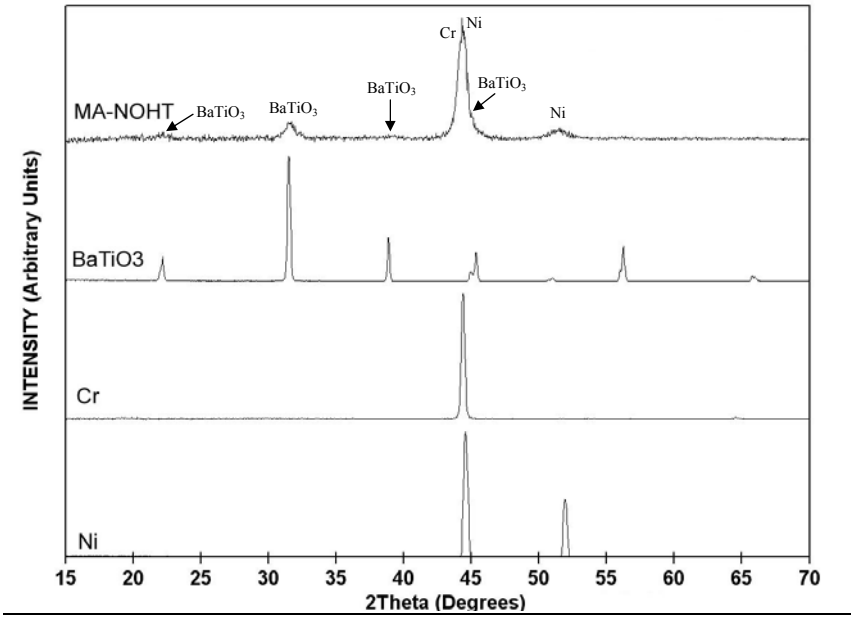

Figure 32: XRD results for the as-milled powder sample, *MA-NOHT*, as compared to results for the starting constituent powders. The as-milled sample appears to be a mixture of the starting constituents.

Determining whether $BaTiO_3$ is cubic or tetragonal is not easily resolvable by XRD of a composite powder mixture. This is because the diffraction peaks of both the cubic and tetragonal structures of $BaTiO_3$ are so similar and that the tetragonal crystal structure is just slightly elongated in the c-direction. Also, the highly-energetic nature of the mechanical alloying process leads to highly-strained powders and refined particle sizes. This causes diffraction peaks to broaden and/or shift off of position further implicating the difficulty in determining the crystal structure of $BaTiO_3$. It's possible that characteristic peaks of tetragonal $BaTiO_3$ are present in Figure 32, but that the peak broadening effect masks them.

Figure 33 is a diffraction peak comparison showing the $Ni_{(111)}$, $Cr_{(110)}$, and $BaTiO_3$ (002) (200) peaks for the powders in Figure 32 at a much higher magnification. It can more easily be seen that the $Ni_{(111)}$-$Cr_{(110)}$ diffraction peaks for the as-milled powder are slightly shifted to lower 2-θ values and are much broader than the constituent powder peaks. This can be attributed to strain and smaller particle sizes induced during milling. The strain is probably a mixture of mechanical strain from milling ball-container entrapment of powders and lattice strain due to the solid substitution of chromium in the FCC nickel lattice. The $BaTiO_3$ peaks in the as-milled sample are dominated by the $Ni_{(111)}$ peak so their presence is not easily noticeable.

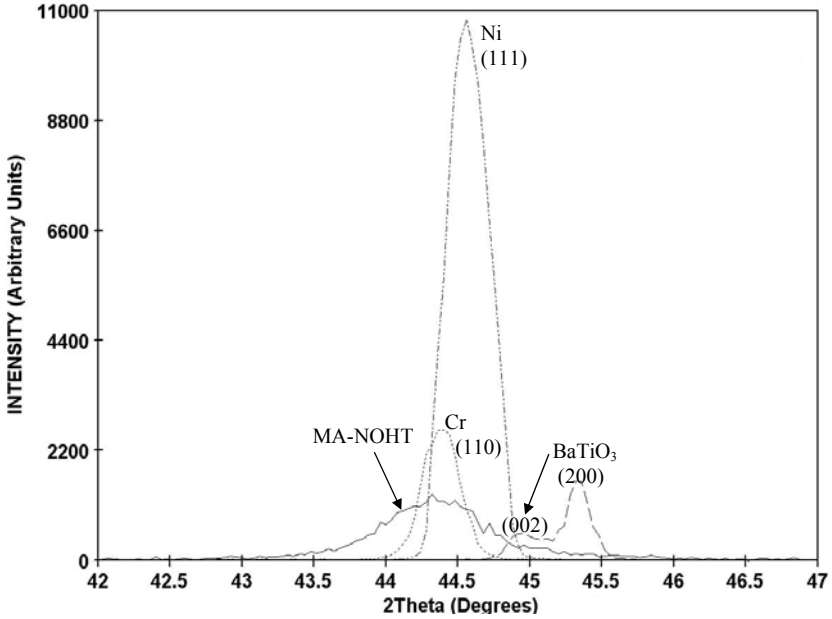

Figure 33: A diffraction peak comparison between the pure constituents and as-milled powders.

Starting constituent volume-weighted fractional XRD data was added together using DRXWin 2.2 XRD analysis software to arrive at a predicted diffraction pattern for the mechanically alloyed *Ni-20wt%Cr-30v%$BaTiO_3$* composite powder. This predicted pattern is shown in Figure 34 along with the experimental XRD results for the as-milled powder and for all of the annealed powders. The powder XRD results exhibit diffraction peaks that match up with what is predicted by the volume-weighted diffraction pattern, although the predicted pattern's peaks are much sharper. Powder sample peak broadening can be attributed to induced strain (lattice and mechanical) and decreased particle size during milling. Lastly, all of the powder samples appear to be mixtures of the starting constituents with the powders that were annealed at higher temperatures showing some level of peak sharpening indicating strain recovery.

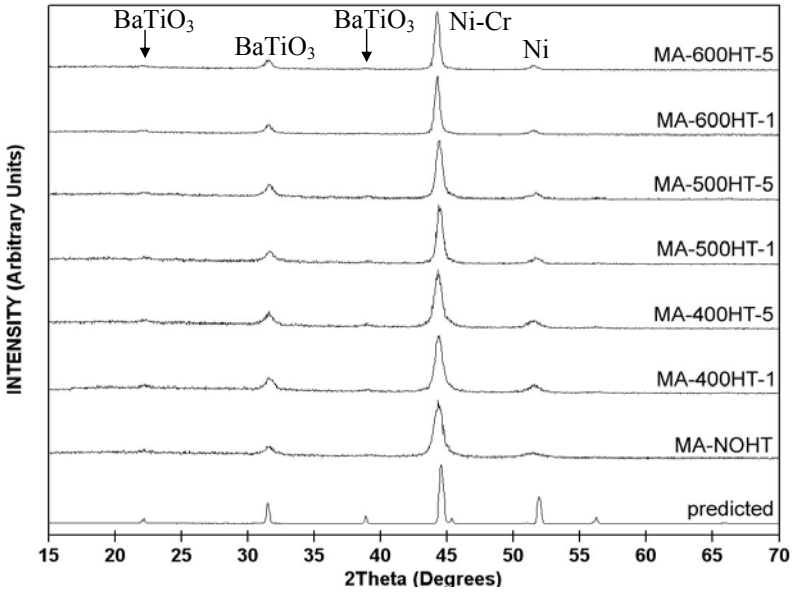

Figure 34: Diffraction patterns for a predicted volume-weighted mixture of the starting constituents as well as results for the as-milled powder and for all of the annealed powders.

Specific peak broadening and shifting can more easily be seen by magnifying the $Ni_{(111)}$-$Cr_{(110)}$ peak in Figure 34. Figure 35 (a) shows the predicted $Ni_{(111)}$-$Cr_{(110)}$ diffraction peak as compared to the peaks for the as-milled powder and for the powders annealed at 400°, 500°, and 600°C for one hour. Figure 35 (b) is the same as (a) except that the powders were annealed at 400°C, 500°C, and 600°C for five hours each.

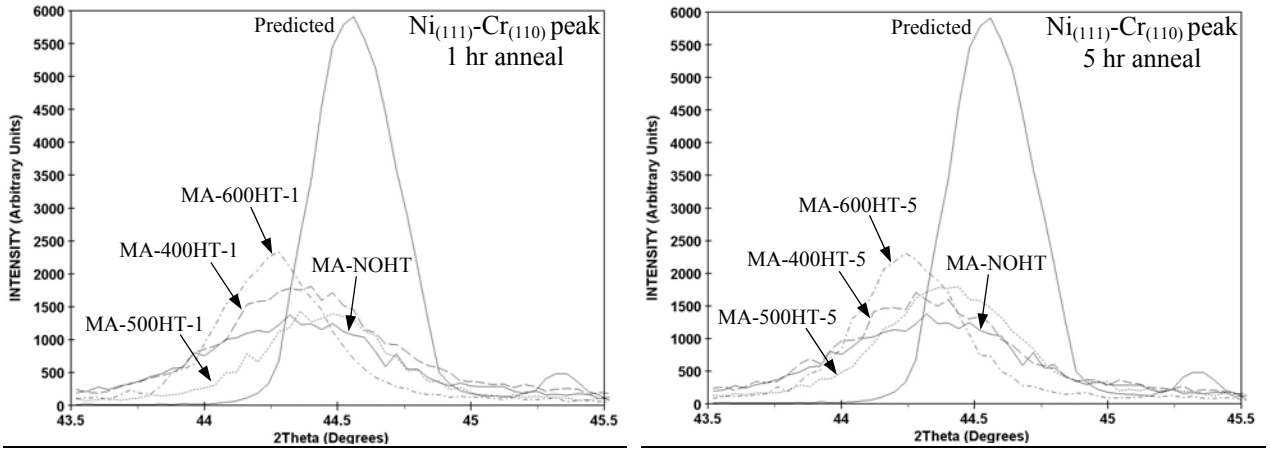

(a) (b)

Figure 35: Magnification of the $Ni_{(111)}$-$Cr_{(110)}$ diffraction peaks for the predicted pattern, the as-milled powder, and the powders annealed for (a) one hour and (b) five hours.

It can be seen in Figure 35 (a) that the sample annealed at 400°C actually has a larger peak intensity than the sample annealed at 500°C. This is counter-intuitive since a higher annealing temperature should result in more strain recovery and lead to sharper diffraction peaks. The diffraction peak intensity is comparable for the samples annealed at 400°C and 500°C for five hours shown in Figure 35 (b). Peaks for the 600°C annealed samples are sharper and more intense than the other annealed samples' peaks in both (a) and (b). This means that more recovery occurs in the powders at this higher annealing temperature, however it is unclear as to whether or not a higher annealing temperature and/or time would result in even more recovery. A more detailed heat treatment regimen should be employed to try to determine the proper annealing cycle to fully recover the strained composite powder crystallites.

It's worth mentioning that some peak shifting is noticeable in both Figure 35 (a) and (b) owing to induced particle strain during milling, decreased particle size, and crystal lattice distortion of the solid substitution of Cr in Ni. It is unclear as to what relative amounts of peak broadening and shifting can be attributed to each case, mostly due to the fact that the diffractometer used to take the powder diffraction measurements was not very precise, owing to small fluctuations in the 2-θ scale from sample to sample and poor resolution. Thus, intricate lattice cell analysis and peak refinement that is required to determine the relative effects of each peak broadening/shifting mechanism was not performed.

Average crystallite size was calculated for all of the powders assuming that particle size was the main contributing factor to peak breadth (overstatement). This was done by using the Scherrer formula[47] which follows as

$$t = \frac{0.9\lambda}{B\cos\theta_B}, \qquad [42]$$

where λ is the principle wavelength of the x-ray beam, B is the full-width of the diffraction peak at half the maximum intensity, θ_B is the value of the angle (not 2-θ) at half the peak width, and t is particle size.

Values of B and θ_B were obtained from powder diffraction peaks corresponding to the (001), (101), and (111) $BaTiO_3$ planes and the $Ni_{(111)}$ and $Cr_{(110)}$ peaks. Since the $Ni_{(111)}$ and $Cr_{(110)}$ peaks fall on top of one another it was assumed that either 1) the Ni and Cr were in total solid solution together, or 2) the particle size of Ni and Cr were the same. In either case, the

particle size of the Ni and Cr were not distinguished from one another and instead were termed the "Ni-Cr" phase. Average particle sizes and standard deviations were calculated and are shown in Table X below.

Table X: Average Phase Particle Sizes for Each Powder Sample Calculated Using the Scherrer Formula.

	Phase Avg. Particle Size (nm)	
Powder Sample	**$BaTiO_3$**	**Ni-Cr**
MA-NOHT	308 ± 416	112 ± 59
MA-400HT-1	177 ± 78	99 ± 59
MA-400HT-5	94 ± 20	98 ± 49
MA-500HT-1	126 ± 26	110 ± 55
MA-500HT-5	128 ± 9	144 ± 55
MA-600HT-1	115 ± 42	143 ± 69
MA-600HT-5	104 ± 18	197 ± 46

It can be seen from Table X that average particle size fluctuates wildly between the as-milled powder and the powders annealed at different temperatures and times. All of the powder sizes are within comprehensible limits however. Average $BaTiO_3$ particle size values don't seem to follow any noticeable trend with increasing annealing temperature and/or time. Average Ni-Cr particle sizes appear to increase with increasing annealing temperature and/or time. All of the starting constituent powder sizes were less than 43μm in diameter (-325 mesh) and according to the values listed in Table X, post-milled powder sizes ranged between about 0.1μm to about 0.3μm. These values should be taken as first approximations and not as definitive numbers since the diffractometer used had such poor resolution. Similarly, XRD peak values used in the Scherrer formula are subjective which explains the large standard deviation values.

An attempt was made to characterize whether peak broadening was more likely due to decreased particle size or strain by constructing Williamson-Hall plots for the as-milled and annealed powder samples. Williamson-Hall plots are based on the equation,

$$B\cos\theta_B = -2\left(\frac{\Delta d}{d}\right)\sin\theta_B, \qquad [43]$$

where B is the full-width of the diffraction peak at half the maximum intensity, θ_B is the value of the angle (not $2\text{-}\theta_B$) at half the peak width, and $\Delta d/d$ is the variational strain present in the sample

(representing variances in plane spacings).[47] Derivation of the methods used in arriving at this governing equation will not be explored here. Individual phase diffraction peaks ($BaTiO_3$ and Ni-Cr) were analyzed for each powder sample and values for B and θ_B were determined. Values of $B\ cos\ \theta_B$ were plotted against values of $sin\ \theta_B$ and normalized by dividing each term by the characteristic principle wavelength of the X-ray beam (1.5406 Cu K-alpha1). Regression analysis was then used to obtain trend lines for the data.

It can be seen in Equation [43] that the slopes of these trend lines are equal to $-2(\Delta d/d)$. The general behavior of the plots and the conclusions that can be drawn are as follows: If peak broadening is controlled by crystallite size then $B\ cos\ \theta_B$ will be constant for all of the peaks (horizontal line); If peak broadening is controlled by strain then $B\ cos\ \theta_B$ will be a linear function of $sin\ \theta_B$ and the larger the slope of the line, the more effect that strain has.

Williamson-Hall plots for all of the $BaTiO_3$ diffraction peaks are shown in Figure 36. Based on the slopes of the trend lines, it can be inferred that the as-milled $BaTiO_3$ peak broadening behavior was dominated by strain to the most extent while the lower annealing temperatures and times (400°C, 500°C, 1hr) were controlled by strain to a lesser extent. The powders that were annealed for 500°C and 600°C for five hours showed that $BaTiO_3$ peak broadening was controlled by particle size and not so much by strain. This is to be expected since the most strain relief occurs during annealing treatments done at higher temperatures and longer times.

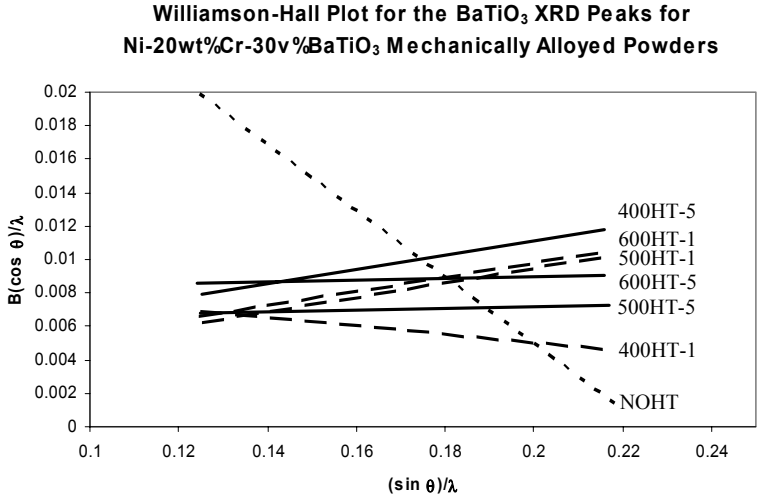

Figure 36: Williamson-Hall plots of $BaTiO_3$ peaks for all of the powder samples.

Williamson-Hall plots for all of the Ni-Cr diffraction peaks are shown in Figure 37. Based on the slopes of the trend lines, it can be inferred that Ni-Cr peak broadening for the lower time and temperature annealing treatments (400°C 1hr and 5hr, 500°C 1hr, 600°C 1hr) was dominated by strain. The powders that were annealed for 500°C and 600°C for five hours showed that Ni-Cr peak broadening was controlled more by particle size and not so much by strain. It should be commented on that slopes of the Ni-Cr trend lines in Figure 37 are larger than the slopes of the $BaTiO_3$ ones in Figure 36. This makes sense in that larger slopes represent a larger peak broadening dependence on strain and Ni-Cr, being a more ductile phase than the ceramic $BaTiO_3$, should be more strained during milling that that of the more brittle $BaTiO_3$ particles.

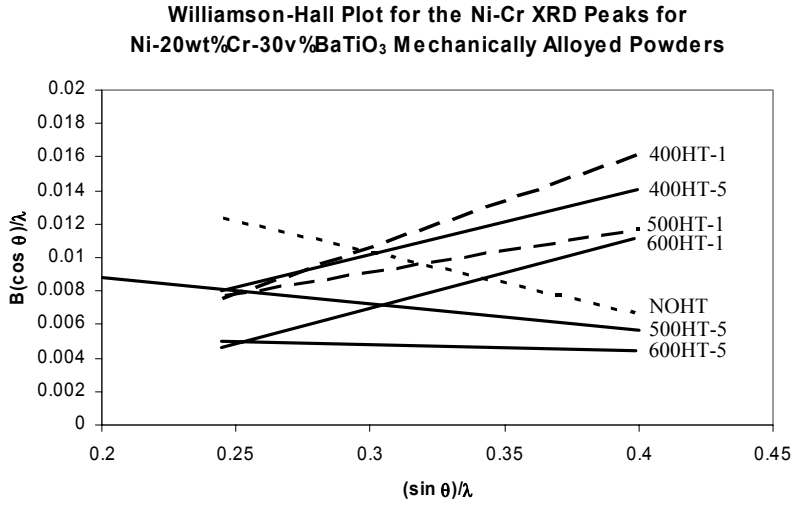

Figure 37: Williamson-Hall plots of Ni-Cr peaks for all of the powder samples.

Finally, relative volume fractions of the $BaTiO_3$ phase were calculated by dividing the area under all of the $BaTiO_3$-specific peaks by the total area under all of the diffraction peaks for each powder sample. It was not possible to do the same for Cr since its peaks (if present at all) were indistinguishable from the Ni peaks. Peak areas were determined using DRXWin 2.2 XRD analysis software.

Table XI shows these calculated values along with the total average volume percent. It can be seen that the calculated volume percent values of $BaTiO_3$ fluctuated between about 20v% to 26v%. Calculated values were not too far off from the theoretical value of 30v% which is predicted from the starting constituent stoichiometry. They are in good agreement considering

the difficulty in determining exact peak boundaries in the XRD patterns due to interference, poor diffractometer resolution, and particle size and strain broadening.

Table XI: Calculated $BaTiO_3$ Volume Percent Values for all of the Powder Samples.

Powder Sample	Calculated $BaTiO_3$ v%	Avg. v%
MA-NOHT	20	
MA-400HT-1	20.5	
MA-400HT-5	25	
MA-500HT-1	26	23.6 ± 2.4
MA-500HT-5	24.5	
MA-600HT-1	24.5	
MA-600HT-5	25	

In summary, it appears from the XRD patterns that all of the composite powder samples are mixtures of the starting constituents while some of the chromium probably exists as a solid substitutional element in the FCC nickel lattice, although it is unclear as to exactly what extent this occurs. This would not be uncommon or surprising since Cr and Ni have similar atomic radii (0.128nm vs. 0.124nm) and the binary phase diagram for nickel and chromium indicates that chromium has solubility in nickel up until about 22wt% at room temperature. This coupled with the fact that the mechanical alloying process leads to such intimately mixed microstructures and attains such a large level of straining, leads to even more of an affinity for chromium dissolution in nickel. The strong presence of $BaTiO_3$ peaks in all of the XRD patterns is indication that the $BaTiO_3$ crystal structure remained intact during milling, although it is unclear as to whether the structure remained tetragonal or converted to cubic. It was worried that the $BaTiO_3$ might disassociate and the ionic forms of Ba, Ti, or O might dissolve in either Ni and/or Cr. This was not evident in the XRD patterns and it appears that the powders are comprised of volume percentages of $BaTiO_3$ close to the predicted value of 30v%.

3.2.3.2 Optical Microscopy

Optical microscopy was performed on the as-milled composite powder and on all of the powders that were annealed for five hours. Since there were no significant differences noticed during X-ray diffraction characterization between the powder samples annealed for one hour versus the ones annealed for five hours, it was decided that optical analysis of the five hour annealed samples would be sufficient for characterization. All optical micrographs are of as-polished and un-etched powder specimens.

Figure 38 shows individual composite particle cross-sections of the as-milled sample as well as the samples annealed at 400°C, 500°C, and 600°C for five hours. The inter-dispersed white particles in each micrograph are the $BaTiO_3$ reinforcement and are in the size range of about 4μm down to less than 1μm in diameter. The black spots are pores that were introduced during the milling process and the dark lines are cracks. It can be seen in all of the micrographs that the $BaTiO_3$ particles appear to be well dispersed throughout the nickel-chromium matrix and that there doesn't appear to be any significant difference between the microstructures of all the powder specimens, whether they were annealed or not.

MA-NOHT ***MA-400HT-5***

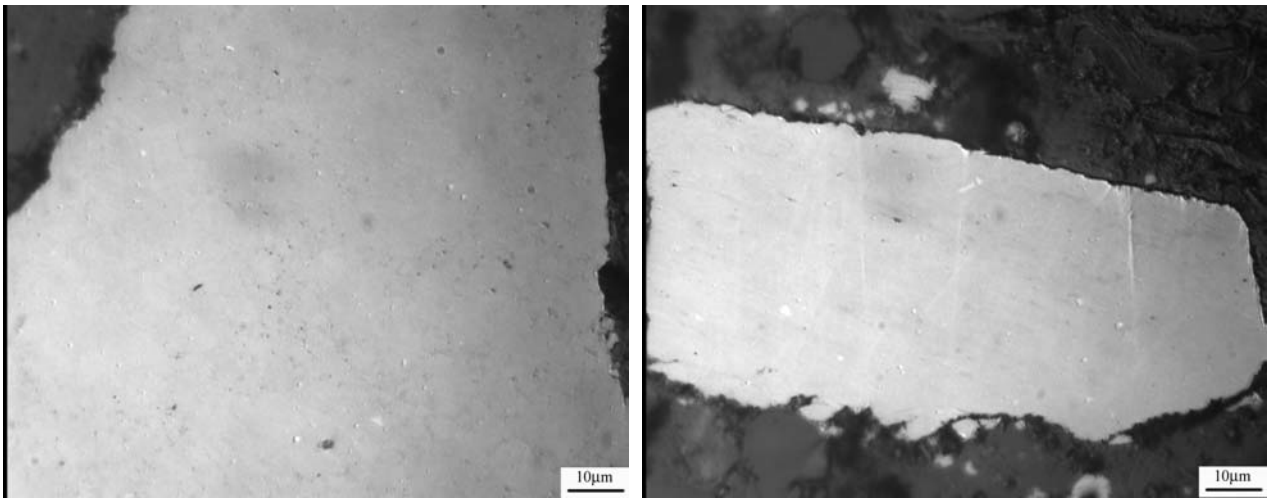

MA-500HT-5 ***MA-600HT-5***

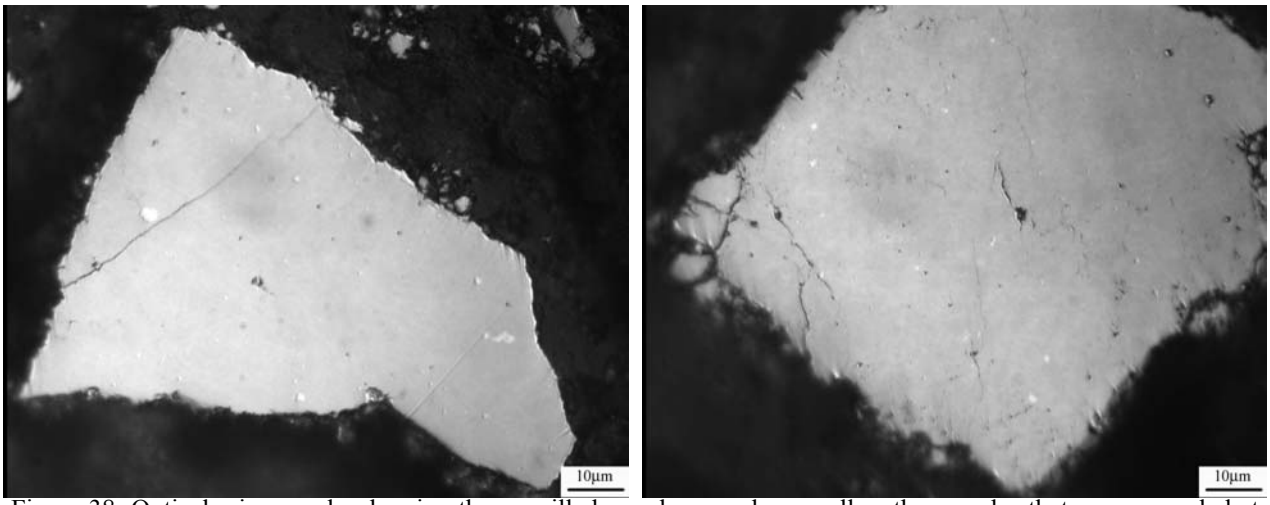

Figure 38: Optical micrographs showing the as-milled powder sample as well as the samples that were annealed at 400°C, 500°C, and 600°C for five hours.The white particles dispersed throughout the nickel-chromium matrix are barium titanate.Note that these particles are in the size range of about 4µm down to less than 1µm in diameter. Black particles are actually pores that developed during the mechanical alloying process and the black lines are cracks.

It should be said that there inevitably must be $BaTiO_3$ particles present in all the powder samples that are too small to be optically resolved by the microscope used to obtain the micrographs in Figure 38. This stems from several facts including that the micrographs were taken using the highest magnification possible by the scope, the $BaTiO_3$ starting powder had particle sizes in the nanometer range to begin with (Figure 30), and mechanical alloying leads to highly refined particle sizes for brittle phases ($BaTiO_3$).

3.2.3.3 SEM and EDS Analysis

A scanning electron microscope was used to obtain micrographs of the surface morphology of the un-mounted powder specimens and the internal microstructure of the mounted ones. Additionally, chemical analysis was performed on the mounted specimens using energy dispersive spectroscopy. Figure 39 shows the general powder particle surface morphology of the as-milled sample and the samples annealed for 400°C, 500°C, and 600°C for five hours each. Powder particle surfaces appear highly-irregular in roughness and shape which is common in a mechanical alloying process. There doesn't appear to be significant surface differences between any of the specimens.

MA-NOHT ***MA-400HT-5***

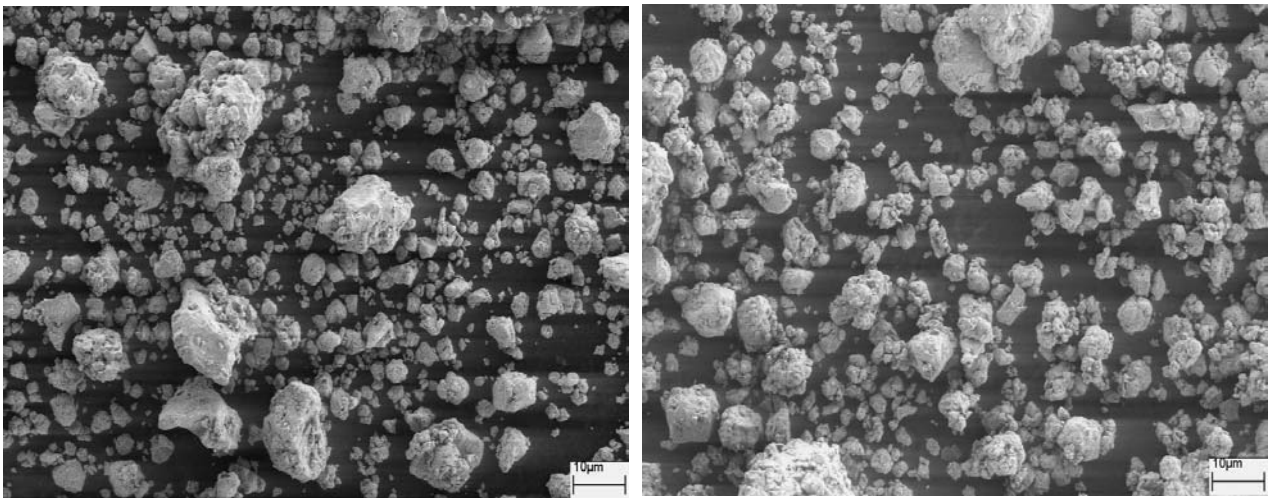

MA-500HT-5 ***MA-600HT-5***

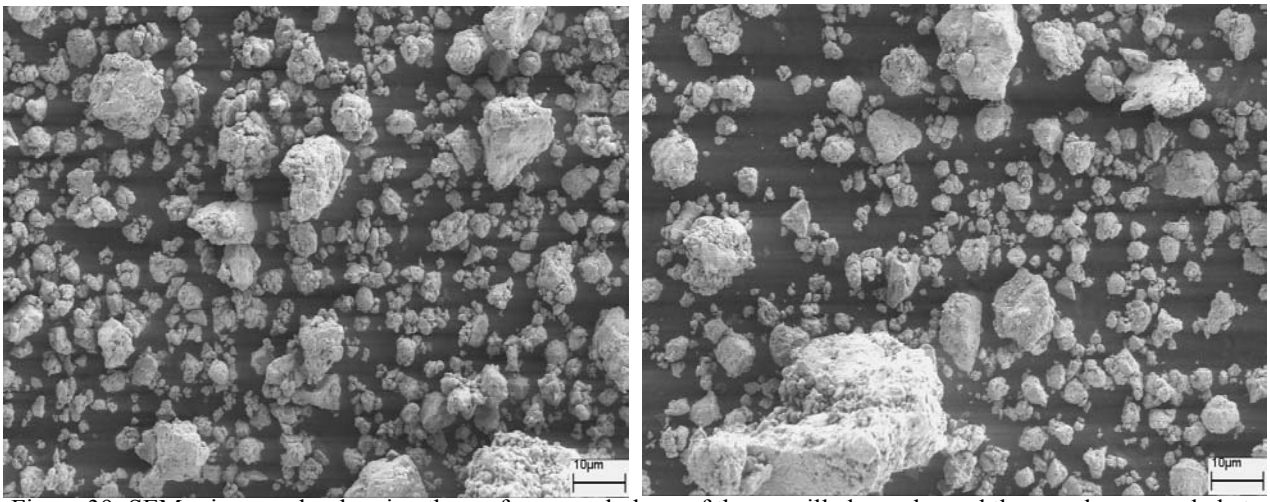

Figure 39: SEM micrographs showing the surface morphology of the as-milled powder and the powders annealed at 400°C, 500°C, and 600°C for five hours. All powders are characterized by a highly-irregular surface roughness and shape which is common in mechanical-alloying processes.

Mechanical alloying processes are well known to result in composite powders that appear lamellar or folded in nature due to the repeated cold-welding of the ductile constituents. Figure 40 shows micrographs of the as-milled powder and the powder annealed at 400°C for five hours that exhibit this layered morphology. Additionally, a milling ball indentation can be seen in the *MA-NOHT* micrograph and both micrographs are representative of the morphology of all of the powder samples.

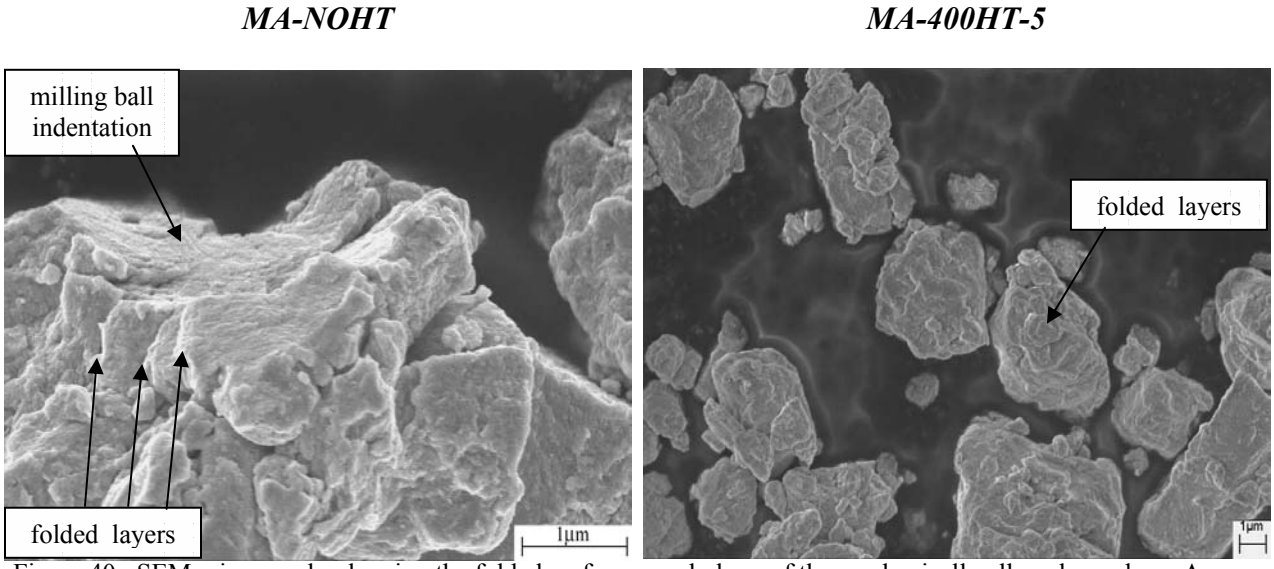

Figure 40: SEM micrographs showing the folded surface morphology of the mechanically alloyed powders. A milling ball indentation can be seen in the micrograph of the as-milled sample. (micrographs are representative of all of the powders)

All of the mounted and polished powder samples were examined with the SEM; first equipped with a secondary electron detector and later with a backscattering detector. Powder microstructures typified in Figure 38 proved elusive for all of the samples when using the secondary electron detector for SEM imaging except for the as-milled powder. This was thought to be due to the small $BaTiO_3$ particle sizes and the loss of color imaging when going from the optical microscope to the black and white SEM image screen. Upon successful imaging of the as-milled powder it was realized that instrument brightness and contrast settings must be set within a very specific range in order to detect the $BaTiO_3$ particles when utilizing the secondary electron detector. Unfortunately these imaging conditions were never duplicated again.

A backscatter electron detector was used in the SEM in an effort to obtain better images of the powder microstructures. It was thought that backscattered electrons might provide more image contrast between the Ni, Cr, and $BaTiO_3$ phases as opposed to secondary emitted electrons. Backscattered electrons are ones from the source beam that are deflected opposite the beam direction due to interactions between specimen atomic nuclei, mainly that of protons. Since Ni has the most protons in its nucleus (Z = 28) with Cr (Z = 24) and $BaTiO_3$ (Z_{avg} = 20) following closely behind, it would be expected that the $BaTiO_3$ particles would appear as darker regions, with Cr appearing less dark and Ni appearing the brightest. This proved to be true for all of the powder specimens.

Figure 41 shows two SEM micrographs of the unetched as-milled powder. Figure 41 (a) is an image taken using the secondary electron detector while Figure 41 (b) was taken using the backscatter detector. The brightness and contrast of image (a) was enhanced using Adobe Photoshop software in order to bring out the dispersion of the light-colored $BaTiO_3$ particles. The particles present in the figure appear to be on the order of less than one micron in diameter and are very well dispersed throughout the Ni-Cr matrix. Since $BaTiO_3$ is a brittle ceramic phase and mechanical alloying is impact-intensive, it can be expected that smaller, irresolvable particles exist within the microstructure of the composite powder

Energy dispersive spectroscopy (EDS) was used to obtain elemental information for two different portions of Figure 41 (b). As can be seen, elemental weight percentages match up quite well for the bulk composite material while the darker region is high in chromium content, either representing a Cr-rich phase or an undissolved Cr particle. Since the EDS spot size is about 1μm in diameter, pin-point elemental analysis is not possible. Rather, elemental electron energies are obtained over about a ¾ μm^2 spot area. It's reasonable to believe that an increase in a particular elemental percentage (Ni,Cr) or groups of elements (Ba,Ti,O) coupled with a visual irregularity in microstructure is actually the constituent who's elemental components are increased. Barium titanate particles are definitely present in Figure 41 (b) based on the EDS results, however it is believed that particle sizes were too small to be resolved at the image magnification.

MA-NOHT – Secondary e^- detector

MA-NOHT – Backscatter e^- detector

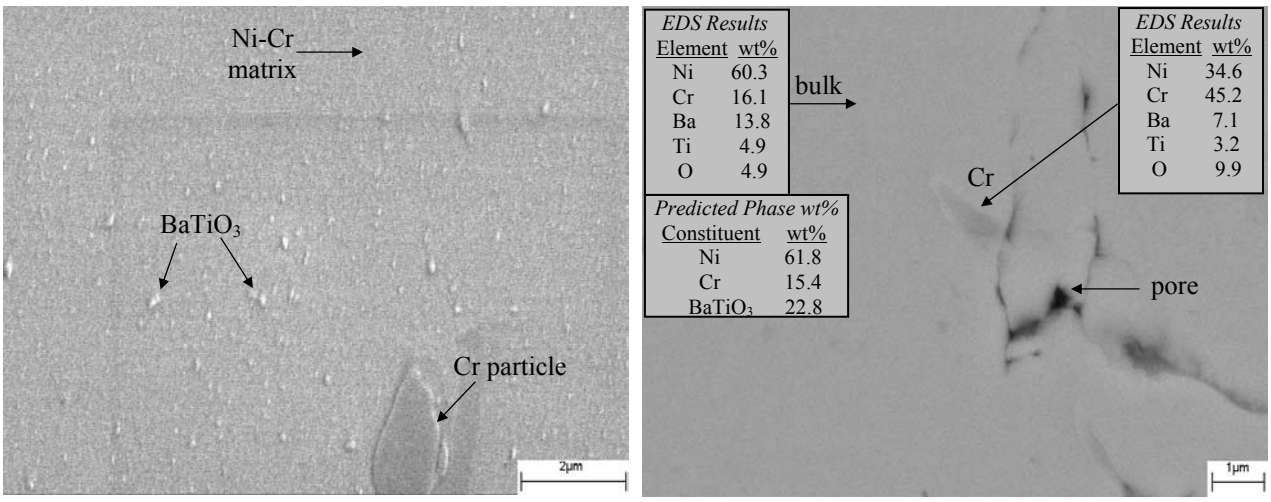

(a) (b)

Figure 41: SEM micrographs showing the un-etched microstructure of the as-milled powder sample using a secondary electron detector and a backscattering detector.

It should be noted that Figure 41 (a) was the only successful image of the $BaTiO_3$ dispersion using the secondary electron detector. The internal powder microstructure in Figure 41 (a) and (b) is more than likely representative of all of the powder samples based on the microstructures shown in Figure 38 and on X-ray diffraction data.

Figure 42 shows a SEM micrograph of the polished and etched powder that was annealed at 400°C for five hours. The bulk phase EDS results show a good correspondence to the predicted weight percent values, except that there is an unusual increase in oxygen content. This can be attributed to the oxidation of both the Ni and Cr metals during the chemical etching procedure. The outcropping of several darker particles were determined to be $BaTiO_3$ particles based on an increase in EDS weight percentage values for barium and titanium. The weight percent of oxygen decreased from the bulk composite value of 14.5% to the $BaTiO_3$ value of 7.7%. This is another indication that the darker particles are indeed $BaTiO_3$ in that ceramic barium titanate does not oxidize as readily in the presence of the chemical etchant (70v%HCl, 30v%H_2O_2) as do nickel and chromium.[46] Therefore, lower oxygen content would be expected around a less-oxidized $BaTiO_3$ region as opposed to a more oxidized Ni-Cr region.

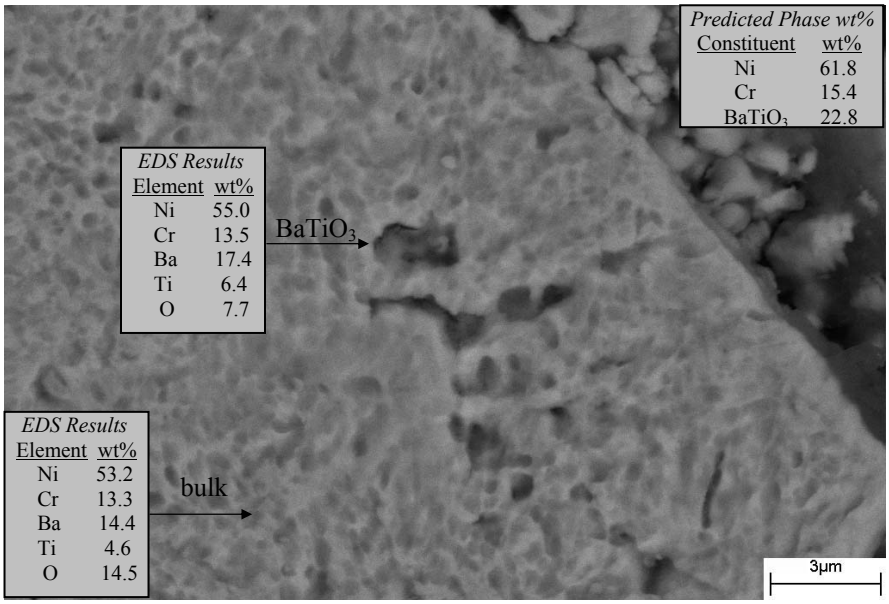

Figure 42: SEM micrograph of the etched *MA-400HT-5* powder sample using a backscattering detector.

It was originally thought that the darker, inter-dispersed regions in Figure 42 were actually $BaTiO_3$ particles, but upon more careful examination it can be seen that they are actually depressions. It is thought that these are areas in which preferential etching occurred, most likely due to small surface imperfections or areas that were more strained than surrounding areas during mechanical alloying.

3.2.3.4 TEM Characterization

Transmission electron microscopy was used to gain better insight into the microstructure of the composite powder. Specifically, images and diffraction patterns were acquired for the *MA-NOHT* powder. Figure 43 shows TEM images of one of the as-milled powder particles and two different diffraction patterns taken from different areas of the particle.

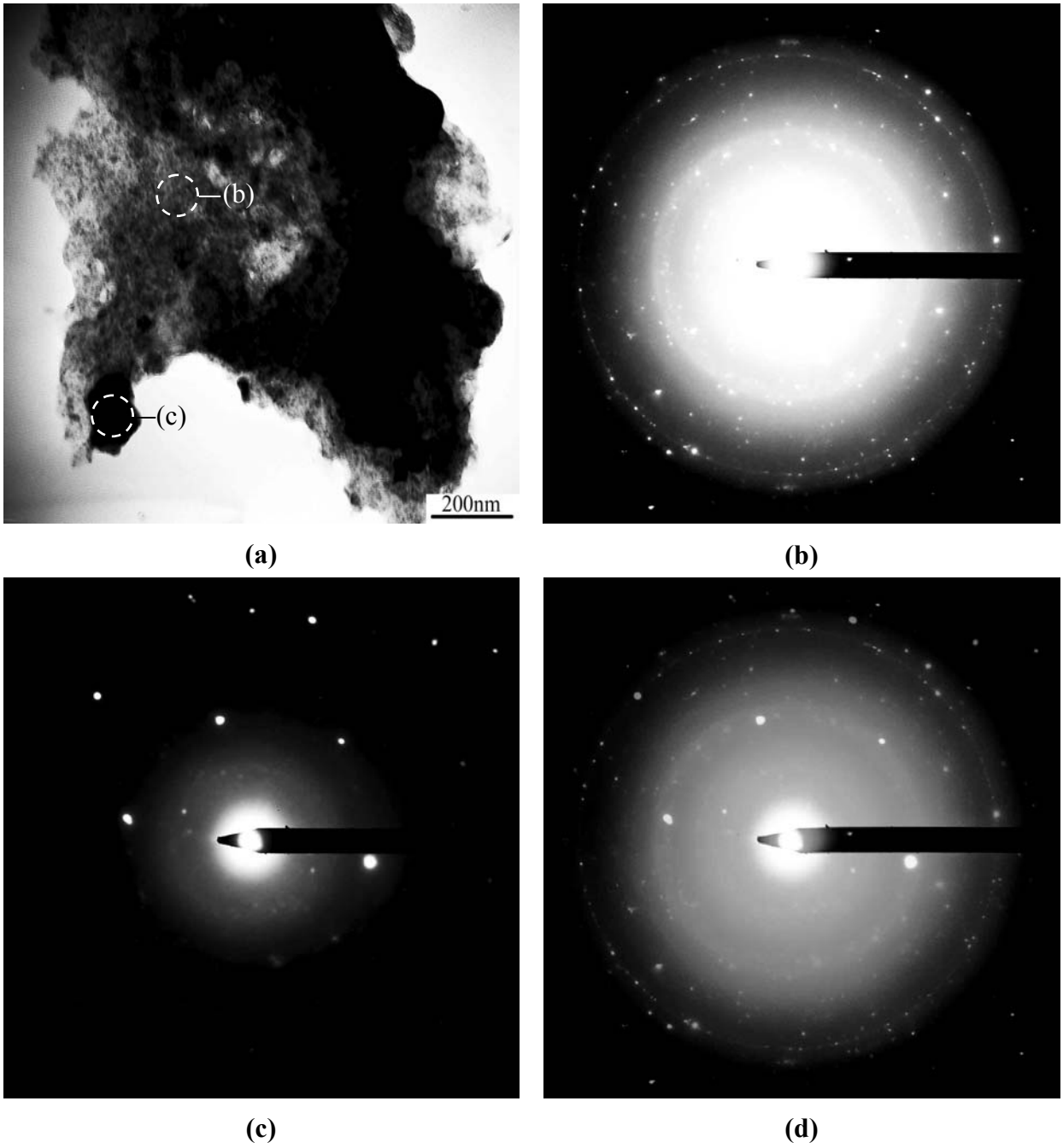

Figure 43: Results from TEM analysis showing one *MA-NOHT* powder particle in (a), a polycrystalline diffraction image in (b), a single crystal diffraction pattern in (c), and a composite diffraction pattern in (d) consisting of an overlay of (b) and (c). Areas from which diffraction patterns originated are marked in (a).

Figure 43 (a) is characterized by a large concentration of dispersed dark particles and areas of increased thickness that were too large to allow transmission of the electron beam. The diffraction pattern in (b) was acquired from the area labeled in image (a). The discrete diffraction spots in image (b) represent larger grain size while the continuous rings represent a much smaller grain size. Specific grain size measurements were not performed due to difficulty associated with obtaining the camera constant for the instrument that was used. What's important to note is that a wide range of grain size is present in the sample. This is in agreement with typical mechanically alloyed powder microstructures.

The diffraction pattern in Figure 43 (c) was acquired from the large dark particle marked in (a). Much effort was made in obtaining a full diffraction pattern from this spot, ultimately however only the portion shown was able to be imaged. This particle's composition is limited based on previous characterization, with the only possible choices being nickel, chromium, or barium titanate. An attempt at indexing this pattern was made by comparing it, as well as distances between diffraction spots, and angles between planes to standard patterns for FCC and BCC materials (Ni,Cr), as well as tabulated values of angles between planes in both the cubic and tetragonal systems. [48] A complete match was never made due to several angle inconsistency problems and a definite determination as to the particle's crystal structure was never reached.

Both nickel and chromium are ductile metals and repeated milling leads to crystallite refinement and cold-welding between the two. This means that individual grains become highly strained and intermixed making the chances low that a large enough fully-oriented Ni or Cr area exists after milling that will result in a distinct diffraction pattern. On the other hand, barium titanate is a brittle ceramic that exhibits a much less-strained internal structure post-milling. Chances are greater that a $BaTiO_3$ area exists within the powder microstructure that has a large enough oriented crystalline area to produce the distinct diffraction pattern shown in Figure 43 (b). It is this reason as to why it is thought that the dark particles in Figure 43 (a) are $BaTiO_3$.

Figure 43 (d) shows a composite image consisting of an overlay of the diffraction patterns in (b) and (c). It can be seen that the bright diffraction spots present in (c) are spaced at distances corresponding to the radii of the discrete diffraction rings from image (b). It can be inferred that the discrete rings in (b) and the diffraction spots in (c) come from crystals with the same d-spacing. This means that the diffracting dark particle in (c) is probably the same as the

smaller dark particles from the diffracted area in (b). This gives further justification that the dark areas are probably $BaTiO_3$ since $BaTiO_3$ particles should be much smaller and more prevalent than any isolated particles of Ni or Cr. If it is true that the dark particles are indeed $BaTiO_3$ then individual particles are well within the 25-50 nm size range.

3.2.4 Discussion on Mechanical Alloying Results

X-ray diffraction measurements should be taken with a word of caution. The diffractometer that was used to acquire the data has poor intrinsic resolution resulting in slight peak broadening. Correspondingly, accurate crystal structure determinations such as lattice cell parameters are not best suited by this diffractometer. Rather, XRD scans from this unit are best utilized for rapid phase identification and not so much for quantitative analysis. Therefore, average particle size predictions and peak broadening determinations obtained from Williamson-Hall plots should be taken with this in mind. General trends in powder behavior should be true however since all results were based on relative XRD peak analysis, meaning that powder patterns were compared to one another and not to outside sources.

Similarly, an exhaustive 2-θ range was not used in order to save diffraction scan time for each sample. Although the range used (15°-70° 2-θ) encompassed most of the important diffraction peaks for the composite constituents, some peaks were left off. Namely, a diffraction peak should exist for $Cr_{(211)}$ at about 81.7° 2-θ that has a relative intensity greater than that of its (200) peak. Accordingly, if a greater 2-θ range were used, then it's possible that the diffractometer would have detected this peak, giving us proof as to the existence of undissolved Cr. Also, the fact that some peaks were left off due to the contracted 2-θ range directly affects the calculation for average crystallite size and phase volume fractions. Additional diffraction peaks would have increased the accuracy of the particle size and phase fraction calculations.

It is difficult to determine the extent of chromium dissolution in nickel by XRD analysis, simply because nickel and chromium's most-intense peaks (111) and (110), respectively, occur at such similar 2-θ values. Additionally, the Ni peak is much more intense than the Cr peak, effectively dominating any other diffraction peaks around it. In effect, even if Cr existed as a separate phase in the composite powder, detection of its diffraction peak would not be possible. It's unfortunate that the only other useful Cr diffraction peak (200) occurs at such a low

intensity. Again, even if Cr were separately present in the composite powder, this peak would be dwarfed by the other more-intense diffraction peaks, rendering it unnoticeable.

The greater presence of Ni in the composite powders as opposed to Cr or $BaTiO_3$ (≈62wt% vs.15 and 23wt% respectively) means that XRD results will exhibit more intense Ni diffraction peaks simply because there is more if it present. The dominant Ni peaks coupled with the fact that the main characteristic tetragonal $BaTiO_3$ peak occurs so close to the 2-θ values for the $Ni_{(111)}$ and $Cr_{(110)}$ peaks, means that the characteristic tetragonal $BaTiO_3$ peak would be masked even if it were present. This makes it impossible to determine whether or not tetragonal $BaTiO_3$ is present in the composite powders from XRD analysis. It was already mentioned that it were possible that the starting tetragonal $BaTiO_3$ may have transformed to the cubic form due to increased system temperature and strain during milling. It's unfortunate then that neither XRD analysis nor TEM proved fruitful in decisively determining the crystal structure of $BaTiO_3$. It is hoped that determination will become easier once the powder is consolidated into a bulk form. High-temperature consolidation may coarsen some of the $BaTiO_3$ particles, allowing for more attainable diffraction patterns from them during TEM analysis.

The goal of heat treating was to gain knowledge into thermal-related processes for the composite powder such as the extent of strain recovery as a function of time and temperature and also to find out whether or not any "hidden" phases existed within the powder that didn't show up in the as-milled XRD scan. Bearing this in mind, more detailed heat treatment trials are necessary in order to completely map the appropriate annealing schedule for this specific composite powder. The composite powders are planned to be consolidated at high temperature anyway, meaning that appropriate heat treatments may have to be carried out post-consolidation to attain the desired microstructure. It's probable though that the high temperature required for consolidation (≈1100°C for HIPing) will result in a completely recovered microstructure and well-dispersed $BaTiO_3$ particles. This fact tends to nullify the heat treatment trials carried out during this work.

3.2.5 Summary of Mechanical Alloying Results

X-ray diffraction scans performed on the as-milled composite powder and on all of the annealed powders showed that each was composed of a mixture of Ni, Cr, and $BaTiO_3$ in relative proportions equivalent to the starting stoichiometry. Since it was determined that no reactions

occurred during milling, there is no reason to believe that the composite powders consist of anything other than the pure starting constituents. All of the powders exhibited XRD peak broadening and slight shifting to lower 2-θ values which was attributed to induced strain and reduced crystallite size of the constituents during milling. X-ray diffraction peaks sharpened after the annealing treatments, especially for the powders that were annealed at 500°C for five hours and 600°C for one and five hours. This was attributed to recovery of some of the strain induced during milling. No proof was acquired showing that the powders were completely recovered even after the highest temperature heat treatment for the longest time (600°C, five hours). Williamson-Hall plots revealed that peak broadening was dominated by strain for both the $BaTiO_3$ and the Ni-Cr phase for all samples except the ones annealed at 500°C and 600°C for five hours. Peak broadening was dominated more by crystallite size as opposed to strain for these higher temperature annealing treatments. Average particles size predictions based off of XRD peak width resulted in an array of values ranging between about 0.1μm to about 0.3μm. Lastly, $BaTiO_3$ volume fraction predictions resulted in values between 20 and 25v%, as compared to the starting stoichiometric prediction of 30v%.

X-ray diffraction and SEM/EDS analysis revealed that not all of the Cr was dissolved in the Ni during milling, although it is unclear as to amount of un-dissolved Cr present. It is also unclear as to whether or not the tetragonal form of $BaTiO_3$ was retained during milling, even after utilization of all of the characterization techniques. Difficulty in determining this stems from the fact that the tetragonal form of $BaTiO_3$ is just slightly so, therefore making it difficult to determine from composite XRD measurements and TEM diffraction patterns.

Optical microscopy coupled with SEM and TEM analysis revealed that the $BaTiO_3$ particulate phase was well-dispersed throughout a Ni-Cr matrix while no noticeable difference was seen between the microstructures of the annealed samples and the as-milled powder. Barium titanate particle size was found to vary between about 25nm and 1μm which is not uncommon for brittle phases during a mechanical alloying process.

3.3 Comprehensive Summary

- A mathematical model has been created based on Eshelby's equivalent inclusion method that can predict composite stiffness and mechanical damping capability for any piezoelectric ceramic-reinforced composite system.
- On average, the model predicts that low-stiffness, high-conductivity metal matrices such as copper, aluminum, and magnesium tend to exhibit greater levels of mechanical damping as opposed to stiffer, more resistive matrices.
- Of the three different piezoelectric ceramic reinforcements modeled, $PbTiO_3$ is predicted to exhibit the largest capability of mechanical damping, followed by $BaTiO_3$ and ZnO.
- Different inclusion shapes and aspect ratios result in variances in predicted composite stiffness and damping capabilities with larger aspect ratios giving larger predicted values.
- Model predictions should be used as a tool to rank potential composite systems and not as a definitive prediction of specific stiffness and damping values.
- X-ray diffraction characterization showed that all of the mechanically alloyed powders were composed of a mixture of Ni, Cr, and $BaTiO_3$ in relative proportions equivalent to the starting stoichiometry.
- The powder samples that were annealed at 500°C and 600°C for five hours showed signs of partial strain recovery; however it is unclear as to whether or not they are fully recovered.
- Average particle size calculations from XRD scans resulted in predicted diameters between 0.1μm and 0.3μm for all of the powders, while volume fraction predictions resulted in $BaTiO_3$ phase values between 20 and 25v%.
- Some un-dissolved Cr is present in all of the powder samples and it is still unclear as to whether or not the dispersed $BaTiO_3$ is present in the tetragonal or cubic phase.
- The $BaTiO_3$ phase is well dispersed in all of the powder samples and was experimentally found to have an average particle size ranging between 25nm and 1μm in diameter.
- Mechanical alloying is a viable synthesis technique to create a Ni-20wt%Cr-30v%$BaTiO_3$ composite.

FUTURE WORK

Presently, the mechanically alloyed Ni-20wt%Cr-30v%$BaTiO_3$ powder system has been mass-produced by repeated SPEX milling runs and is awaiting HIP consolidation at Michigan Tech. Additionally, a composite system identical to the $BaTiO_3$-reinforced one except with non-piezoelectric ZrO_2 as the reinforcement is currently undergoing exploratory trials in hopes of ultimately being mass-produced and consolidated for use as an experimental control for vibration damping testing. It is hoped that the piezoelectric ($BaTiO_3$) reinforced composite system will exhibit a damping capability beyond that of the non-piezoelectric (ZrO_2) reinforced system, thereby giving credence to the electromechanical damping mechanism theorized in this thesis.

Lastly, this thesis documentation represents one half of the present status of this project and merely the beginning of much more research work to come. Jennifer Franklin has investigated many more piezoelectric ceramic-reinforced metal matrix composite systems and results from her work can be found in her thesis submittal. By combining results obtained from composite modeling trials presented in this work with the composite synthesis foundation paved by Jennifer and myself, future research focus will be placed on those systems which seem most appropriate for further exploration. It is hoped that this research project will culminate in the successful creation, consolidation, and application of several different piezoelectric ceramic-reinforced metal matrix composite systems.

REFERENCES

[1] T. W. Clyne and P. J. Withers, *An introduction to metal matrix composites* (New York NY USA : Cambridge University Press, Cambridge England ;, 1993).

[2] P. S. Gilman and J. S. Benjamin, Annual Review of Materials Science **13,** 279-300 (1983).

[3] R. M. German, *Powder Metallurgy Science*, second ed. (Metal Powder Industries Federation, Princeton, New Jersey, 1994).

[4] B. Yang and X. M. Chen, Journal of the European Ceramic Society **20,** 1687-1690 (2000).

[5] X. M. Chen and B. Yang, Materials Letters **33,** 237-240 (1997).

[6] R. K. N. D. Rajapakse and X. Zeng, Acta Materialia **49,** 877-885 (2001).

[7] R. F. Singer and G. H. Gessinger, Metallurgical Transactions A **13A,** 1463-1470 (1982).

[8] X. Han, X. Li, and S. X. Mao, Metallurgical & Materials Transactions A-Physical Metallurgy & Materials Science **33,** 2835-2845 (2002).

[9] W. Lu, D. N. Fang, and K. C. Hwang, Theoretical and Applied Fracture Mechanics **37,** 29-38 (2001).

[10] G. C. Sih, Theoretical and Applied Fracture Mechanics **38,** 1-14 (2002).

[11] S. Sastry, M. Krishna, and J. Uchil, Journal of Alloys and Compounds **314,** 268-274 (2001).

[12] Y. Liu, J. Li, G. Yang, and Y. Lu, Journal of Materials Processing Technology **106,** 94-98 (2000).

[13] N. Srikanth and M. Gupta, Composites Science and Technology **63,** 559-568 (2003).

[14] J. N. Wei, H. F. Cheng, Y. F. Zhang, F. S. Han, Z. C. Zhou, and J. P. Shui, Materials Science and Engineering A **325,** 444-453 (2002).

[15] A. D. Nashif, D. I. G. Jones, and J. P. Henderson, *Vibration damping* (Wiley, New York, 1985).

[16] H. H. Law, P. L. Rossiter, G. P. Simon, and L. L. Koss, Journal of Sound and Vibration **197,** 489-513 (1996).

[17] V. R. Buravalla, C. Remillat, J. A. Rongong, and G. R. Tomlinson, Smart Materials Bulletin **2001,** 10-13 (2001).

[18] Y. Suda and H. Komine, Wear **191,** 72-77 (1996).

[19] S. Durieux, C. Esnouf, E. Maire, J. P. Fondere, R. Fougeres, G. Lormand, and A. Vincent, Scripta Materialia **36,** 189-193 (1997).

[20] J. Banhart, J. Baumeister, and M. Weber, Materials Science and Engineering A **A205,** 221-228 (1996).

[21] W. Jiejun, L. Chenggong, W. Dianbin, and G. Manchang, Composites Science and Technology **63,** 569-574 (2003).

[22] J. Van Humbeeck, Materials Science and Engineering A **273-275,** 134-148 (1999).

[23] M. O. Moroni, R. Saldivia, M. Sarrazin, and A. Sepulveda, Materials Science and Engineering A **335,** 313-319 (2002).

[24] M. C. Piedboeuf, R. Gauvin, and M. Thomas, Journal of Sound and Vibration **214,** 885-901 (1998).

[25] A. Baz and A. Tempia, Proceedings of the IEEE Conference on Decision & Control Including the Symposium on Adaptive Processes. v 3 1998**,** 2946-2951.

[26] M. Arafa and A. Baz, Composites Science & Technology **60,** 2759-2768 (2000).

[27] Y. Suzuki, K. Uchino, H. Gouda, M. Sumita, R. E. Newnham, and A. R. Ramachandran, Journal of the Ceramic Society of Japan, International Edition **99,** 1096-1098 (1991).

[28] G. A. Lesieutre, Shock & Vibration Digest **30,** 187-195 (1998).

[29] M. Hori, T. Aoki, Y. Ohira, and S. Yano, Composites Part A: Applied Science and Manufacturing **32,** 287-290 (2001).

[30] B. Jaffe, W. R. Cook, and H. L. C. Jaffâe, *Piezoelectric ceramics* (Academic Press, London, New York,, 1971).

[31] W. D. Callister, *Materials Science and Engineering: An Introduction*, 4 ed. (John Wiley and Sons, Inc., 1997).

[32] J. D. Eshelby, Proc. Roy. Soc. **A241,** 376-396 (1957).

[33] T. Mura, *Micromechanics of Defects in Solids*, Second, Revised ed. (Martinus Nijhoff Publishers, Dordrecht, 1987).

[34] Mori T and T. K, Acta Metallurgica **21,** 571-574 (1973).

[35] K. Wakashima and H. Tsukamoto, Materials Science and Engineering a-Structural Materials Properties Microstructure and Processing **146,** 291-316 (1991).

[36] K. Wakashima and H. Tsukamoto, Isij International **32,** 883-892 (1992).

[37] G. K. Hu and F. Tian, Mechanics Research Communications **24,** 65-68 (1997).

[38] J. S. Benjamin, Metallurgical Transactions **1,** 2943-2951 (1970).

[39] J. S. Benjamin and T. E. Volin, Metallurgical Transactions **5,** 1929-1934 (1974).

[40] *Nickel, Cobalt, and Their Alloys* (ASM International, 2000).

[41] J. S. Benjamin, in *Mechanical alloying - history and future potential*, Part 7 (of 9) (Novel Powder Processing Advances in Powder Metallurgy. Publ by Metal Powder Industries Federation, Princeton, NJ, USA. v 7.), p. 155-168.

[42] J. S. Benjamin, T. E. Volin, and W. J. H, High Temperatures - High Pressures **6,** 443-446 (1974).

[43] R. C. Benn, J. S. Benjamin, and C. M. Austin, High - Temperature Alloys:Theory and Design (proceedings of a conference)**,** 419-449.

[44] J. S. Benjamin, in *Mechanical alloying process*, Orlando, FL, USA (Proc 1988 Int Powder Metall Conf. Publ by American Powder Metallurgy Inst, Princeton, NJ, USA. v 21 (of vv 18-21).), p. 397-414.

[45] J. S. Benjamin, in *Mechanical Alloying for Preparation of Superalloys*, Grant Symposium (Publ by ASM, Metals Park, OH, USA.), p. 85-91.

[46] G. F. Vander Voort, *Metallography, principles and practice* (McGraw-Hill, New York, 1984).

[47] B. D. Cullity, *Elements of x-ray diffraction*, 2d ed. (Addison-Wesley, Reading, Mass., 1978).

[48] K. W. Andrews, D. J. Dyson, and S. R. Keown, *Interpretation of electron diffraction patterns*, 2d ed. (Plenum Press, New York,, 1971).

[49] Z. Li, M. H. Grimsditch, X. Xu, and S.-K. Chan, Ferroelectrics **141,** 313 (1993).

[50] N. E. Dowling, *Mechanical Behavior of Materials*, Second Edition ed. (Prentice Hall, 1999).

Appendix A:
Composite Constituent Data

Piezoelectric Reinforcement

$BaTiO_3$

Crystal Structure: tetragonal
Space Group: P4mm
Modeled Form: single crystal
E = 64GPa
Data Source: [30]

$$S_{ij} = \begin{pmatrix} 8.05 & -2.35 & -5.24 & 0 & 0 & 0 \\ -2.35 & 8.05 & -5.24 & 0 & 0 & 0 \\ -5.24 & -5.24 & 15.7 & 0 & 0 & 0 \\ 0 & 0 & 0 & 18.4 & 0 & 0 \\ 0 & 0 & 0 & 0 & 18.4 & 0 \\ 0 & 0 & 0 & 0 & 0 & 8.84 \end{pmatrix} \times 10^{-12} \frac{m^2}{N}$$

$$g_{ij} = \begin{pmatrix} 0. & 0. & 0. & 0. & 15.2 & 0. \\ 0. & 0. & 0. & 15.2 & 0. & 0. \\ -23. & -23. & 57.5 & 0. & 0. & 0. \end{pmatrix} \times 10^{-3} \frac{Vm}{N}$$

$PbTiO_3$

Crystal Structure: tetragonal
Space Group: P4mm
Modeled Form: single crystal
E = 47GPa
Data Source: [49]

$$S_{ij} = \begin{pmatrix} 7.1 & -0.4 & -6.3 & 0 & 0 & 0 \\ -0.4 & 7.1 & -6.3 & 0 & 0 & 0 \\ -6.3 & -6.3 & 21.3 & 0 & 0 & 0 \\ 0 & 0 & 0 & 15.4 & 0 & 0 \\ 0 & 0 & 0 & 0 & 15.4 & 0 \\ 0 & 0 & 0 & 0 & 0 & 9.6 \end{pmatrix} \times 10^{-12} \frac{m^2}{N}$$

$$g_{ij} = \begin{pmatrix} 0. & 0. & 0. & 0. & 5.2 & 0. \\ 0. & 0. & 0. & 5.2 & 0. & 0. \\ -3.1 & -3.1 & 9.4 & 0. & 0. & 0. \end{pmatrix} \times 10^{-2} \frac{Vm}{N}$$

ZnO

Crystal Structure: hexagonal
Space Group: 6mm
Modeled Form: single crystal
E = 144GPa
Data Source: http://www.efunda.com

$$S_{ij} = \begin{pmatrix} 7.86 & -3.43 & -2.21 & 0 & 0 & 0 \\ -3.43 & 7.86 & -2.21 & 0 & 0 & 0 \\ -2.21 & -2.21 & 6.94 & 0 & 0 & 0 \\ 0 & 0 & 0 & 23.6 & 0 & 0 \\ 0 & 0 & 0 & 0 & 23.6 & 0 \\ 0 & 0 & 0 & 0 & 0 & 22.6 \end{pmatrix} \times 10^{-12} \frac{m^2}{N}$$

$$g_{ij} = \begin{pmatrix} 0. & 0. & 0. & 0. & -14. & 0. \\ 0. & 0. & 0. & -14. & 0. & 0. \\ -4.9 & -4.9 & 10.4 & 0. & 0. & 0. \end{pmatrix} \times 10^{-2} \frac{Vm}{N}$$

Metal Matrices

Table XII: Mechanical Data for the Metallic Matrices Used in Mathematical Modeling

Metal Matrix	**Young's Modulus, E (GPa)**	**Poisson's Ratio, ν**	**Electrical Resistivity, ρ (10^{-8} Ωm)**	**Data Source**
Aluminum	70.3	0.345	2.71	[50]
Brass	101	0.35	6.08	Knovel.com
Copper	130	0.343	1.71	Knovel.com
Lead	16.1	0.44	21.1	Knovel.com
Magnesium	44.7	0.291	4.48	Knovel.com
Nickel	207	0.31	6.4	eFunda.com
Tin	41.4	0.33	11.5	Knovel.com
Titanium	120	0.361	43	Knovel.com
Tungsten	411	0.28	5.39	Knovel.com
304 Stainless Steel	195	0.28	72	Knovel.com
Mild Steel	212	0.293	9.87	[50]
Ni – 20wt% Cr	216.6	0.31	8.27	eFunda + ROM
Ti – 6Al – 4V	113.8	0.342	178	[50]

Appendix B:
Forms of the Eshelby Tensor

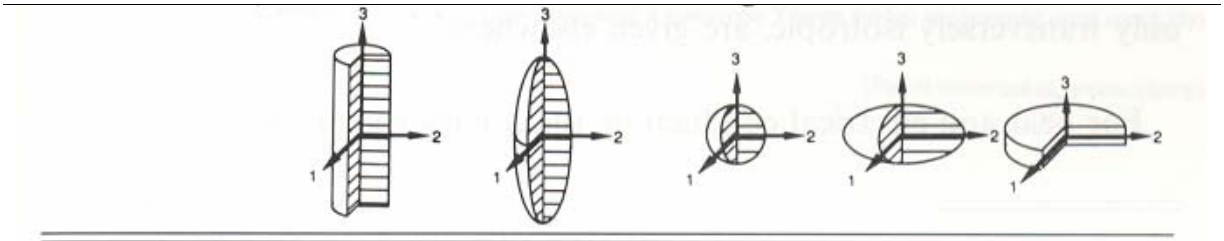

S_{ijkl}	Fibres	Prolate spheroids	Spheres	Oblate spheroids	Plates
S_{3333}	0	$\frac{4Q}{3} + RI_3 + 2s^2T$	$\frac{7-5\nu}{15(1-\nu)}$	$\frac{4Q}{3} + RI_3 + 2s^2T$	1
$S_{1111} = S_{2222}$	$\frac{5-\nu}{8(1-\nu)}$	$Q + RI_1 + \frac{3T}{4}$	$\frac{7-5\nu}{15(1-\nu)}$	$Q + RI_1 + \frac{3T}{4}$	0
$S_{1122} = S_{2211}$	$\frac{-1+4\nu}{8(1-\nu)}$	$\frac{Q}{3} - RI_1 + \frac{4T}{3}$	$\frac{-1+5\nu}{15(1-\nu)}$	$\frac{Q}{3} - RI_1 + \frac{4T}{3}$	0
$S_{1133} = S_{2233}$	$\frac{\nu}{2(1-\nu)}$	$-RI_1 - s^2T$	$\frac{-1+5\nu}{15(1-\nu)}$	$-RI_1 - s^2T$	0
$S_{3311} = S_{3322}$	0	$-RI_3 - T$	$\frac{-1+5\nu}{15(1-\nu)}$	$-RI_3 - T$	$\frac{\nu}{1-\nu}$
$S_{1212} = S_{1221} = S_{2112} = S_{2121}$	$\frac{3-4\nu}{8(1-\nu)}$	$\frac{Q}{3} + RI_1 + \frac{T}{4}$	$\frac{4-5\nu}{15(1-\nu)}$	$\frac{Q}{3} + RI_1 + \frac{T}{4}$	0
$S_{1313} = S_{1331} = S_{3113} = S_{3131} = S_{3232} = S_{3223} = S_{2332} = S_{2323}$	$\frac{1}{4}$	$2R - \frac{I_1R}{2} - \frac{1+s^2}{2}T$	$\frac{4-5\nu}{15(1-\nu)}$	$2R - \frac{I_1R}{2} - \frac{1+s^2}{2}T$	$\frac{1}{2}$
For all other S_{ijkl}	0	0	0	0	0

Figure 44: Forms of the Eshelby shape tensor for several common inclusion shapes.[1]

Appendix C:
Mathematica Code for One Model Run

The Determination of Composite Stiffness and Damping Capabilities of a Piezoelectric-Reinforced Metal-Matrix Composite Using the Eshelby Method

■ Function Definitions

```
(*turns off any spelling errors/warnings due to similar variable names in Mathematica*)
Off[General::"spell1"];
 (*function that obtains the magnitude of a vector, v*)
 mag[v_] = Sqrt[v.v];
 (*defines a function that will accept
    any vector value and output its unit vector equivalent*)
 UnitVector[{a_, b_, c_}] := {a, b, c} / mag[{a, b, c}];
(*defines a 6 x 6 identity matrix for use in Eshelby calculation*)
 identity = IdentityMatrix[6];
 (*this gives the compliance tensor for any bulk polycrystalline material
    (isotropic) given the material's elastic modulus and Poisson ratio*)
Sij_M[Ymodulus_, ν_] := {{1 / Ymodulus, -ν / Ymodulus, -ν / Ymodulus,
     0, 0, 0}, {-ν / Ymodulus, 1 / Ymodulus, -ν / Ymodulus, 0, 0, 0},
    {-ν / Ymodulus, -ν / Ymodulus, 1 / Ymodulus, 0, 0, 0},
    {0, 0, 0, 2 * (1 + ν) / Ymodulus, 0, 0}, {0, 0, 0, 0,
     2 * (1 + ν) / Ymodulus, 0}, {0, 0, 0, 0, 0, 2 * (1 + ν) / Ymodulus}};
 (*Function that takes a tensor quantity and transforms it into a new coordinate
    system given the transformation matrix, "a". The transformation matrix
    is simply the direction cosines between two sets of reference axes*)
 NewTensor[tensor_] := Table[Sum[a[[x, i, o]] a[[x, j, p]]
      a[[x, k, q]] tensor[[o, p, q]], {o, 1, 3},
     {p, 1, 3}, {q, 1, 3}], {i, 1, 3}, {j, 1, 3}, {k, 1, 3}];
 (*function that takes the contracted form of the compliance
    tensor and outputs its expanded form*)
 ExpandCompliance[tensor_] :=
   Table[Which[i + j == 2, Which[k + l == 2, tensor[[1, 1]],
      k + l == 3, 0.5 tensor[[1, 6]], k + l == 4 && k == l,
      tensor[[1, 2]], k + l == 4, 0.5 tensor[[1, 5]], k + l == 5,
      0.5 tensor[[1, 4]], k + l == 6, tensor[[1, 3]]],
     i + j == 3, Which[k + l == 2, 0.5 tensor[[6, 1]], k + l == 3,
      0.25 tensor[[6, 6]], k + l == 4 && k == l, 0.5 tensor[[6, 2]],
      k + l == 4, 0.25 tensor[[6, 5]], k + l == 5,
      0.25 tensor[[6, 4]], k + l == 6, 0.5 tensor[[6, 3]]],
     i + j == 4 && i == j, Which[k + l == 2, tensor[[2, 1]],
      k + l == 3, 0.5 tensor[[2, 6]], k + l == 4 && k == l,
      tensor[[2, 2]], k + l == 4, 0.5 tensor[[2, 5]], k + l == 5,
```

```
      0.5 tensor[[2, 4]], k + l == 6, tensor[[2, 3]]],
     i + j == 4, Which[k + l == 2, 0.5 tensor[[5, 1]], k + l == 3,
      0.25 tensor[[5, 6]], k + l == 4 && k == 1, 0.5 tensor[[5, 2]],
      k + l == 4, 0.25 tensor[[5, 5]], k + l == 5,
      0.25 tensor[[5, 4]], k + l == 6, 0.5 tensor[[5, 3]]],
     i + j == 5, Which[k + l == 2, 0.5 tensor[[4, 1]], k + l == 3,
      0.25 tensor[[4, 6]], k + l == 4 && k == 1, 0.5 tensor[[4, 2]],
      k + l == 4, 0.25 tensor[[4, 5]], k + l == 5,
      0.25 tensor[[4, 4]], k + l == 6, 0.5 tensor[[4, 3]]],
     i + j == 6, Which[k + l == 2, tensor[[3, 1]], k + l == 3,
      0.5 tensor[[3, 6]], k + l == 4 && k == 1, tensor[[3, 2]],
      k + l == 4, 0.5 tensor[[3, 5]], k + l == 5,
      0.5 tensor[[3, 4]], k + l == 6, tensor[[3, 3]]]],
    {i, 1, 3}, {j, 1, 3}, {k, 1, 3}, {l, 1, 3}];
(*function that takes the contracted form of the stiffness
   tensor and outputs its expanded form*)
ExpandStiffness[tensor_] := Table[Which[
    i + j == 2,
    Which[k + l == 2, tensor[[1, 1]], k + l == 3, tensor[[1, 6]],
     k + l == 4 && k == 1, tensor[[1, 2]], k + l == 4, tensor[[1, 5]],
     k + l == 5, tensor[[1, 4]], k + l == 6, tensor[[1, 3]]],
    i + j == 3, Which[k + l == 2, tensor[[6, 1]], k + l == 3,
     tensor[[6, 6]], k + l == 4 && k == 1, tensor[[6, 2]],
     k + l == 4, tensor[[6, 5]], k + l == 5, tensor[[6, 4]],
     k + l == 6, tensor[[6, 3]]],
    i + j == 4 && i == j, Which[k + l == 2, tensor[[2, 1]],
     k + l == 3, tensor[[2, 6]], k + l == 4 && k == 1,
     tensor[[2, 2]], k + l == 4, tensor[[2, 5]], k + l == 5,
     tensor[[2, 4]], k + l == 6, tensor[[2, 3]]],
    i + j == 4, Which[k + l == 2, tensor[[5, 1]], k + l == 3,
     tensor[[5, 6]], k + l == 4 && k == 1, tensor[[5, 2]],
     k + l == 4, tensor[[5, 5]], k + l == 5, tensor[[5, 4]],
     k + l == 6, tensor[[5, 3]]],
    i + j == 5, Which[k + l == 2, tensor[[4, 1]], k + l == 3,
     tensor[[4, 6]], k + l == 4 && k == 1, tensor[[4, 2]],
     k + l == 4, tensor[[4, 5]], k + l == 5, tensor[[4, 4]],
     k + l == 6, tensor[[4, 3]]],
    i + j == 6, Which[k + l == 2, tensor[[3, 1]], k + l == 3,
     tensor[[3, 6]], k + l == 4 && k == 1, tensor[[3, 2]],
     k + l == 4, tensor[[3, 5]], k + l == 5, tensor[[3, 4]], k + l == 6,
     tensor[[3, 3]]]], {i, 1, 3}, {j, 1, 3}, {k, 1, 3}, {l, 1, 3}];
(*function that takes the expanded form of the stiffness tensor
   and outputs its contracted form*)
ContractStiffness[tensor_] :=
  {{tensor[[1, 1, 1, 1]], tensor[[1, 1, 2, 2]],
```

```
     tensor[[1, 1, 3, 3]], 2 * tensor[[1, 1, 2, 3]],
     2 * tensor[[1, 1, 1, 3]], 2 * tensor[[1, 1, 1, 2]]},
    {tensor[[2, 2, 1, 1]], tensor[[2, 2, 2, 2]],
     tensor[[2, 2, 3, 3]], 2 * tensor[[2, 2, 2, 3]],
     2 * tensor[[2, 2, 1, 3]], 2 * tensor[[2, 2, 1, 2]]},
    {tensor[[3, 3, 1, 1]], tensor[[3, 3, 2, 2]],
     tensor[[3, 3, 3, 3]], 2 * tensor[[3, 3, 2, 3]],
     2 * tensor[[3, 3, 1, 3]], 2 * tensor[[3, 3, 1, 2]]},
    {2 * tensor[[2, 3, 1, 1]], 2 * tensor[[2, 3, 2, 2]],
     2 * tensor[[2, 3, 3, 3]], 4 * tensor[[2, 3, 2, 3]],
     4 * tensor[[2, 3, 1, 3]], 4 * tensor[[2, 3, 2, 1]]},
    {2 * tensor[[1, 3, 1, 1]], 2 * tensor[[1, 3, 2, 2]],
     2 * tensor[[1, 3, 3, 3]], 4 * tensor[[1, 3, 2, 3]],
     4 * tensor[[1, 3, 1, 3]], 4 * tensor[[1, 3, 2, 1]]},
    {2 * tensor[[1, 2, 1, 1]], 2 * tensor[[1, 2, 2, 2]],
     2 * tensor[[1, 2, 3, 3]], 4 * tensor[[1, 2, 2, 3]],
     4 * tensor[[1, 2, 1, 3]], 4 * tensor[[1, 2, 2, 1]]}};
(*function that takes the contracted form of a piezoelectric tensor,
  such as "g", and outputs its expanded form*)
ExpandPiezo[tensor_] :=
  {{{tensor[[1, 1]], .5 tensor[[1, 6]], .5 tensor[[1, 5]]},
    {.5 tensor[[1, 6]], tensor[[1, 2]], .5 tensor[[1, 4]]},
    {.5 tensor[[1, 5]], .5 tensor[[1, 4]], tensor[[1, 3]]}},
   {{tensor[[2, 1]], .5 tensor[[2, 6]], .5 tensor[[2, 5]]},
    {.5 tensor[[2, 6]], tensor[[2, 2]], .5 tensor[[2, 4]]},
    {.5 tensor[[2, 5]], .5 tensor[[2, 4]], tensor[[2, 3]]}},
   {{tensor[[3, 1]], .5 tensor[[3, 6]], .5 tensor[[3, 5]]},
    {.5 tensor[[3, 6]], tensor[[3, 2]], .5 tensor[[3, 4]]},
    {.5 tensor[[3, 5]], .5 tensor[[3, 4]], tensor[[3, 3]]}}};
```

■ Random Orientation of Dispersoids

This subroutine takes into account the random orientation of the dispersoids. Tensor values such as compliance, stiffness, and piezoelectric "g" values will be different depending on what set of reference axes one uses.

```
(*allows the user to specify the number of different orientations the subroutine will use*)
n = 25000;
```

```
(*this chooses "n" random mutually−perpindicular unit vectors to
    represent a set of reference axes for the randomly−oriented dispersoids*)
x1old = Table[UnitVector[{Random[Real, {-1, 1}],
     Random[Real, {-1, 1}], Random[Real, {-1, 1}]}], {n}];
randdirection = Table[UnitVector[{Random[Real, {-1, 1}],
     Random[Real, {-1, 1}], Random[Real, {-1, 1}]}], {n}];
x2old = Table[UnitVector[Cross[x1old[[i]], randdirection[[i]]]],
   {i, 1, n}];
x3old = Table[UnitVector[Cross[x1old[[i]], x2old[[i]]]],
   {i, 1, n}];
```

```
(*this generates "n" random directions [h,k,l]
   to represent random orientations of the dispersoids*)
 randomh = Table[Random[Real, {-1, 1}], {n}];
randomk = Table[Random[Real, {-1, 1}], {n}];
randoml = Table[Random[Real, {-1, 1}], {n}];
direction =
  Table[{randomh[[i]], randomk[[i]], randoml[[i]]}, {i, 1, n}];
```

```
(*This defines our new reference axes;
  in terms of common axis naming, x1old=x, x2old=y,
  x3old=z. The "newaxes" are the random directions resolved into three perpindicular axes,
  or the "new" x,y,z axes*)
newaxes = Table[{Cross[x1old[[i]], direction[[i]]],
     Cross[direction[[i]], Cross[x1old[[i]], direction[[i]]]],
     direction[[i]]}, {i, 1, n}];
  (*should have an x1,x2,x3 axis for each different random direction, "n"*)
x1new = Table[newaxes[[z, 1]], {z, 1, n}];
x2new = Table[newaxes[[z, 2]], {z, 1, n}];
x3new = Table[newaxes[[z, 3]], {z, 1, n}];
```

```
(*this defines the transformation matrices for each different orientation, "n"*)
a = Table[
   {{x1new[[i]].x1old[[i]] / (mag[x1new[[i]]] mag[x1old[[i]]]),
     x1new[[i]].x2old[[i]] / (mag[x1new[[i]]] mag[x2old[[i]]]),
     x1new[[i]].x3old[[i]] / (mag[x1new[[i]]] mag[x3old[[i]]])},
    {x2new[[i]].x1old[[i]] / (mag[x2new[[i]]] mag[x1old[[i]]]),
     x2new[[i]].x2old[[i]] / (mag[x2new[[i]]] mag[x2old[[i]]]),
     x2new[[i]].x3old[[i]] / (mag[x2new[[i]]] mag[x3old[[i]]])},
    {x3new[[i]].x1old[[i]] / (mag[x3new[[i]]] mag[x1old[[i]]]),
     x3new[[i]].x2old[[i]] / (mag[x3new[[i]]] mag[x2old[[i]]]),
     x3new[[i]].x3old[[i]] /
      (mag[x3new[[i]]] mag[x3old[[i]]])}}, {i, 1, n}];
```

The General Form of the Compliance and Stiffness Tensors

All information below comes from Reference [1], Chapter VIII.

■ Contracted Form

$$S_{ij} = \begin{pmatrix} S_{1,1} & S_{1,2} & S_{1,3} & S_{1,4} & S_{1,5} & S_{1,6} \\ S_{2,1} & S_{2,2} & S_{2,3} & S_{2,4} & S_{2,5} & S_{2,6} \\ S_{3,1} & S_{3,2} & S_{3,3} & S_{3,4} & S_{3,5} & S_{3,6} \\ S_{4,1} & S_{4,2} & S_{4,3} & S_{4,4} & S_{4,5} & S_{4,6} \\ S_{5,1} & S_{5,2} & S_{5,3} & S_{5,4} & S_{5,5} & S_{5,6} \\ S_{6,1} & S_{6,2} & S_{6,3} & S_{6,4} & S_{6,5} & S_{6,6} \end{pmatrix}$$

$$C_{ij} = \begin{pmatrix} C_{1,1} & C_{1,2} & C_{1,3} & C_{1,4} & C_{1,5} & C_{1,6} \\ C_{2,1} & C_{2,2} & C_{2,3} & C_{2,4} & C_{2,5} & C_{2,6} \\ C_{3,1} & C_{3,2} & C_{3,3} & C_{3,4} & C_{3,5} & C_{3,6} \\ C_{4,1} & C_{4,2} & C_{4,3} & C_{4,4} & C_{4,5} & C_{4,6} \\ C_{5,1} & C_{5,2} & C_{5,3} & C_{5,4} & C_{5,5} & C_{5,6} \\ C_{6,1} & C_{6,2} & C_{6,3} & C_{6,4} & C_{6,5} & C_{6,6} \end{pmatrix}$$

■ Expanded Form

$$S_{ijkl} = \begin{pmatrix} \begin{pmatrix} S_{1,1} & 0.5\,S_{1,6} & 0.5\,S_{1,5} \\ 0.5\,S_{1,6} & S_{1,2} & 0.5\,S_{1,4} \\ 0.5\,S_{1,5} & 0.5\,S_{1,4} & S_{1,3} \end{pmatrix} & \begin{pmatrix} 0.5\,S_{6,1} & 0.25\,S_{6,6} & 0.25\,S_{6,5} \\ 0.25\,S_{6,6} & 0.5\,S_{6,2} & 0.25\,S_{6,4} \\ 0.25\,S_{6,5} & 0.25\,S_{6,4} & 0.5\,S_{6,3} \end{pmatrix} & \begin{pmatrix} 0.5\,S_{5,1} & 0.25\,S_{5,6} & 0.25\,S_{5,5} \\ 0.25\,S_{5,6} & 0.5\,S_{5,2} & 0.25\,S_{5,4} \\ 0.25\,S_{5,5} & 0.25\,S_{5,4} & 0.5\,S_{5,3} \end{pmatrix} \\ \begin{pmatrix} 0.5\,S_{6,1} & 0.25\,S_{6,6} & 0.25\,S_{6,5} \\ 0.25\,S_{6,6} & 0.5\,S_{6,2} & 0.25\,S_{6,4} \\ 0.25\,S_{6,5} & 0.25\,S_{6,4} & 0.5\,S_{6,3} \end{pmatrix} & \begin{pmatrix} S_{2,1} & 0.5\,S_{2,6} & 0.5\,S_{2,5} \\ 0.5\,S_{2,6} & S_{2,2} & 0.5\,S_{2,4} \\ 0.5\,S_{2,5} & 0.5\,S_{2,4} & S_{2,3} \end{pmatrix} & \begin{pmatrix} 0.5\,S_{4,1} & 0.25\,S_{4,6} & 0.25\,S_{4,5} \\ 0.25\,S_{4,6} & 0.5\,S_{4,2} & 0.25\,S_{4,4} \\ 0.25\,S_{4,5} & 0.25\,S_{4,4} & 0.5\,S_{4,3} \end{pmatrix} \\ \begin{pmatrix} 0.5\,S_{5,1} & 0.25\,S_{5,6} & 0.25\,S_{5,5} \\ 0.25\,S_{5,6} & 0.5\,S_{5,2} & 0.25\,S_{5,4} \\ 0.25\,S_{5,5} & 0.25\,S_{5,4} & 0.5\,S_{5,3} \end{pmatrix} & \begin{pmatrix} 0.5\,S_{4,1} & 0.25\,S_{4,6} & 0.25\,S_{4,5} \\ 0.25\,S_{4,6} & 0.5\,S_{4,2} & 0.25\,S_{4,4} \\ 0.25\,S_{4,5} & 0.25\,S_{4,4} & 0.5\,S_{4,3} \end{pmatrix} & \begin{pmatrix} S_{3,1} & 0.5\,S_{3,6} & 0.5\,S_{3,5} \\ 0.5\,S_{3,6} & S_{3,2} & 0.5\,S_{3,4} \\ 0.5\,S_{3,5} & 0.5\,S_{3,4} & S_{3,3} \end{pmatrix} \end{pmatrix}$$

$$C_{ijkl} = \begin{pmatrix} \begin{pmatrix} C_{1,1} & C_{1,6} & C_{1,5} \\ C_{1,6} & C_{1,2} & C_{1,4} \\ C_{1,5} & C_{1,4} & C_{1,3} \end{pmatrix} & \begin{pmatrix} C_{6,1} & C_{6,6} & C_{6,5} \\ C_{6,6} & C_{6,2} & C_{6,4} \\ C_{6,5} & C_{6,4} & C_{6,3} \end{pmatrix} & \begin{pmatrix} C_{5,1} & C_{5,6} & C_{5,5} \\ C_{5,6} & C_{5,2} & C_{5,4} \\ C_{5,5} & C_{5,4} & C_{5,3} \end{pmatrix} \\ \begin{pmatrix} C_{6,1} & C_{6,6} & C_{6,5} \\ C_{6,6} & C_{6,2} & C_{6,4} \\ C_{6,5} & C_{6,4} & C_{6,3} \end{pmatrix} & \begin{pmatrix} C_{2,1} & C_{2,6} & C_{2,5} \\ C_{2,6} & C_{2,2} & C_{2,4} \\ C_{2,5} & C_{2,4} & C_{2,3} \end{pmatrix} & \begin{pmatrix} C_{4,1} & C_{4,6} & C_{4,5} \\ C_{4,6} & C_{4,2} & C_{4,4} \\ C_{4,5} & C_{4,4} & C_{4,3} \end{pmatrix} \\ \begin{pmatrix} C_{5,1} & C_{5,6} & C_{5,5} \\ C_{5,6} & C_{5,2} & C_{5,4} \\ C_{5,5} & C_{5,4} & C_{5,3} \end{pmatrix} & \begin{pmatrix} C_{4,1} & C_{4,6} & C_{4,5} \\ C_{4,6} & C_{4,2} & C_{4,4} \\ C_{4,5} & C_{4,4} & C_{4,3} \end{pmatrix} & \begin{pmatrix} C_{3,1} & C_{3,6} & C_{3,5} \\ C_{3,6} & C_{3,2} & C_{3,4} \\ C_{3,5} & C_{3,4} & C_{3,3} \end{pmatrix} \end{pmatrix}$$

Constituent Properties

Reinforcement Parameters

sij components taken from Reference [2],Table 5.C pg 74

sij components should be multiplied by 10^{-12} m^2 / N

Values below are for the crystalline form of $BaTiO_3$. Note that one could use the ceramic values if needed.

```
(*the stiffness tensor is obtained from the input compliance tensor*)
Sij_I = 10^-12 *
    {{8.05, -2.35, -5.24, 0, 0, 0}, {-2.35, 8.05, -5.24, 0, 0, 0},
     {-5.24, -5.24, 15.7, 0, 0, 0}, {0, 0, 0, 18.4, 0, 0},
     {0, 0, 0, 0, 18.4, 0}, {0, 0, 0, 0, 0, 8.84}};
Cij_I = Inverse[Sij_I] / 10^9    (* now in units of GPa *)

{{275.121, 178.967, 151.555, 0., 0., 0.},
 {178.967, 275.121, 151.555, 0., 0., 0.},
 {151.555, 151.555, 164.86, 0., 0., 0.},
 {0., 0., 0., 54.3478, 0., 0.},
 {0., 0., 0., 0., 54.3478, 0.}, {0., 0., 0., 0., 0., 113.122}}
```

```
(*expanding the stiffness tensor for use in calculations*)
Cijkl_I = ExpandStiffness[Cij_I]

{{{{275.121, 0., 0.}, {0., 178.967, 0.}, {0., 0., 151.555}},
  {{0., 113.122, 0.}, {113.122, 0., 0.}, {0., 0., 0.}},
  {{0., 0., 54.3478}, {0., 0., 0.}, {54.3478, 0., 0.}}},
 {{{0., 113.122, 0.}, {113.122, 0., 0.}, {0., 0., 0.}},
  {{178.967, 0., 0.}, {0., 275.121, 0.}, {0., 0., 151.555}},
  {{0., 0., 0.}, {0., 0., 54.3478}, {0., 54.3478, 0.}}},
 {{{0., 0., 54.3478}, {0., 0., 0.}, {54.3478, 0., 0.}},
  {{0., 0., 0.}, {0., 0., 54.3478}, {0., 54.3478, 0.}},
  {{151.555, 0., 0.}, {0., 151.555, 0.}, {0., 0., 164.86}}}}
```

We need the piezoelectric "g" values for the calculation of the electrical field induced within the reinforcement.
All values are taken from Reference [2],Table 5.C pg 74, and are for crystalline $BaTiO_3$.

General form of the contracted "g" tensor

$$g_{ij} = \begin{pmatrix} g_{1,1} & g_{1,2} & g_{1,3} & g_{1,4} & g_{1,5} & g_{1,6} \\ g_{2,1} & g_{2,2} & g_{2,3} & g_{2,4} & g_{2,5} & g_{2,6} \\ g_{3,1} & g_{3,2} & g_{3,3} & g_{3,4} & g_{3,5} & g_{3,6} \end{pmatrix}$$

```
g = 10^-3 * {{0, 0, 0, 0, 15.2, 0}, {0, 0, 0, 15.2, 0, 0},
      {-23, -23, 57.5, 0, 0, 0}} // N ;; (*values in Vm/N*)
```

- **Transformation of the "g" tensor into the expanded form for use in piezoelectric calculations**

The form of the expanded g tensor is below.

$$g_{ijk} = \begin{pmatrix} \begin{pmatrix} g_{1,1} \\ 0.5\, g_{1,6} \\ 0.5\, g_{1,5} \end{pmatrix} & \begin{pmatrix} 0.5\, g_{1,6} \\ g_{1,2} \\ 0.5\, g_{1,4} \end{pmatrix} & \begin{pmatrix} 0.5\, g_{1,5} \\ 0.5\, g_{1,4} \\ g_{1,3} \end{pmatrix} \\ \begin{pmatrix} g_{2,1} \\ 0.5\, g_{2,6} \\ 0.5\, g_{2,5} \end{pmatrix} & \begin{pmatrix} 0.5\, g_{2,6} \\ g_{2,2} \\ 0.5\, g_{2,4} \end{pmatrix} & \begin{pmatrix} 0.5\, g_{2,5} \\ 0.5\, g_{2,4} \\ g_{2,3} \end{pmatrix} \\ \begin{pmatrix} g_{3,1} \\ 0.5\, g_{3,6} \\ 0.5\, g_{3,5} \end{pmatrix} & \begin{pmatrix} 0.5\, g_{3,6} \\ g_{3,2} \\ 0.5\, g_{3,4} \end{pmatrix} & \begin{pmatrix} 0.5\, g_{3,5} \\ 0.5\, g_{3,4} \\ g_{3,3} \end{pmatrix} \end{pmatrix}$$

```
gnew = ExpandPiezo[g]

{{{0., 0., 0.0076}, {0., 0., 0.}, {0.0076, 0., 0.}},
 {{0., 0., 0.}, {0., 0., 0.0076}, {0., 0.0076, 0.}},
 {{-0.023, 0., 0.}, {0., -0.023, 0.}, {0., 0., 0.0575}}}
```

"NewTensor" is a command that transforms a tensor from the old reference axes to the new axes.
For example, $S'_{ijkl} = a_{im}\, a_{jn}\, a_{ko}\, a_{lp}\, S_{mnop}$, summing on m,n,o,p.
"allg" is a table of the "g" tensor resolved into each new set of reference axes; there are "n" different new "g" tensors.

```
allg = Table[NewTensor[gnew], {x, 1, n}];
```

```
(*"newallg" is just "allg" put into the contracted
   tensor form so we can do an electric field calculation*)
newallg = Table[{{allg[[i, 1, 1, 1]], allg[[i, 1, 2, 2]],
     allg[[i, 1, 3, 3]], 2*allg[[i, 1, 2, 3]],
     2*allg[[i, 1, 1, 3]], 2*allg[[i, 1, 1, 2]]},
    {allg[[i, 2, 1, 1]], allg[[i, 2, 2, 2]], allg[[i, 2, 3, 3]],
     2*allg[[i, 2, 2, 3]], 2*allg[[i, 2, 1, 3]],
     2*allg[[i, 2, 1, 2]]}, {allg[[i, 3, 1, 1]],
     allg[[i, 3, 2, 2]], allg[[i, 3, 3, 3]], 2*allg[[i, 3, 2, 3]],
     2*allg[[i, 3, 1, 3]], 2*allg[[i, 3, 1, 2]]}}, {i, 1, n}];
```

Matrix Parameters

For an isotropic material, such as a metallic alloy, the general form of the compliance tensor is below.

$$S_{ij} = \begin{pmatrix} \frac{1}{E} & -\frac{\nu}{E} & -\frac{\nu}{E} & 0 & 0 & 0 \\ -\frac{\nu}{E} & \frac{1}{E} & -\frac{\nu}{E} & 0 & 0 & 0 \\ -\frac{\nu}{E} & -\frac{\nu}{E} & \frac{1}{E} & 0 & 0 & 0 \\ 0 & 0 & 0 & \frac{2(1+\nu)}{E} & 0 & 0 \\ 0 & 0 & 0 & 0 & \frac{2(1+\nu)}{E} & 0 \\ 0 & 0 & 0 & 0 & 0 & \frac{2(1+\nu)}{E} \end{pmatrix}$$

All values below are for bulk Nickel and Chromium, and specific constant values taken from Reference [3].

■ Calculation of ROM Parameters for a Ni-20wt%Cr Matrix

The Rule of Mixtures, or ROM, is used below for estimation of a Ni-20wt%Cr matrix, but other approaches could be employed.

```
(*volume fractions were calculated using material–
   specific density values and corresponding weight percentage values*)
V_Ni = .76368;
V_Cr = .23633;
(*below are Poisson ratio values for the two constituents*)
 nu_Ni = 0.31;
nu_Cr = 0.31;
```

```
(*The "Sij_M" function is used below to calculate the compliance tensor for both nickel and
   chromium, given their elastic modulous values and Poisson ratio values. Additionally,
  the overall matrix stiffness tensor is defined.*)
compni = Sij_M[206.8, nu_Ni];
Cij_Ni = Inverse[compni];
compcr = Sij_M[248.2, nu_Cr];
Cij_Cr = Inverse[compcr];
Cij_M = (Cij_Ni * V_Ni) + (Cij_Cr * V_Cr)

{{300.21, 134.877, 134.877, 0., 0., 0.},
 {134.877, 300.21, 134.877, 0., 0., 0.},
 {134.877, 134.877, 300.21, 0., 0., 0.},
 {0., 0., 0., 82.6665, 0., 0.},
 {0., 0., 0., 0., 82.6665, 0.}, {0., 0., 0., 0., 0., 82.6665}}
```

```
(*The matrix stiffness and compliance tensors are put
   into expanded form so the composite stiffness can be calculated*)
Cijkl_M = ExpandStiffness[Cij_M];
sij = Inverse[Cij_M]
Sijkl_M = ExpandCompliance[sij];

{{0.0046171, -0.0014313, -0.0014313, 0., 0., 0.},
 {-0.0014313, 0.0046171, -0.0014313, 0., 0., 0.},
 {-0.0014313, -0.0014313, 0.0046171, 0., 0., 0.},
 {0., 0., 0., 0.0120968, 0., 0.},
 {0., 0., 0., 0., 0.0120968, 0.}, {0., 0., 0., 0., 0., 0.0120968}}
```

```
(*The matrix Poisson ratio is needed for the Eshelby shape tensor calculation*)
ν = (nu_Ni * V_Ni) + (nu_Cr * V_Cr);
```

```
(*The resistivity values for isotropic nickel and chromium are needed here to calculate
   the ROM resistivity value for the matrix. The resistivity will be used to calculate
   the conductivity of the matrix that will in turn be used to obtain the amount of
   resistive heat generated from induced electric fields in the reinforcement.*)
resistivity_Ni = 6.84 * 10^-8; (*in units of Ωm *)
resistivity_Cr = 1.29 * 10^-7; (*in units of Ωm *)
resistivity = (resistivity_Ni * V_Ni) + (resistivity_Cr * V_Cr);
conductivity = 1 / resistivity; (*in units of (Ωm)^-1 *)
```

Eshelby Tensor

The Eshelby Shape Tensor is used to quantify the effect that different material properties (i.e. stiffness) between the matrix and reinforcement has on the overall composite mechanical behavior. The misfit stress surrounding the particle and immediate near by matrix will depend on the shape of the inclusion particles and the Poisson ratio of the matrix.

■ Reinforcement as Spheres

The Eshelby shape tensor takes the form below when reinforcement is modeled as spheres. (taken from Reference [4]) It should be noted that This form of the Eshelby Tensor is used in this calculation but other shapes can be used. An example Eshelby tensor for prolate spheroids is below.

$$\begin{pmatrix} \frac{7-5\nu}{15(1-\nu)} & \frac{-1+5\nu}{15(1-\nu)} & \frac{-1+5\nu}{15(1-\nu)} & 0 & 0 & 0 \\ \frac{-1+5\nu}{15(1-\nu)} & \frac{7-5\nu}{15(1-\nu)} & \frac{-1+5\nu}{15(1-\nu)} & 0 & 0 & 0 \\ \frac{-1+5\nu}{15(1-\nu)} & \frac{-1+5\nu}{15(1-\nu)} & \frac{7-5\nu}{15(1-\nu)} & 0 & 0 & 0 \\ 0 & 0 & 0 & \frac{2(4-5\nu)}{15(1-\nu)} & 0 & 0 \\ 0 & 0 & 0 & 0 & \frac{2(4-5\nu)}{15(1-\nu)} & 0 \\ 0 & 0 & 0 & 0 & 0 & \frac{2(4-5\nu)}{15(1-\nu)} \end{pmatrix}$$

```
(*ν is the ROM Poisson ratio value for the matrix*)
Sij = Table[S[i, j], {i, 1, 6}, {j, 1, 6}];
Sij[[1, 1]] = (7 - 5 * ν) / (15 * (1 - ν));
Sij[[2, 2]] = Sij[[1, 1]];
Sij[[3, 3]] = Sij[[1, 1]];
Sij[[1, 2]] = (-1 + 5 * ν) / (15 * (1 - ν));
Sij[[2, 1]] = Sij[[1, 2]];
Sij[[1, 3]] = Sij[[1, 2]];
Sij[[2, 3]] = Sij[[1, 3]];
Sij[[3, 1]] = Sij[[2, 3]];
Sij[[3, 2]] = Sij[[3, 1]];
Sij[[4, 4]] = 2 * (4 - 5 * ν) / (15 * (1 - ν));
Sij[[5, 5]] = Sij[[4, 4]];
Sij[[6, 6]] = Sij[[4, 4]];
Seshelby = {{Sij[[1, 1]], Sij[[1, 2]], Sij[[1, 3]], 0, 0, 0},
   {Sij[[2, 1]], Sij[[2, 2]], Sij[[2, 3]], 0, 0, 0},
   {Sij[[3, 1]], Sij[[3, 2]], Sij[[3, 3]], 0, 0, 0},
   {0, 0, 0, Sij[[4, 4]], 0, 0}, {0, 0, 0, 0, Sij[[5, 5]], 0},
   {0, 0, 0, 0, 0, Sij[[6, 6]]}};
```

Composite Stiffness Tensor

The Eshelby - approach equation that is used to calculate composite compliance is listed in general form below. (taken from Reference [5])

$Q = f\,(S - I)[(C_M - C_I)\,S - C_M]^{-1}\,(C_I - C_M)$, and

$S_C = [I + (S - I)^{-1}\,(I + Q)^{-1}\,Q]\,C_M{}^{-1}$, where

S_C = composite compliance,

C_M = matrix stiffness,

C_I = reinforcement stiffness,

f = volume fraction of reinforcement,

S = Eshelby shape tensor,

$$I = \text{identity matrix} \rightarrow \begin{pmatrix} 1 & 0 & 0 & 0 & 0 & 0 \\ 0 & 1 & 0 & 0 & 0 & 0 \\ 0 & 0 & 1 & 0 & 0 & 0 \\ 0 & 0 & 0 & 1 & 0 & 0 \\ 0 & 0 & 0 & 0 & 1 & 0 \\ 0 & 0 & 0 & 0 & 0 & 1 \end{pmatrix}$$

```
Clear[f];
Q = f * (Seshelby - identity) .
    Inverse[(Cij_M - Cij_I) .Seshelby - Cij_M] .(Cij_I - Cij_M);
S_c = (identity + Inverse[Seshelby - identity] .
      Inverse[identity + Q] .Q) .Inverse[Cij_M];
```

```
(*"Modulus" is a function that calculates the composite compliance for a certain volume fraction of reinforcement.  This function is used to evaluate the compliance for several different volume fractions.  The table "almod" is made from these compliance values.*)
```

```
modulus[x_] := {f = x, S_c};
compmod = Table[modulus[i], {i, 0, 1, 0.025}];
almod = Table[1 / compmod[[i, 2, 3, 3]], {i, 1, Length[compmod]}]

{216.586, 210.852, 205.263, 199.814, 194.499, 189.314, 184.254,
 179.314, 174.49, 169.779, 165.176, 160.678, 156.281, 151.981,
 147.776, 143.663, 139.638, 135.698, 131.842, 128.066, 124.368,
 120.746, 117.196, 113.718, 110.309, 106.966, 103.689, 100.475,
 97.3216, 94.2281, 91.1926, 88.2133, 85.2887, 82.4173, 79.5978,
 76.8287, 74.1087, 71.4365, 68.8108, 66.2304, 63.6943}
```

■ General Form of Stress and Strain

$$\sigma_{ij} = \begin{pmatrix} \sigma_{11} & \sigma_{12} & \sigma_{13} \\ \sigma_{21} & \sigma_{22} & \sigma_{23} \\ \sigma_{31} & \sigma_{32} & \sigma_{33} \end{pmatrix}$$

$$\epsilon_{ij} = \begin{pmatrix} \epsilon_{11} & \epsilon_{12} & \epsilon_{13} \\ \epsilon_{21} & \epsilon_{22} & \epsilon_{23} \\ \epsilon_{31} & \epsilon_{32} & \epsilon_{33} \end{pmatrix}$$

■ Applied Stress Definition

The applied stress below is for a isostatic sound pressure of 50Pa which is typical for a jack hammer. Sound pressure represents the pressure induced on a body from a given sound source.

```
σ_applied = {{-0.50 * 10^-7, 0, 0}, {0, -0.50 * 10^-7, 0},
   {0, 0, -0.50 * 10^-7}};  (*make sure stress is in GPa*)
```

```
MatrixForm[σ_applied]
```

$$\begin{pmatrix} -5.\times10^{-8} & 0 & 0 \\ 0 & -5.\times10^{-8} & 0 \\ 0 & 0 & -5.\times10^{-8} \end{pmatrix}$$

■ Applied Strain (ϵ_A) Calculation from Applied Stress and Matrix Compliance

Applied strain can be calculated by this equation by the expression,
$\epsilon_{ij} = S_{ijkl}\,\sigma_{kl}$
It is defined as the strain that arrises from an applied load in an elastically homogeneous composite. That is, if the matrix and reinforcement were of the same material. The following calculation is defined in Reference [4] pg. 52

```
(*the sum is used instead of having to put the applied stress into contracted form*)
ϵ_A = Table[Sum[Sijkl_M[[i, j, k, l]] σ_applied[[k, l]],
   {k, 1, 3}, {l, 1, 3}], {i, 1, 3}, {j, 1, 3}]
```

```
{{-8.77249×10^-11, 0., 0.},
 {0., -8.77249×10^-11, 0.}, {0., 0., -8.77249×10^-11}}
```

■ Obtaining the contracted form (ϵ_{Acon}) of the applied strain matrix, ϵ_A

$$\begin{pmatrix} \sigma_{11} & \sigma_{12} & \sigma_{13} \\ \sigma_{21} & \sigma_{22} & \sigma_{23} \\ \sigma_{31} & \sigma_{32} & \sigma_{33} \end{pmatrix} \rightarrow \begin{pmatrix} \sigma_1 & \sigma_6 & \sigma_5 \\ \sigma_6 & \sigma_2 & \sigma_4 \\ \sigma_5 & \sigma_4 & \sigma_3 \end{pmatrix}, \quad \begin{pmatrix} \epsilon_{11} & \epsilon_{12} & \epsilon_{13} \\ \epsilon_{21} & \epsilon_{22} & \epsilon_{23} \\ \epsilon_{31} & \epsilon_{32} & \epsilon_{33} \end{pmatrix} \rightarrow \begin{pmatrix} \epsilon_1 & 0.5\,\epsilon_6 & 0.5\,\epsilon_5 \\ 0.5\,\epsilon_6 & \epsilon_2 & 0.5\,\epsilon_4 \\ 0.5\,\epsilon_5 & 0.5\,\epsilon_4 & \epsilon_3 \end{pmatrix}$$

```
ϵ_Acon = {ϵ_A[[1, 1]], ϵ_A[[2, 2]], ϵ_A[[3, 3]],
  2 * ϵ_A[[2, 3]], 2 * ϵ_A[[3, 1]], 2 * ϵ_A[[1, 2]]}
```

```
{-8.77249×10^-11, -8.77249×10^-11, -8.77249×10^-11, 0., 0., 0.}
```

```
Clear[f]
```

■ ϵ_T Calculation from ϵ_{Acon}

ϵ_T is sometimes called the "Eigen Strain";
equation from Reference [4] pg. 60

```
ϵTcon = -Inverse[(CijM - CijI).(Seshelby - f * (Seshelby - identity)) -
       CijM].(CijM - CijI).ϵAcon;
ϵT = {{ϵTcon[[1]], .5 * ϵTcon[[6]], .5 * ϵTcon[[5]]},
   {.5 * ϵTcon[[6]], ϵTcon[[2]], .5 * ϵTcon[[4]]},
   {.5 * ϵTcon[[5]], .5 * ϵTcon[[4]], ϵTcon[[3]]}};
```

■ Calculation of Mean Internal Stress of Constituents

from Reference [4] pg.61

```
σMmeancon = -f * CijM.(Seshelby - identity).ϵTcon;
(*this is the mean stress in the matrix*)
σMmean = {{σMmeancon[[1]], σMmeancon[[6]], σMmeancon[[5]]},
   {σMmeancon[[6]], σMmeancon[[2]], σMmeancon[[4]]},
   {σMmeancon[[5]], σMmeancon[[4]], σMmeancon[[3]]}};
σImeancon = (1 - f) * CijM.(Seshelby - identity).ϵTcon;
(*this is the mean stress in the inclusions*)
σImean = {{σImeancon[[1]], σImeancon[[6]], σImeancon[[5]]},
   {σImeancon[[6]], σImeancon[[2]], σImeancon[[4]]},
   {σImeancon[[5]], σImeancon[[4]], σImeancon[[3]]}};
(*the calculation below should be zero if the mean stresses are defined appropriately*)
(1 - f) * σMmeancon + f * σImeancon // Chop

{0, 0, 0, 0, 0, 0}
```

■ Calculation of Average Stress of Constituents

Calculation procedure from Reference [4] pg. 61

```
Clear[f];
(*The average stress in the matrix is simply the applied stress plus its mean stress*)
σMavg = σapplied + σMmean;
(*the contracted form*)
σMavgcon = {σMavg[[1, 1]], σMavg[[2, 2]],
    σMavg[[3, 3]], σMavg[[2, 3]], σMavg[[3, 1]], σMavg[[1, 2]]};
(*"avgmatrixstress" is a function that retrieves the value for the average
   stress in the matrix for a given volume fraction of reinforcement*)
avgmatrixstress[x_] := Block[{f = x}, σMavgcon];
(*"matrixstress" is a table of the average matrix stresses for
   volume fractions ranging from 0 to 1 with a step increment of 0.025.*)
matrixstress = Table[avgmatrixstress[i], {i, 0, 1, .025}]
```

```
{{-5.×10^-8, -5.×10^-8, -5.×10^-8, 0, 0, 0},
 {-4.99439×10^-8, -4.99439×10^-8, -5.01827×10^-8, 0., 0., 0.},
 {-4.98868×10^-8, -4.98868×10^-8, -5.0371×10^-8, 0., 0., 0.},
 {-4.98288×10^-8, -4.98288×10^-8, -5.05653×10^-8, 0., 0., 0.},
 {-4.97697×10^-8, -4.97697×10^-8, -5.07656×10^-8, 0., 0., 0.},
 {-4.97096×10^-8, -4.97096×10^-8, -5.09724×10^-8, 0., 0., 0.},
 {-4.96484×10^-8, -4.96484×10^-8, -5.11859×10^-8, 0., 0., 0.},
 {-4.9586×10^-8, -4.9586×10^-8, -5.14064×10^-8, 0., 0., 0.},
 {-4.95224×10^-8, -4.95224×10^-8, -5.16343×10^-8, 0., 0., 0.},
 {-4.94574×10^-8, -4.94574×10^-8, -5.18699×10^-8, 0., 0., 0.},
 {-4.93912×10^-8, -4.93912×10^-8, -5.21135×10^-8, 0., 0., 0.},
 {-4.93235×10^-8, -4.93235×10^-8, -5.23655×10^-8, 0., 0., 0.},
 {-4.92544×10^-8, -4.92544×10^-8, -5.26265×10^-8, 0., 0., 0.},
 {-4.91837×10^-8, -4.91837×10^-8, -5.28967×10^-8, 0., 0., 0.},
 {-4.91113×10^-8, -4.91113×10^-8, -5.31768×10^-8, 0., 0., 0.},
 {-4.90372×10^-8, -4.90372×10^-8, -5.34672×10^-8, 0., 0., 0.},
 {-4.89613×10^-8, -4.89613×10^-8, -5.37684×10^-8, 0., 0., 0.},
 {-4.88835×10^-8, -4.88835×10^-8, -5.40811×10^-8, 0., 0., 0.},
 {-4.88037×10^-8, -4.88037×10^-8, -5.44058×10^-8, 0., 0., 0.},
 {-4.87217×10^-8, -4.87217×10^-8, -5.47433×10^-8, 0., 0., 0.},
 {-4.86374×10^-8, -4.86374×10^-8, -5.50943×10^-8, 0., 0., 0.},
 {-4.85508×10^-8, -4.85508×10^-8, -5.54596×10^-8, 0., 0., 0.},
 {-4.84616×10^-8, -4.84616×10^-8, -5.584×10^-8, 0., 0., 0.},
 {-4.83697×10^-8, -4.83697×10^-8, -5.62364×10^-8, 0., 0., 0.},
 {-4.82749×10^-8, -4.82749×10^-8, -5.66499×10^-8, 0., 0., 0.},
 {-4.81771×10^-8, -4.81771×10^-8, -5.70815×10^-8, 0., 0., 0.},
 {-4.8076×10^-8, -4.8076×10^-8, -5.75323×10^-8, 0., 0., 0.},
 {-4.79715×10^-8, -4.79715×10^-8, -5.80038×10^-8, 0., 0., 0.},
 {-4.78633×10^-8, -4.78633×10^-8, -5.84971×10^-8, 0., 0., 0.},
 {-4.77511×10^-8, -4.77511×10^-8, -5.9014×10^-8, 0., 0., 0.},
 {-4.76347×10^-8, -4.76347×10^-8, -5.9556×10^-8, 0., 0., 0.},
 {-4.75137×10^-8, -4.75137×10^-8, -6.01249×10^-8, 0., 0., 0.},
 {-4.73878×10^-8, -4.73878×10^-8, -6.07228×10^-8, 0., 0., 0.},
 {-4.72567×10^-8, -4.72567×10^-8, -6.13519×10^-8, 0., 0., 0.},
 {-4.71199×10^-8, -4.71199×10^-8, -6.20145×10^-8, 0., 0., 0.},
 {-4.69769×10^-8, -4.69769×10^-8, -6.27135×10^-8, 0., 0., 0.},
 {-4.68273×10^-8, -4.68273×10^-8, -6.34517×10^-8, 0., 0., 0.},
 {-4.66705×10^-8, -4.66705×10^-8, -6.42326×10^-8, 0., 0., 0.},
 {-4.65059×10^-8, -4.65059×10^-8, -6.50598×10^-8, 0., 0., 0.},
 {-4.63327×10^-8, -4.63327×10^-8, -6.59375×10^-8, 0., 0., 0.},
 {-4.61502×10^-8, -4.61502×10^-8, -6.68704×10^-8, 0., 0., 0.}}
```

```
(*The average stress in the reinforcement is simply the applied stress plus its mean stress*)
σIavg = σapplied + σImean;
(*the contracted form*)
σIavgcon = {σIavg[[1, 1]], σIavg[[2, 2]],
    σIavg[[3, 3]], σIavg[[2, 3]], σIavg[[3, 1]], σIavg[[1, 2]]};
(*"avgincstress" is a function that retrieves the value for the average stress
    in the reinforcement for a given volume fraction of reinforcement*)
avgincstress[x_] := Block[{f = x}, σIavgcon];
(*"inclusionstress" is a table of the average reinforcement stresses for
    volume fractions ranging from 0 to 1 with a step increment of 0.025.*)
inclusionstress = Table[avgincstress[i], {i, 0, 1, .025}]
```

```
{{-5.22266×10^-8, -5.22266×10^-8, -4.28021×10^-8, 0., 0., 0.},
 {-5.21886×10^-8, -5.21886×10^-8, -4.2875×10^-8, 0., 0., 0.},
 {-5.21503×10^-8, -5.21503×10^-8, -4.29505×10^-8, 0., 0., 0.},
 {-5.21115×10^-8, -5.21115×10^-8, -4.30285×10^-8, 0., 0., 0.},
 {-5.20723×10^-8, -5.20723×10^-8, -4.31094×10^-8, 0., 0., 0.},
 {-5.20326×10^-8, -5.20326×10^-8, -4.31931×10^-8, 0., 0., 0.},
 {-5.19925×10^-8, -5.19925×10^-8, -4.32798×10^-8, 0., 0., 0.},
 {-5.19518×10^-8, -5.19518×10^-8, -4.33696×10^-8, 0., 0., 0.},
 {-5.19106×10^-8, -5.19106×10^-8, -4.34628×10^-8, 0., 0., 0.},
 {-5.18688×10^-8, -5.18688×10^-8, -4.35594×10^-8, 0., 0., 0.},
 {-5.18264×10^-8, -5.18264×10^-8, -4.36596×10^-8, 0., 0., 0.},
 {-5.17835×10^-8, -5.17835×10^-8, -4.37636×10^-8, 0., 0., 0.},
 {-5.17398×10^-8, -5.17398×10^-8, -4.38716×10^-8, 0., 0., 0.},
 {-5.16955×10^-8, -5.16955×10^-8, -4.39837×10^-8, 0., 0., 0.},
 {-5.16504×10^-8, -5.16504×10^-8, -4.41003×10^-8, 0., 0., 0.},
 {-5.16046×10^-8, -5.16046×10^-8, -4.42214×10^-8, 0., 0., 0.},
 {-5.1558×10^-8, -5.1558×10^-8, -4.43474×10^-8, 0., 0., 0.},
 {-5.15105×10^-8, -5.15105×10^-8, -4.44786×10^-8, 0., 0., 0.},
 {-5.14622×10^-8, -5.14622×10^-8, -4.46151×10^-8, 0., 0., 0.},
 {-5.14129×10^-8, -5.14129×10^-8, -4.47574×10^-8, 0., 0., 0.},
 {-5.13626×10^-8, -5.13626×10^-8, -4.49057×10^-8, 0., 0., 0.},
 {-5.13112×10^-8, -5.13112×10^-8, -4.50604×10^-8, 0., 0., 0.},
 {-5.12587×10^-8, -5.12587×10^-8, -4.52218×10^-8, 0., 0., 0.},
 {-5.1205×10^-8, -5.1205×10^-8, -4.53905×10^-8, 0., 0., 0.},
 {-5.11501×10^-8, -5.11501×10^-8, -4.55668×10^-8, 0., 0., 0.},
 {-5.10937×10^-8, -5.10937×10^-8, -4.57511×10^-8, 0., 0., 0.},
 {-5.1036×10^-8, -5.1036×10^-8, -4.59441×10^-8, 0., 0., 0.},
 {-5.09767×10^-8, -5.09767×10^-8, -4.61463×10^-8, 0., 0., 0.},
 {-5.09157×10^-8, -5.09157×10^-8, -4.63584×10^-8, 0., 0., 0.},
 {-5.0853×10^-8, -5.0853×10^-8, -4.65809×10^-8, 0., 0., 0.},
 {-5.07884×10^-8, -5.07884×10^-8, -4.68147×10^-8, 0., 0., 0.},
 {-5.07218×10^-8, -5.07218×10^-8, -4.70605×10^-8, 0., 0., 0.},
 {-5.0653×10^-8, -5.0653×10^-8, -4.73193×10^-8, 0., 0., 0.},
 {-5.05819×10^-8, -5.05819×10^-8, -4.7592×10^-8, 0., 0., 0.},
 {-5.05083×10^-8, -5.05083×10^-8, -4.78798×10^-8, 0., 0., 0.},
 {-5.04319×10^-8, -5.04319×10^-8, -4.81838×10^-8, 0., 0., 0.},
 {-5.03525×10^-8, -5.03525×10^-8, -4.85054×10^-8, 0., 0., 0.},
 {-5.027×10^-8, -5.027×10^-8, -4.8846×10^-8, 0., 0., 0.},
 {-5.01839×10^-8, -5.01839×10^-8, -4.92074×10^-8, 0., 0., 0.},
 {-5.0094×10^-8, -5.0094×10^-8, -4.95913×10^-8, 0., 0., 0.},
 {-5.×10^-8, -5.×10^-8, -5.×10^-8, 0., 0., 0.}}
```

■ Calculation of Average Electric Field

"allEfield" is a table of all of the calculated electric fields based on the average stress in the reinforcment and each newly-resolved "g" tensor; there are "n" different electric fields representing the electric field produced for the given reinforcement stress and transformed "g" tensor.
Note: This model assumes that all of the load transfer to the inclusions is transformed into an electric field through the "g" tensor.

```
allEfield = Table[Table[newallg[[i]].(10^9 * inclusionstress[[j]]),
    {i, 1, n}], {j, 1, Length[inclusionstress]}];
```

■ Calculation of Joule Heating

If we assume that the average electric field induced within the piezoelectric-ceramic particles is fully coupled between the electrically conducting matrix, then we can calculate the average Joule heating per unit time and volume of material.

In order to calculate this we need the electrical conductivity tensor for the matrix. If we are dealing with a polycrystaline metallic matrix then the electrical conductivity values should be the same in each direction and the only important terms are the ones in the principal directions. (Reference [1] pg. 213)

The conductivity tensor looks like this: $\begin{pmatrix} \sigma_{11} & \sigma_{12} & \sigma_{13} \\ \sigma_{21} & \sigma_{22} & \sigma_{23} \\ \sigma_{31} & \sigma_{32} & \sigma_{33} \end{pmatrix}$, which for polycrystalline materials goes to this $\rightarrow \begin{pmatrix} \sigma & 0 & 0 \\ 0 & \sigma & 0 \\ 0 & 0 & \sigma \end{pmatrix}$

```
(*The conductivity values below come from the previously-defined matrix values*)
econd = {{conductivity, 0, 0},
    {0, conductivity, 0}, {0, 0, conductivity}};
(*The root-mean-squared (rms) electric field value is simply a way to
    determine the average electric field induced in the randomly-
   oriented reinforcement. It essentially gives us the average of the
    magnitudes of all of the electric fields for each random orientation*)
rmsEfield = Table[((Sum[allEfield[[j, i]]^2, {i, 1, n}]) / n)^0.5,
    {j, 1, Length[inclusionstress]}];
(*The current density, "cdens", is defined as the electrical conductivity of the matrix
    dotted into the root-mean-squared electric field value (Reference [1])*)
cdens = Table[econd.rmsEfield[[i]],
    {i, 1, Length[inclusionstress]}]; (*in units of A/m^2*)
```

```
(*If we assume that we're dealing with 1 cm^3 of composite,
  then the volume of reinforcement is just "f" in units of cm^3.
     We are essentially defining the effective amount of Joule
    heat that is produced in 1 cm^3 of composite material.*)
VolumeFraction = Table[i, {i, 0, 1, .025}];
(*The Joule heat values below are for each different volume fraction of reinforcement
    and are defined as the current density dotted into the rms electric field value,
  multiplied by the given volume of reinforcement*)
JouleHeat = Table[
   ((cdens[[i]].rmsEfield[[i]]) * VolumeFraction[[i]]),
   {i, 1, Length[inclusionstress]}] (*in units of J/s*)

{0, 0.112479, 0.224167, 0.335057, 0.445137, 0.5544, 0.662835,
 0.770435, 0.877191, 0.983098, 1.08815, 1.19234, 1.29566,
 1.39811, 1.4997, 1.60042, 1.70028, 1.79928, 1.89743, 1.99476,
 2.09128, 2.18701, 2.28199, 2.37625, 2.46985, 2.56285, 2.65531,
 2.74734, 2.83902, 2.9305, 3.02191, 3.11345, 3.20533, 3.2978,
 3.39117, 3.48581, 3.58216, 3.68074, 3.78218, 3.88723, 3.99681}
```

The values of Joule heat represent the amount of heat that is generated specifically through the inherent resistance of the matrix material, in this case a Ni-20wt%Cr alloy. An average electric field is induced within the reinforcement from a stress that is applied to the composite system. Some portion of this stress is transferred to the reinforcement, thus inducing an electric field within it that is then transformed into resistive heat by the surrounding matrix. We therefor have a transformation of energy resulting in a means of mechanical damping.

References

[1] J.F.Nye,*Physical Properties of Crystals, Their Representation by Tensors and Matrices* (Clarendon Press,Oxford,1957)

[2] B.Jaffe,W.R.Cook,and H.L.C.Jaffâe, *Piezoelectric Ceramics* (Academic-Press,London,NewYork,1971)

[3] World Wide Web address: www.efunda.com

[4] T.W.Clyne and P.J.Withers, *An Introduction to Metal Matrix Composites*, 1993

[5] G.K.Hu and F.Tian, "Micromechanical Analysis of Fatigue Properties of Metal-Matrix Composites", 24 65-68 (1997)

Vita

The author was born on October 1, 1977 in Charleston, West Virginia. He was raised by his loving parents in Hurricane, West Virginia and spent much of his time exploring his Grandparents' farmland in rural Looneyville, West Virginia. The author was introduced to metallurgy at a young age when he and his brothers melted lead-cased bullets that they unearthed from a nearby shooting range. The beauty of molten metal and the mysteriousness of phase change has haunted the author ever since.

After graduating from Winfield High School in the spring of 1996, the author acquired a scholarship to attend Virginia Tech in Blacksburg, Virginia starting that fall. A bout with mononucleosis forced the author to take the spring 1997 semester off and to return to his home state of West Virginia. He returned to Virginia Tech during the summer academic session of 1997 and has been enrolled in the Materials Science and Engineering Department since the fall of 1997. The author co-op'ed at Union Carbide Corporation (now owned by DOW chemical) in South Charleston, West Virginia during the spring and summer of 1998 and the summer of 1999. While there, he worked in a failure analysis lab performing odd-jobs related to materials characterization and corrosion issues. It was here that the author obtained his first true taste of scientific research.

During the summer of 2000, the author began undergraduate research work on finding an appropriate polymer filler material for use in a light-activated adhesive resin under the supervision of Dr. Brian Love. It was this setting that piqued the author's interest in attending graduate school. Upon graduating from Virginia Tech with a B.S. in Materials Science and Engineering in May 2001, the author enrolled in graduate school and began work on his thesis project under the supervision of Dr. Stephen Kampe. A milestone occurred for the author when he proposed to his girlfriend, Caren Tahan, on December 15, 2001. Luckily, he is currently engaged to be married on July 12, 2003.

After completing requirements for a Master's of Science degree in May 2003, the author will continue to work on this project, tying up loose ends until late June. Eventually he will obtain a job and settle down with his new wife, but until then he is looking forward to a much-deserved honeymoon in St. John, USVI.